χ_c production in $p\bar{p}$ Collisions at $\sqrt{s} = 1.8$ TeV

A Dissertation Presented

by

Regina Demina

to

The Graduate School

in Partial Fulfillment of the Requirements

for the Degree of

Doctor of Philosophy

in

Physics

Northeastern University
Boston, Massachusetts

December 1994

χ_c production in $p\bar{p}$ Collisions at $\sqrt{s} = 1.8$ TeV

by

Regina Demina

ABSTRACT OF DISSERTATION

In this thesis I report the full reconstruction of χ_c mesons through the decay chain

$$\chi_c \to J/\psi + \gamma, \quad J/\psi \to \mu^+ \mu^-,$$

using data collected at $\sqrt{s} = 1.8$ TeV in 13.0 pb^{-1} of $p\bar{p}$ collisions with the DØ detector at Fermilab. This sample is used to obtain the χ_c production cross section times branching fractions

$$\sigma(p\bar{p} \to \chi_c + X) \times B(\chi_c \to J/\psi + \gamma) \times B(J/\psi \to \mu^+ \mu^-).$$

Together with the total J/ψ sample it is used to measure the fraction of J/ψ events coming from χ_c decay. The relative contributions of different χ_c production mechanisms are discussed.

Submitted in partial fulfillment of the requirements
for the degree of Doctor of Philosophy in Physics
in the Graduate School of Arts and Sciences of
Northeastern University, December 1994

Acknowledgements

Thanks to God it happened I am here. And thanks to God it happened I have completed my PhD requirements and thus my graduate study. All right, it's over and I'm still alive. Thanks again.

It is pleasure to thank God because of a low possibility to misspell his sane name. So I'll do that again in the very end.

I would like to thank my parents. They approved my choice to be a scientist.

And so did my first Physics teacher, Yury Grigorievich Sulima. I do remember that dialog after my high school graduation when you asked me if I'm going to university and what department. "Well, - I answered, - History..." "What's a damn fool! Look, that's stupid, you have to apply for Physics, you are physicist can you understand that?" Thank you, sir, that was a very critical advice.

I thank you, my teachers at Novosibirsk State University, - Lev Barkov, Marek Zolotorev, Arkady Vainshtein, Vladimir Zelevinsky, Senya Eidelman, Valery Serbo and others, - yes, physics is clear now a little bit or at least I think it is clear. I mean I can talk about it at least and even write.

I really want to thank some people as well who sincerely or not it doesn't matter determined my life way, gave me a support and helped me to live and to work in a very different country and all about it.

My dear Steve. There are no words to express my appreciation. I would like to work with you for the rest of my life simply because you are that ideal of supervisor I only can imagine, simply the best.

Thank you Geneam! You are kind and all, and you are my friend, man. Don't lock the tapes, please.

Thanks to Daria Zieminska, Zhenya Kozlovsky, Andrzej Zieminski, Chris Murphy, Sasha Peryshkin for the interest to my research at DØ and for the real fruitful discussions and all.

Thanks to Thorsten Huehn who was a instant example of a hard worker, that ideal of the scientist which I would like to be but I couldn't. But you have encouraged me a lot, thanks, Thorsten.

Thanks to George Fanourakis. You are the best colleague I ever met and it was a real pleasure to work with you.

Thanks to Robert Fripp for his music which inspired me on my way.

Thanks to Dan Green who made a proposal for the theme of my PhD thesis.

And thanks to God!!! Peace.

Contents

Abstract i

Acknowledgements iii

Table of Contents v

List of Tables x

List of Figures xi

1 Introduction 1

1.1 Colliders 2

1.2 Collider Detector Organization 3

1.3 Quarks and Leptons 3

1.4 Fundamental Forces 5

1.5 Perturbative QED and QCD 8

1.6 Charmonium system 10

1.7 Outline of the Thesis 12

2 Theoretical Overview **14**

2.1 The Production of Charmonium States 14

2.2 Assumptions 14

2.2.1 The Parton Model 14

2.2.2 The Coordinate System and Kinematic Variables 17

2.2.3 Perturbative QCD 20

2.2.4 Fragmentation 20

2.2.5 The Nonrelativistic quarkonium model 21

2.2.6 Assumption Summary 22

2.3 Mechanisms of charmonium production in hadronic collisions 22

2.3.1 Direct Hadroproduction 22

2.3.2 b-quark Decay 25

2.3.3 Gluon and c-quark Fragmentation 28

2.4 The Production Pattern 29

2.5 Summary 33

3 Experimental Apparatus **35**

3.1 The Tevatron $p\bar{p}$ collider 35

3.2 The DØ Detector 39

3.2.1 The Central Detector 40

3.2.2 Calorimetry 45

3.2.3 The Muon System 49

3.2.4 The Trigger System 52

3.3 Data Processing 55

3.4 Particle Identification 58

3.4.1 Photons and Electrons 58

3.4.2 Muons 59

3.4.3 Jets 61

3.4.4 Neutrinos 62

4 Estimates 63

4.1 Kinematics 63

4.2 Kinematic Resolution Estimates 71

4.3 The Goals of the Experiment 72

5 Event Selection 74

5.1 Single Muon Selection 75

5.1.1 Level 1 trigger. 75

5.1.2 Level 2 trigger. 75

5.1.3 Offline selection. 75

5.1.4 Dimuon selection. 76

5.2 Contributions to the dimuon spectrum 77

5.2.1 b-quark decay. 78

5.2.2 Drell-Yan 79

5.2.3 Muons from Hadronic Jets 80

5.2.4 Cosmics 81

5.2.5 J/ψ 82

5.3 Fitting the Dimuon Spectrum 83

5.4 MU_2_HIGH Dimuons 85

5.4.1 Photon Selection 86

5.5 χ_c Reconstruction for Different P_t regions 89

5.6 Isolation requirement 94

6 Efficiency Determination 98

6.1 The J/ψ Kinematic Region 100

6.2 Muon Acceptance 101

6.3 J/ψ Identification Efficiency 102

6.4 Photon Acceptance 103

6.5 Photon Reconstruction Efficiency 103

6.6 Systematic Errors 104

7 Results and Conclusion 106

7.1 Presentation of the Result 106

7.2 Determination of the Fraction of J/ψ Coming from χ_c Decay 107

7.3 Cross Section Determination 108

7.4 The P_t Dependance of the Fraction of J/ψ Coming from χ_c Decay. . 110

7.5 Isolated χ_c. 111

7.6 Discussion of the Different Production Mechanisms. 111

7.7 Conclusion 112

8 Charmonium Physics with the DØ Upgrade 114

8.1 Problems 114

8.2 The DØ Upgrade 115

8.2.1 Main Injector 115

8.2.2 The DØ Upgrade 115

8.2.3 The DØ Central Magnetic Field 116

8.2.4 The DØ Silicon Vertex Detector 116

8.2.5 The DØ Fiber Tracking System 116

8.3 Cosmic Ray Test of the DØ Fiber Tracking System 118

8.3.1 The Cosmic Ray Test Setup 118

8.3.2 The Cosmic Ray Test Results 119

8.4 Estimates for Charmonium Production with the Upgraded DØ Detector 119

Bibliography **121**

Appendix **126**

List of Tables

1.1 Three generations of quarks and leptons 4

2.1 The relative production of χ_c and J/ψ states in B-decay 29

7.1 The number of fully reconstructed χ_c events, the number of J/ψ events and the efficiency to register the photon from χ_c decay 108

7.2 The number of J/ψ events, the total integrated luminosity of this data set and the efficiency of J/ψ registration 109

7.3 Number of χ_c and J/ψ events and photon efficiency for two $P_t^{\mu\mu}$ regions 110

List of Figures

1.1 Electro-weak doublet interaction with W and Z bosons and the photon 6

1.2 (a) Quark-gluon interaction vertex; (b) Triple gluon vertex 7

1.3 Lowest order QED vacuum polarization diagram 8

1.4 Lowest order QCD vacuum polarization diagram: (a) quark-antiquark loop; (b) gluon loop 9

1.5 The charmonium system. J denotes the total angular momentum of a particular state, P is its P-parity and C is its C-parity. The first symbol in brackets next to the name of a state indicates its radial and orbital quantum numbers in the atomic notation, the second number in brackets is the mass of a particle. The arrows indicate possible radiative decays and the numbers in brackets next to the γ show the branching ratios of these decays. 11

2.1 The parton scattering representation of a proton-antiproton collision 15

2.2 DØ coordinate system 19

2.3 The $O(\alpha_s^2)$ Feynman diagram for charmonium production. $^1S_0$ represents η_c, $^3P_{0,2}$ represents $\chi_{c_{0,2}}$. 23

2.4 The $O(\alpha_s^3)$ Feynman diagrams for charmonium production. $^1S_0$ represents η_c, ^3P_J represents χ_{c_J}. 24

2.5 Charmonium production via triple gluon vertex. $^1S_0$ represents η_c, ^3P_J represents χ_{c_J}, $^3S_1$ represents J/ψ. 25

2.6 Feynman diagrams for b-quark production in a $p\bar{p}$ collision. 26

2.7 Example of b-quark fragmentation. 27

2.8 Charmonium production in b-quark decay. 27

2.9 The Feynman diagrams for charmonium production via fragmentation of a gluon (a,c,d) or a c-quark (b) . $^1S_0$ represents η_c, ^3P_J represents χ_{c_J}, $^3S_1$ represents J/ψ. 30

2.10 The dependence of the χ_c and J/ψ production cross section versus P_t for the different production mechanisms: direct charmonium production, charmonium production from b-decay and charmonium production from gluon fragmentation 32

3.1 The Tevatron collider with two high luminosity interaction points: DØ and CDF 36

3.2 General view of the DØ detector 41

3.3 A cross section of the DØ tracking system 42

3.4 The cell structure of the DØ vertex chamber 43

3.5 A cut away view of the DØ calorimeter system 46

3.6 A unit cell structure of the DØ calorimeter 47

3.7 General view of the DØ muon system 50

3.8 The pad structure of the DØ muon system 52

3.9 The scheme of data processing at DØ 57

4.1 The transverse momentum distribution of the muons from J/ψ decay 66

4.2 Distribution in the angle between the two muons from J/ψ decay . . 67

4.3 The J/ψ transverse momentum distribution 68

4.4 The energy distribution of the photon from χ_c decay 69

4.5 Distribution in the angle between J/ψ and the photon from χ_c decay. 70

5.1 The experimental spectrum of the invariant mass of two muons the curves show the fit to the background plus the J/ψ signal shapes (solid line) and the background shape (dashed line). 77

5.2 Feynman diagram of the parallel b-quark decay 79

5.3 Feynman diagram of the sequential b-quark decay 80

5.4 The combined invariant mass spectrum of muons from b-quark decay, obtained from a full Monte-Carlo simulation 81

5.5 Feynman diagram of the Drell-Yan process 82

5.6 The invariant mass spectrum of two muons from the Drell-Yan process, obtained from a full Monte-Carlo simulation 83

5.7 The invariant mass spectrum of two muons from the hadronic jets, obtained from a full Monte-Carlo simulation 84

5.8 The invariant mass spectrum of the cosmic ray muons, obtained from cosmic ray runs 85

5.9 The dimuon invariant mass spectrum of the J/ψ signal from a full Monte-Carlo simulation 86

5.10 The experimental dimuon invariant mass spectrum for post shutdown data, MU_2_HIGH trigger 87

5.11 The mass difference spectrum ($\Delta M = M_{\mu^+\mu^-\gamma} - M_{\mu^+\mu^-}$) for the selected dimuon events 88

5.12 The ΔM distribution for J/ψ from b-quark decay 89

5.13 The ΔM distribution for dimuons from parallel and sequential b-quark decays 90

5.14 The ΔM distribution for the Drell-Yan process 91

5.15 The ΔM distribution for same sign muons 91

5.16 The ΔM distribution for J/ψ from χ_c decay 92

5.17 The dimuon mass ($M_{\mu\mu}$) spectra and $\Delta M(= M_{\mu\mu\gamma} - M_{\mu\mu})$ spectra for P_t regions: $8 < P_t < 10$ GeV/c and $P_t > 10$ GeV/c 93

5.18 The fraction of events that have no jet in the cone, ΔR, around the dimuon, as a function of the size of the cone, ΔR a) J/ψ from χ_c decay; b) J/ψ from b-quark decay; c) parallel and sequential b-quark decay; 95

5.19 The dimuon invariant mass spectrum of isolated muons 96

5.20 The mass difference spectrum ($\Delta M = M_{\mu^+\mu^-\gamma} - M_{\mu^+\mu^-}$) for the isolated dimuon events 97

6.1 The acceptance for muons within $|\eta| < 0.6$ region as a function of the P_t of the dimuon system 100

6.2 The J/ψ efficiency dependance on the transverse momentum of the dimuon system 101

6.3 The dependance of the efficiency of photon reconstruction as a function of energy 102

8.1 Layout of the DØ upgrade showing solenoid, scintillating fiber superlayers, silicon barrels and disks and the preshower detector. 117

8.2 The schematic layout of the Cosmic Ray Test stand 119

Chapter 1

Introduction

I remember my father telling me, when I was very young, that we all and the trees and the Sun and fishes and everything are built of molecules, which are in turn made of atoms. Each atom consists of the nucleus and the electrons around it; and the nucleus is a crowd of protons and neutrons packed together. These were the most exciting stories of my childhood. Even more exciting is the question of how deep can we go in breaking matter apart and how can we accomplish it.

The concept of the atom was suggested by Democritus in ancient Greece. Unfortunately mankind could go no further with this idea until an elegant method of probing the structure of matter was used by Rutherford, at the beginning of the 20th century [1] . In his famous experiment, he bombarded a gold foil with alpha particles and discovered that some of them are scattered backwards from the gold. The only acceptable interpretation of Rutherford's results is that the atom must contain a small hard core – the nucleus. This experiment immediately brought us 5 orders of magnitude deeper inside the structure of matter. This method of bombarding a stationary target by a beam of particles has become extremely popular. The higher

we go in the energy of the beam, the deeper we probe the target. Indeed, modern high energy electron scattering experiments have shown that protons and neutrons themselves contain small hard constituents, the quarks.

1.1 Colliders

The main disadvantage of the fixed target method is that most of the energy of the initial beam is used in the motion of the final products. In order to put more of the initial kinetic energy into final state mass, the idea of colliding beams has emerged. Two beams of particles, usually of equal energy, collide and produce new particles. The idea of sitting in the center of mass system and watching this process pleases and excites any physicist. For some particular purposes colliding beams of unequal energy are used.

Initially, electrons and positrons, or just electrons, were used as the beam particles. The pioneers in this method being experiments performed at the laboratories in Stanford, Frascati, Orsay and Novosibirsk [1]. This e^+e^- method has brought, and continues to bring, many physics results.

Unfortunately charged particles radiate when accelerated. The energy of this so called synchrotron radiation grows as the fourth power of the Lorenz factor $\gamma = E/m$, where E is the energy of the accelerated particle and m is its mass. Accelerating electrons to arbitrarily high energies becomes very difficult.

The obvious solution to this problem is to take more massive particles, such as protons and antiprotons which are 2000 times heavier than electrons. This $p\bar{p}$ method has allowed us to reach a center of mass energy of 1.8 trillion electron-Volts (TeV),

the highest energy in the world so far, at the Fermi National Accelerator Laboratory in Batavia, Illinois. This collider is whimsically referred to as the Tevatron [2].

1.2 Collider Detector Organization

In a colliding beam experiment we sit in the center of mass frame and there is a pleasing axial symmetry around the beam axis; the detectors that detect the results of the collision are axially symmetric. Usually they consist of a central tracking system, which tracks the charged products, then a calorimeter system, which measures the energy of the products, and finally, a muon system, which is also a tracking system, but muons are the only charged particles which can survive as far as this system. There are two detectors at the Tevatron collider, CDF (Collider Detector at Fermilab) [3] and DØ (named after its accelerator interaction point)[4] .

The experiment described in this thesis was performed with the DØ detector at Fermilab.

1.3 Quarks and Leptons

As we presently understand it, matter is built from two types of fundamental particles, quarks and leptons, each of which exists in three so-called generations (see Table 1.1) [5]. Each generation is represented by a lepton doublet and a quark doublet and the higher the generation, the heavier and less stable are the particles. Each particle has its antiparticle. Quarks and leptons have spin 1/2 and obey Fermi statistics.

	name	symbol	charge	mass, GeV	type
first generation	up	u	2/3	4×10^{-3}	quark
	down	d	-1/3	7×10^{-3}	quark
	e - neutrino	ν_e	0	$< 5.1 \times 10^{-9}$	lepton
	electron	e	-1	5.1×10^{-4}	lepton
second generation	charm	c	2/3	1.5	quark
	strange	s	-1/3	0.2	quark
	μ - neutrino	ν_μ	0	$< 2.7 \times 10^{-4}$	lepton
	muon	μ	-1	0.106	lepton
third generation	top (truth)	t	2/3	> 131	quark
	bottom (beauty)	b	-1/3	4.4	quark
	τ - neutrino	ν_τ	0	$< 3.1 \times 10^{-2}$	lepton
	tau	τ	-1	1.78	lepton

Table 1.1: Three generations of quarks and leptons

The first generation lepton doublet consists of the electron and its neutrino. Higher lepton doublets contain the muon or the tau, the electron siblings, and the corresponding neutrinos. The electron, muon and tau have electric charge -1, in the nomenclature of particle physics. The neutrinos are weakly interacting neutral particles which are likely to escape from any detector.

The so-called up (u) and down (d) quarks form the lowest quark doublet. The next doublet consists of a strange (s) and a charm (c) quark. The third (and currently believed to be the last) doublet contains a not-yet-discovered top or truth (t) quark and a bottom or beauty (b) quark. The u, c and t quarks all have charge 2/3 (i.e. 2/3 times the magnitude of the electron charge) and d, s and b quarks all have charge -1/3.

All the particles from the higher generations, except (according to current thinking) the massless neutrinos, eventually decay into product particles built from the lowest generation.

1.4 Fundamental Forces

The fundamental particles interact with each other via four fundamental forces: strong, electromagnetic, weak and gravitational [1]. Each force is believed to be transmitted by its own gauge boson – another class of elementary particle. Gauge bosons have spin 1 and obey Bose statistics. The exception to this is gravitation. The graviton, the assumed particle carrier of gravitation, has spin 2 and has never yet been observed.

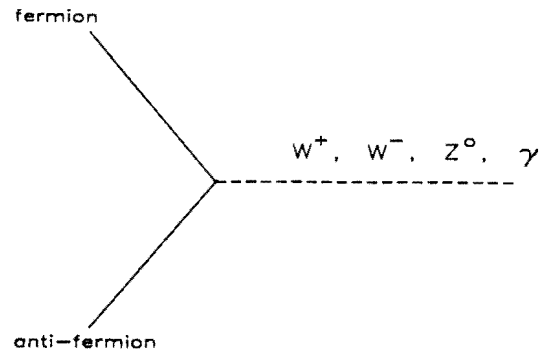

Figure 1.1: Electro-weak doublet interaction with W and Z bosons and the photon

Every massive object interacts gravitationally, but this force is by far the weakest one and does not count for much in the elementary particle domain.

Every electrically charged particle interacts electromagnetically. This interaction is transmitted by the photon (γ), a massless and neutral particle.

The weak interaction is transmitted by massive W- and Z-bosons, which couple to fermion doublets (Figure 1.1). Actually, currently acceptable theoretical thinking indicates that the W- and Z-bosons and photons are together the transmitters of the electro-weak interaction, but because the photon happens to be the only massless, neutral and thus stable carrier, the electromagnetic component is a long distance and much more well known one than the weak component.

Quarks (q) interact with each other strongly. The strong "charge" is referred to as color. Each quark is supposed to have one of three colors: red, blue or green. Antiquarks are antired, antiblue or antigreen. Leptons, gravitons and electro-weak bosons are colorless.

The transmitter of the strong interaction is the gluon (g) (Figure 1.2 a). As it is also a massless, spin 1 particle, it is somewhat similar to the photon; however because

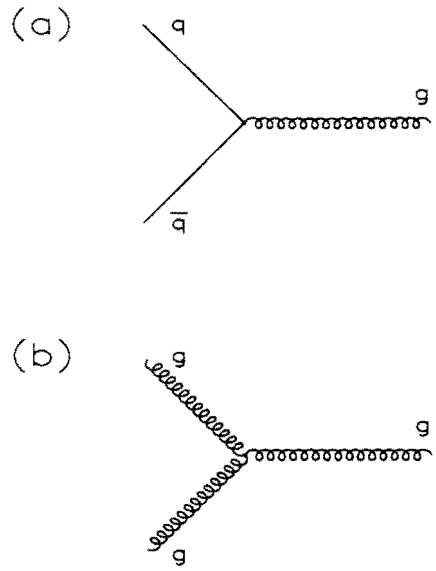

Figure 1.2: (a) Quark-gluon interaction vertex; (b) Triple gluon vertex

it has color itself it can be coupled to another gluon (Figure 1.2 b). This makes the strong force more complicated than electro-weak force. Also the constant of the strong interaction is much larger than that of the electromagnetic interaction. All this leads to the fact that the strong interaction, unlike the electromagnetic interaction, increases with the distance between the interacting objects and therefore, quarks never appear in a free state. When two quarks are pulled apart, at some point the potential energy of their interaction becomes large enough to spontaneously form a quark-antiquark pair, each of which forms bound colorless states with the initial quarks. The process by which quarks become bound colorless states is called fragmentation. The particles formed by quarks are called hadrons. The bound state of a quark and an antiquark is usually referred to as a meson or quarkonium.

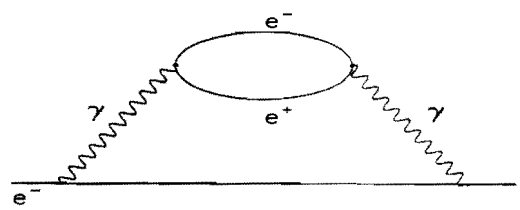

Figure 1.3: Lowest order QED vacuum polarization diagram

1.5 Perturbative QED and QCD

The coupling constant of the electromagnetic interaction is small: $\alpha = 1/137$. This has allowed theoreticians to build the pertubative theory of Quantum Electro Dynamics (QED) [5]. In other words, to expand the exact equations in powers of α. Actually α is not an exact constant. During its life, a charged particle, say an electron, can emit and absorb virtual photons. Photons themselves can form a virtual electron-positron pair (Figure 1.3). This effect is called vacuum polarization. The initial electron attracts positrons from its own cloud, thus screening its own charge. So its charge seems smaller when probed from longer distances, or in other words at smaller energies. The higher we go in energy, the stronger the electromagnetic interaction becomes. This means that the coupling constant must be renormalized for different energies. According to QED, if the value of α was obtained in a measurement with a typical momentum transfer Q_0, then its value at a momentum transfer Q will be:

$$\alpha(Q^2) = \frac{\alpha(Q_0^2)}{1 - \frac{\alpha(Q_0^2)}{3\pi}\ln(Q^2/Q_0^2)}.$$

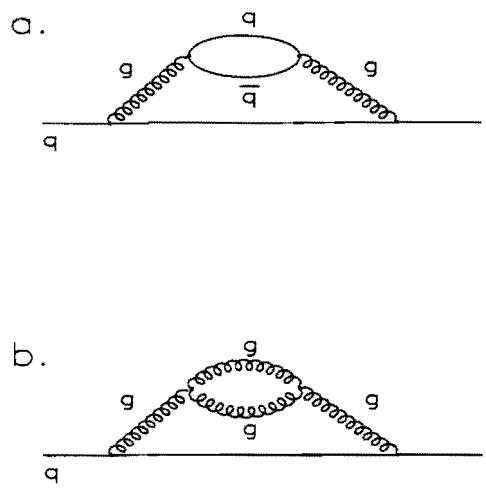

Figure 1.4: Lowest order QCD vacuum polarization diagram: (a) quark-antiquark loop; (b) gluon loop

The QED theory has explained and predicted many physics results.

The temptation is strong to apply the same technique to Quantum Chromo-Dynamics (QCD) [6], the theory that describes the strong interactions. However, the typical value of the constant of the strong interaction α_s is about 0.2 and that is not a truly small enough parameter that can be used in an expansion. Often the next term in the expansion is bigger than the previous one. Another problem is that gluons have color and can interact with each other. So, not only quark-antiquark loops (Figure 1.4 a) contribute to the vacuum polarization, but also gluon loops (Figure 1.4 b). This leads to the fact that α_s decreases as the energy increases:

$$\alpha_s(Q^2) = \frac{12\pi}{(33-2f)\ln(Q^2/\Lambda^2)},$$

where $\Lambda = 0.2$ GeV is a renormalisation parameter and f is the number of the quarks contributing to the loop.

So, the interaction between quarks can be assumed small only for a very large

momentum transfer. This effect is called asymptotic freedom. Only in the case of large masses and large momentum transfer is it possible to use perturbative QCD.

1.6 Charmonium system

The c-quark is considered to be the lowest mass quark whose physics can be described by perturbative QCD. The combination of c and $\bar{c}$ quarks can form a bound system, called charmonium [7]. In a manner similar to that of the hydrogen atom, a pe^- bound state, the $c\bar{c}$ system may exist in states with different quantum numbers. Each of these $c\bar{c}$ states is identified with a specific particle (Figure 1.5). The lowest charmonium state, $\eta_c(1s)$ has orbital angular momentum $L = 0$, and spin $S = 0$, hence its total angular momentum J is 0. The next state is $J/\psi(1s)$, perhaps the most famous hadron. It has $L = 0$ and $S = J = 1$, the quantum numbers of a photon, which is why it can be produced directly in an e^+e^- collision. This has allowed very careful studies of this particle to be performed. The J/ψ was first discovered in two experiments simultaneously, one was at an e^+e^- collider[8], the other a fixed target hadroproduction experiment[9]. The discovery of this particle was the first experimental indication that there exist more then three quarks, as had been believed previously. The next three charmonium states (1p) have $S = 1$ and $L = 1$ and these can sum up to three possible values of the total angular momentum $J = 0, 1, 2$. These correspond to the $\chi_{c0}(1p)$, $\chi_{c1}(1p)$, $\chi_{c2}(1p)$ states, respectively, each of which can decay to the J/ψ state electromagnetically. These states are rarely produced directly in e^+e^- annihilation, but may be produced in a $p\bar{p}$ collision either directly or via the hadronic decay of a b-quark. The study of χ_c production in

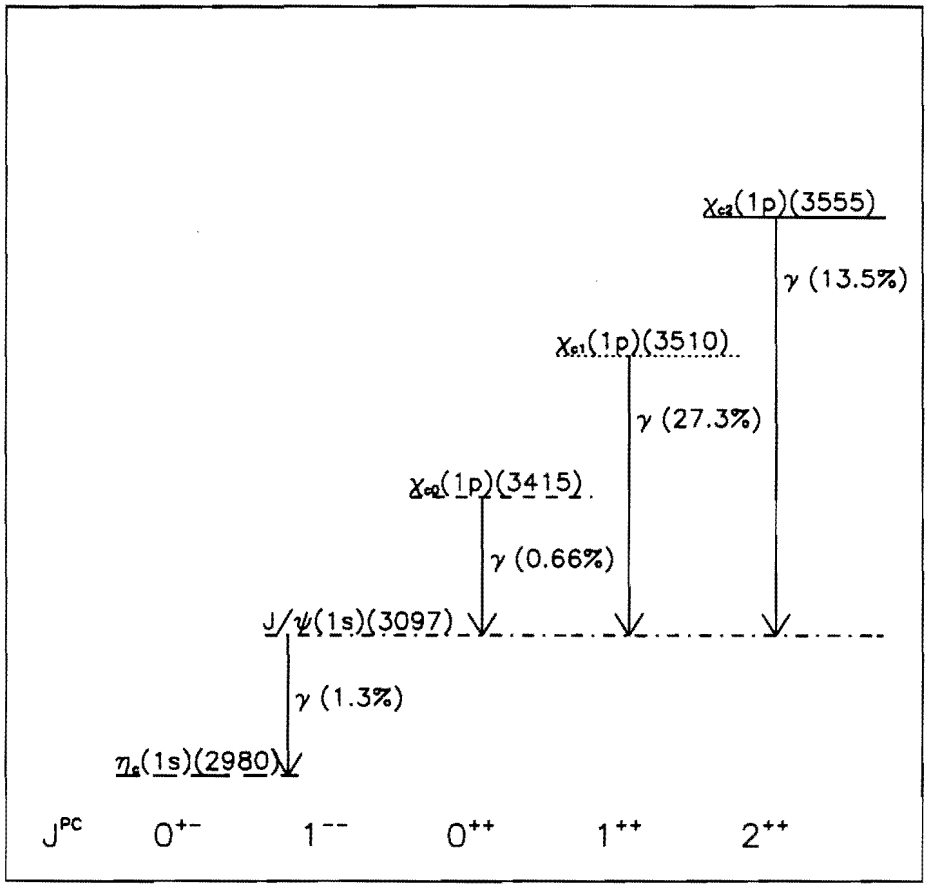

Figure 1.5: The charmonium system. J denotes the total angular momentum of a particular state, P is its P-parity and C is its C-parity. The first symbol in brackets next to the name of a state indicates its radial and orbital quantum numbers in the atomic notation, the second number in brackets is the mass of a particle. The arrows indicate possible radiative decays and the numbers in brackets next to the γ show the branching ratios of these decays.

$p\bar{p}$ experiments provides an important testing ground for perturbative QCD. The natural way to observe them is through their decay to $J/\psi + \gamma$, with J/ψ being then identified in $\mu^+\mu^-$ decay. The branching ratio of $J/\psi \to \mu^+\mu^-$ is about 6% [7], but the signature of this process is pretty clean. This is crucial in $p\bar{p}$ experiments, which suffer from large backgrounds. In the next chapter we discuss alternate mechanisms of charmonium production in $p\bar{p}$ collisions.

1.7 Outline of the Thesis

In this thesis we study the production of the χ_c meson in $p\bar{p}$ collisions using the DØ detector at the Fermilab Tevatron. We identify χ_c through the decay chain

$$\chi_c \to J/\psi\, \gamma, \quad J/\psi \to \mu^+\, \mu^-$$

at a center of mass energy 1800 GeV.

Chapter 2 presents a theoretical overview. In particular, different production mechanisms of the charmonium states and their characteristic patterns are discussed.

In Chapter 3 the apparatus - the Tevatron $p\bar{p}$ collider and the DØ detector - is discussed with the emphasis on muon and photon identification and their kinematic parameters resolution. The reconstruction algorithms for different particle identifications are described.

In Chapter 4 the kinematics of the final products is examined. Estimates are derived for the expected mass resolutions of the J/ψ and χ_c states. The experimental goals are stated.

Chapter 5 describes the selection of events with two muons and a photon in the final state. The number of J/ψ and χ_c is determined for the final event sample. Background processes are discussed.

In Chapter 6 the acceptances and reconstruction efficiencies for two muons and a photon are obtained.

In Chapter 7 the total production cross section of the χ_c is determined. The relative fractions of the different production mechanisms are obtained and their P_t dependance is discussed. The result is compared to similar measurements performed by the CDF experiment.

Chapter 8 describes the upgrade of the DØ detector and the resulting future potential for charmonium physics.

Chapter 2

Theoretical Overview

2.1 The Production of Charmonium States

In this chapter we describe the production of different quantum states formed by two charm quarks in a $p\bar{p}$ collision.

First, the assumptions that are used in this discussion will be considered. Then various production mechanisms of charmonium states will be investigated. Finally, we shall discuss the general patterns of high transverse momentum (P_t) charmonium production.

2.2 Assumptions

2.2.1 The Parton Model

Hadronic collisions involving the production of a high P_t state, can be described by the parton model [10]. In this model protons or antiprotons are not considered

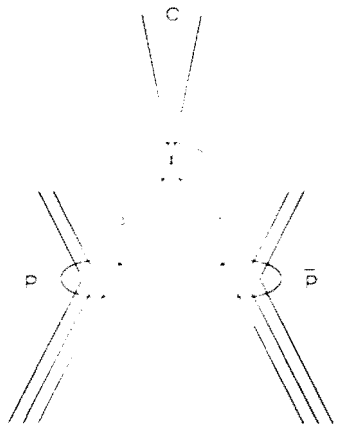

Figure 2.1: The parton scattering representation of a proton-antiproton collision

to be pointlike particles. Rather, each of them consists of three valence quarks and a cloud of sea quarks and gluons, that emerge as a result of the interaction of the valence quarks with each other. The quarks and gluons that constitute the proton are called partons. When a proton and an antiproton collide, a parton from the proton interacts with a parton from the antiproton, producing an arbitrary quantum state. The parton scattering representation of a proton-antiproton collision is illustrated in Figure 2.1, where the proton and the antiproton carry the momentum P_p and $P_{\bar{p}}$ respectively, and parton a represents the proton and parton b the antiproton.

Each parton carries some fraction of the hadron momentum,

$$x_a = P_a/P_p \ , \quad (0 \leq x_a \leq 1).$$

The probability of a parton to carry the momentum fraction x_a obviously is a function of x_a and is called the structure function $f_{a/p}(x_a)$[11]. Similarly for $x_b = P_b/P_{\bar{p}}$. The structure functions are usually measured in the lepton-proton scattering experiments where a pointlike lepton probes the structure of the proton.

The cross section for producing some final state C in the reaction

$$p + \bar{p} \rightarrow C + X,$$

where X represents all other particles produced in the reaction, is obtained by multiplying the subprocess cross section $\hat{\sigma}$ for $a + b \rightarrow C + X$ by $dx_a\ f_{a/p}(x_a)$ and $dx_b\ f_{b/\bar{p}}(x_b)$, summing over parton types and integrating over x_a and x_b. As each of the partons carries color, a correction by a color-averaging factor D_{ab} must be done. Thus, for the total cross section we obtain:

$$\sigma(p\bar{p} \rightarrow C) = \sum_{a,b} D_{ab} \int dx_a\ dx_b \cdot f_{a/p}(x_a) f_{b/\bar{p}}(x_b)\ \hat{\sigma}(ab \rightarrow C).$$

Each quark can have one of three colors, and each gluon, carrying two color indices, can have one of eight color combinations. The color averaging factor D_{ab} is the inverse of the number of possible color combinations. Hence, the color averaging factors for quarks and gluons are:

$$D_{qq} = D_{q\bar{q}} = 1/9, \quad D_{qg} = 1/24, \quad D_{gg} = 1/64.$$

For the particular case of charmonium (ch) production the cross section can be expressed as

$$\sigma(p\bar{p} \rightarrow ch + X) \sim K \sum_{a,b} D_{ab} \int dx_a dx_b f_{a/p}(x_a) f_{b/\bar{p}}(x_b) \hat{\sigma}(a + b \rightarrow ch + X),$$

where K is an enhancement factor to correct for non-leading order QCD effects [12].

Since the final result is expressed in terms of the parton-parton cross section $\hat{\sigma}$, we can forget for a while about protons and antiprotons and talk about partons.

The most important property of the structure functions of the sea partons is their behaviour at low x: viz., the lower the energy of the parton, the higher is the

probability of its formation. In other words, the lower the parton x, the higher is the value of the parton structure function. Hence, partons with the lowest possible x contribute the most to any production process.

The threshold in x for charmonium production is set by the mass of the charmonium state M_{ch} :

$$x_{min} = M_{ch}/E_{beam},$$

where $M_{ch} = 3.1$ GeV/c^2 and E_{beam} is the energy of the proton or antiproton beam. In the case of the Tevatron, $E_{beam} = 900$ GeV. The higher the energy of the beam, the lower x we are probing in the production process. For example, charmonium production at the Tevatron is probing x down to:

$$x \approx 3.1/900 \approx 0.003.$$

Partons with the lowest possible x contribute the most to the production of a given particle. Hence, its mass sets the scale for the typical momentum transfer in the reaction.

2.2.2 The Coordinate System and Kinematic Variables

When proton and antiproton collide they have the same absolute value of the momentum, but are moving in the opposite directions. Thus, the laboratory system is, at the same time, the center of mass system for the colliding particles. The beam axis is an obvious axis of symmetry in this system and that is why the coordinate system used for the discussion of the $p\bar{p}$ collision kinematics, has its z axis along the beams.

We use a right-handed coordinate system with the z-axis along the proton direction and y pointing up. ϕ denotes the azimuthal angle and θ – the polar angle, see Figure 2.2.

For the kinematic parameters of any particle the following notation is used:

- m denotes the mass of the particle;
- E its energy;
- $\vec{P}$ its momentum vector, where P_x, P_y, P_z are its cartesian components. If ϕ is the azimuthal angle and θ – the polar angle of the particle direction, then the components of the momentum obey the following relations:

$$P_x = P\ Sin(\theta)\ Cos(\phi),$$

$$P_y = P\ Sin(\theta)\ Sin(\phi),$$

$$P_z = P\ Cos(\theta),$$

$$P_t = P\ Sin(\theta),$$

  where P is the absolute value of the momentum, and P_t is the transverse momentum.

  The following relation between mass (expressed in GeV/c^2), energy (in GeV) and momentum (in GeV/c) of the particle is valid:

$$E^2 - P^2 = m^2.$$

- an important parameter used in the discussions of the kinematics of the $p\bar{p}$ collision is rapidity. It is defined as:

$$y = 1/2\ \ln((E + P_z)/(E - P_z)).$$

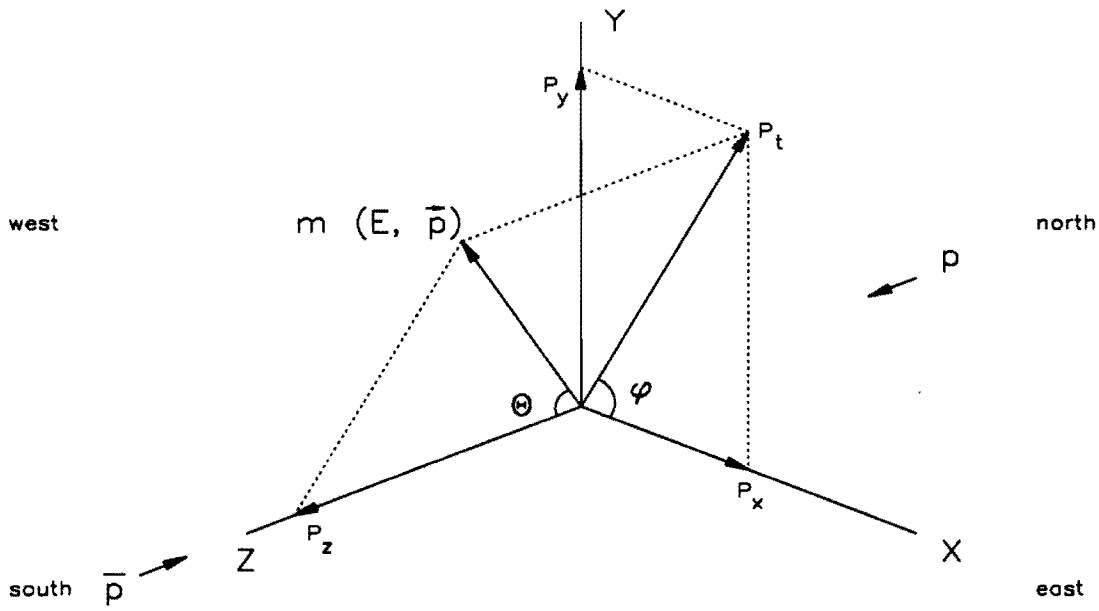

Figure 2.2: DØ coordinate system

In the ultra relativistic limit ($m/E \rightarrow 0$) it can be approximated by the pseudo-rapidity, defined as $\eta = -\ln(\tan(\theta/2))$. Pseudo-rapidity is a pure geometrical parameter and it is simple to calculate. It is important to note that $\eta = 0$ for $\theta = \pi/2$ and $\eta \rightarrow \pm\infty$ for $\theta \rightarrow 0,\ \pi$.

2.2.3 Perturbative QCD

Perturbative QCD can be used for the calculation of the quarkonium production cross section when the strong coupling constant $\alpha_s(Q^2)$, where Q is the typical momentum transfer in the reaction, is much less than 1.

In the case of charmonium production, a typical value of Q is the mass of the charmonium system. This is 3.1 GeV. The renormalization parameter Λ is 0.2 GeV [1]. The number of quark flavors (f) that contribute to the vacuum polarization loop is the number of quarks having mass below the c-quark mass. Then,

$$\alpha_s(Q^2) = \frac{12\pi}{(33 - 2f)\ln(Q^2/\Lambda^2)} = 0.25 \ .$$

Assuming 0.25 to be much less than 1, we can therefore calculate the quarkonium production cross section using perturbative QCD.

2.2.4 Fragmentation

Colored partons – quarks and gluons – can be regarded as free only during a hard collision, after which they organize themselves into colorless states called hadrons. This process is referred to as fragmentation or hadronization [13]. As a result of this process a flux of hadrons, a so-called jet, is formed.

The probability of parton k to produce hadron h depends on the energy fraction z, where

$$z = E_h/E_k, \quad 0 < z < 1.$$

The probability of finding hadron h in the range z to $z + dz$ is defined as $D_k^h(z)dz$, where D_k^h is called the k-to-h fragmentation function.

Some of the mechanisms of charmonium production involve the fragmentation of a hard parton [14], [15], [16], [17], [18]. For the particular case of charmonium production via fragmentation, the cross section can be expressed as a product of the parton k production cross section $\sigma(p\bar{p} \to k)$ and the fragmentation function of k-to-charmonium D_k^{ch}, integrated over z from 0 to 1, and summed over parton types:

$$\sigma(p\bar{p} \to ch + X) = \sum_k \int_0^1 dz \sigma(p\bar{p} \to k)(E/z) D_k^{ch}(z).$$

For the production of light hadrons via fragmentation, the effects of soft gluon emission by any of the secondary partons are large. Therefore, the fragmentation functions of the light hadrons are difficult to calculate and they are usually measured experimentally. For the relatively heavy charmonium, however, soft gluon emission effects can be neglected, and the fragmentation functions for charmonium production can be calculated within perturbative QCD [19], [20].

2.2.5 The Nonrelativistic quarkonium model

When, in the quarkonium rest frame, the relative momentum q of the quarks is small with respect to the quark mass m_c, we can describe quarkonium as a nonrelativistic bound state. The mass of the charmonium system is about 3.1 GeV/c^2 [7], while the mass of the c-quark is 1.5 GeV/c^2. Thus, the energy of motion of the two

quarks is small, and we can assume:

$$q << m_c.$$

2.2.6 Assumption Summary

Summarizing these assumptions then, in our following discussion of the different charmonium production mechanisms we will be using the parton model, perturbative QCD, parton fragmentation and the nonrelativistic quarkonium model.

2.3 Mechanisms of charmonium production in hadronic collisions

2.3.1 Direct Hadroproduction

The direct mechanisms of charmonium production have been discussed many times [21], [22], [23], [24], [12], [25]. The $O(\alpha_s^2)$ Feynman diagram for charmonium production is shown in Figure 2.3.

Gluon fusion predominates at this level. Quark and antiquark can produce charmonium either in electromagnetic annihilation, which is suppressed by α^2/α_s^2, or at the $O(\alpha_s^3)$ level.

Since charmonium is the only particle produced in the $O(\alpha_s^2)$ gluon fusion it has no partner to compensate its momentum. Therefore, this mechanism produces states with low P_t determined by the transverse motion of the partons inside the proton or antiproton; it is small compared to the longitudinal momentum. This means, that the angle between the beam axis and the direction of the charmonium is small and

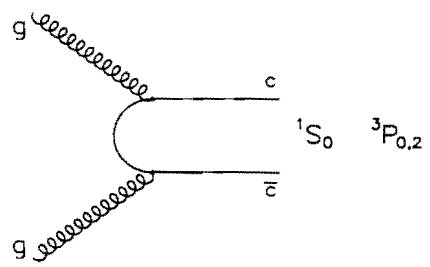

Figure 2.3: The $O(\alpha_s^2)$ Feynman diagram for charmonium production. $^1S_0$ represents η_c, $^3P_{0,2}$ represents $\chi_{c0,2}$.

therefore the products of charmonium decay are likely to escape from the detector along the beam axis.

At the $O(\alpha_s^3)$ level there are several possible contributions. Most important are the two-by-two scattering processes depicted in Figures 2.4 and 2.5. In these processes the momentum of the charmonium is compensated by the momentum of the final state parton, which materializes as a jet and which is almost back-to-back with the charmonium. Therefore, these mechanisms tend to populate the higher P_t region. Since the only jet in such events tends to be in the other hemisphere, there is no jet in the neighbourhood of the charmonium. In other words, the charmonium is isolated.

A crucial role is played by the quantum numbers of the charmonium final state. For example, C-parity, which is conserved in the strong interactions. Since the gluon has negative C-parity, in order to form a state with negative C-parity an odd number of gluons is needed. An even number of gluons forms a state with positive C-parity.

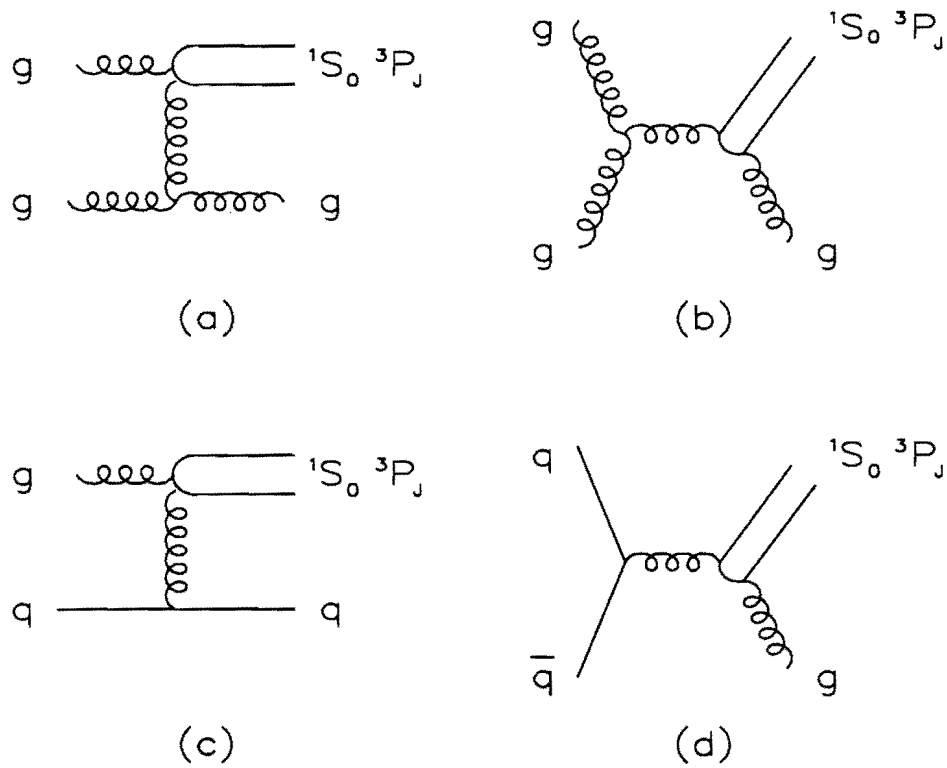

Figure 2.4: The $O(\alpha_s^3)$ Feynman diagrams for charmonium production. $^1S_0$ represents η_c, ^3P_J represents χ_{cJ}.

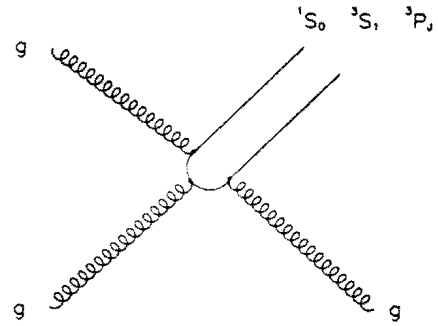

Figure 2.5: Charmonium production via triple gluon vertex. $^1S_0$ represents η_c, ^3P_J represents χ_{c_J}, $^3S_1$ represents J/ψ.

In particular, in processes with a two gluon vertex, the states with positive parity ($^1S_0$ (η_c) and ^3P_J (χ_J)) can be produced. Whereas, for the negative parity state production ($^3S_1$ (J/ψ)) a three gluon vertex is needed. This leads to the fact that direct J/ψ production is suppressed with respect to η_c and χ_J production.

2.3.2 b-quark Decay

The energy of the Tevatron is high enough for the production of b-quark pairs. The diagrams for b-quark production in a $p\bar{p}$ collision are shown in Figure 2.6 [26]. After the b-quark is produced, it is fragmented into a B-meson. A simple example of this b-quark fragmentation process is shown in Figure 2.7. After this, the B-meson decays with a characteristic mean lifetime of $\approx$ 1 ps. To first approximation, the effects of the light quark in the B-meson can be neglected and the b-quark can be regarded as free. In this case the light quark is called a spectator.

Most of the time, a b-quark decays into a c-quark plus a W^--boson. The W^--

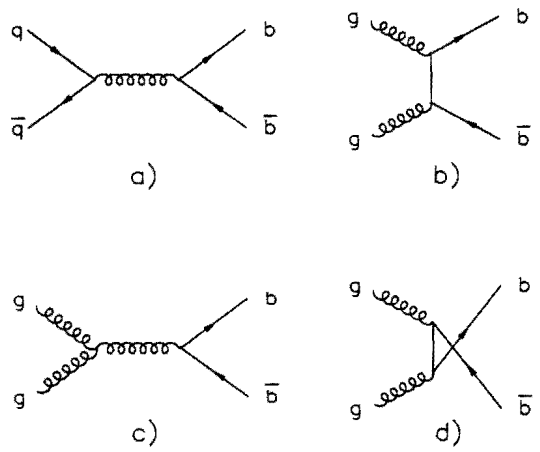

Figure 2.6: Feynman diagrams for b-quark production in a $p\bar{p}$ collision.

boson couples to an electroweak doublet, consisting of particles with mass smaller than the mass of the b-quark. Possible doublets are a $\bar{c}$-quark plus s-quark, a $\bar{u}$-quark plus d-quark, and all three lepton doublets. Both quark doublets have three color possibilities. So, all together we have 9 possible channels for the W-decay and therefore, in 33% of the cases the W-boson decays into a $\bar{c}$ and s-quark doublet (see Figure 2.8). The c-quark from the b-decay and the $\bar{c}$ from the W decay can form a charmonium bound state. This happens only when the $\bar{c}$ has the same color as the c-quark from b-decay, or in 1/3 of the cases. This effect is called color suppression. We may therefore expect an 11 % branching ratio of b-decay to a charmonium state.

Actually, a bound state is not always formed even when the correct color combination is produced. The rate of charmonium production in b-decay is discussed in

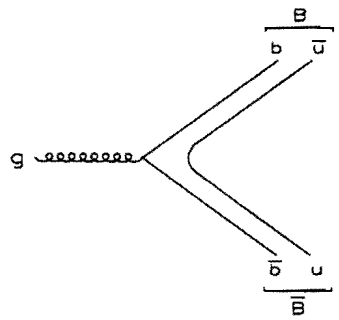

Figure 2.7: Example of b-quark fragmentation.

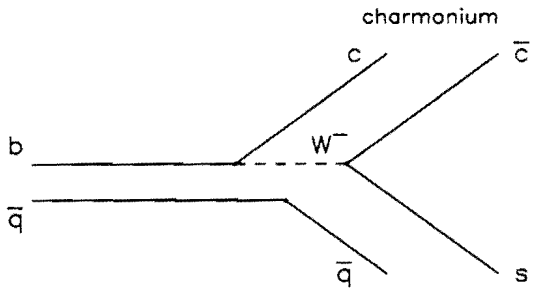

Figure 2.8: Charmonium production in b-quark decay.

references [27], [28], [29], [30], [31], [32].

The experimentally measured inclusive branching ratio of B-meson decays to charmonium states is $1.12 \pm 0.16\%$ [7]. Nevertheless, the rate of b-quark production is high enough that this represents a significant mechanism of charmonium production. Moreover, charmonium produces clean signatures in the detector and thus can be considered as a valuable tag of the b-quark.

The momentum of one b-quark is compensated by the momentum of the other. Thus the b-quarks are produced approximately back-to-back with respect to each other. Similar are the B-mesons into which the b-quarks fragment. The products of the B-meson decay follow the direction of their parent and are in the same hemisphere. The charmonium from b-decay is therefore accompanied by a hadron jet and is nonisolated.

The quantum numbers of the charmonium state produced in B-decay are not yet well determined. The relative production of χ_c and J/ψ states in B-decay measured in several experiments is shown in table 2.1 together with different theoretical predictions. Statistics are limited and additional experimental information is desperately needed.

2.3.3 Gluon and c-quark Fragmentation

Recently a new mechanism of charmonium production at large transverse momentum in $p\bar{p}$ collisions has been suggested [14], [15], [16], [17], [18]. The mechanism involves the fragmentation of a gluon or a c-quark, produced as a result of hard $p\bar{p}$ scattering, into a charmonium state. Such processes are of higher order in α_s, but are quite significant for sufficiently high P_t. The Feynman diagrams for charmonium

Source	$\frac{Br(b \to \chi_{c1}\ X)}{Br(b \to J/\psi\ X)}$
L3 (experiment) [33]	1.92 ± 0.82
ARGUS (experiment) [34]	0.94 ± 0.41
J.H.Kühn *et al* [27], [28] (theory)	0.27
G.T.Bodwin *et al* [32] (theory)	0.70 ± 0.35

Table 2.1: The relative production of χ_c and J/ψ states in B-decay

production via fragmentation are shown in Figure 2.9.

The parton that fragments itself to charmonium is usually produced in a 2-to-2 process. Thus, the momentum of the second parton compensates the momentum of this one. Similarly to charmonium from b-decay, charmonium from parton fragmentation is accompanied by a jet. This jet is in the neighbourhood of the charmonium, hence the charmonium is nonisolated. This is a very important feature that helps to distinguish between the different mechanisms of charmonium production.

2.4 The Production Pattern

The final results for the cross sections of charmonium production can be expressed analytically and these are presented in the Appendix. These formulae can be analysed in a graphical way. The only experimentally observable characteristics are the kinematic parameters (momenta and angles) of the final products in the reac-

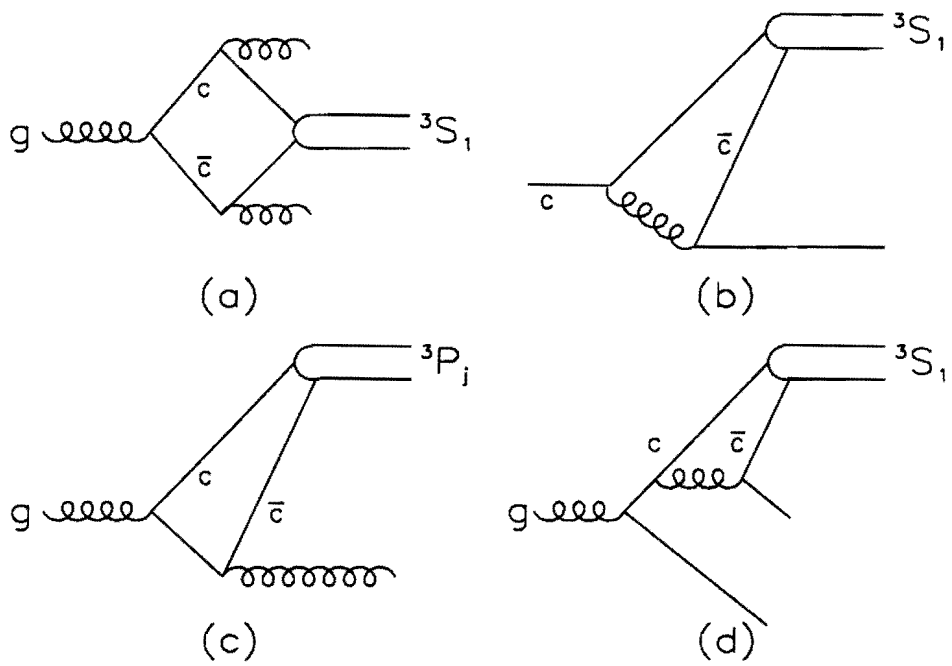

Figure 2.9: The Feynman diagrams for charmonium production via fragmentation of a gluon (a,c,d) or a c-quark (b). ^3P_J represents χ_{c_J}, $^3S_1$ represents J/ψ.

tion. The P_t dependance of the differential cross section of charmonium is of special interest.

The dependence of the χ_c and J/ψ production cross section versus P_t for the different production mechanisms discussed above is shown in Figure 2.10.

Several things are useful to note. The differential cross section $(\frac{d\sigma}{dP_t^2})$ scales asymptotically like P_t^{-6} for hard scattering processes compared to P_t^{-4} for fragmentation mechanisms and b-decay [20]. Therefore, fragmentation becomes more important for high P_t production; the two extra powers of P_t overcome the suppression by α_s. The P_t-dependence is very important in distinguishing the mechanisms of charmonium production.

Also, χ_1 production can be seen to dominate over χ_2 by a factor of about 10. Since direct J/ψ production is suppressed by another order of magnitude, most of the observed J/ψ comes from χ_1 decay.

Finally, to evaluate the possibility of studying charmonium production at the DØ experiment, let us do some rough estimations for the expected number of J/ψ and χ_c events. The total theoretically predicted cross section for inclusive χ_c production at $\sqrt{s}$ = 1800 GeV, and $P_{t\,J/\psi} > 5$ GeV/c is 196 nb [12]. In the DØ experiment we observe $J/\psi \rightarrow \mu^+\mu^-$, therefore we must multiply this by the appropriate decay branching ratio of 6 %. This yields 11.8 nb. With the integrated luminosity of 15 pb^{-1}, and a realistic acceptance times efficiency for muon detection of 1 %, we may expect

$$11.8 \text{ nb } \times 15 \times 10^3 \text{ nb}^{-1} \times 1\% \approx 1500$$

J/ψ events in our event sample. Assuming 10 % for photon reconstruction efficiency, we should obtain some 150 χ_c events.

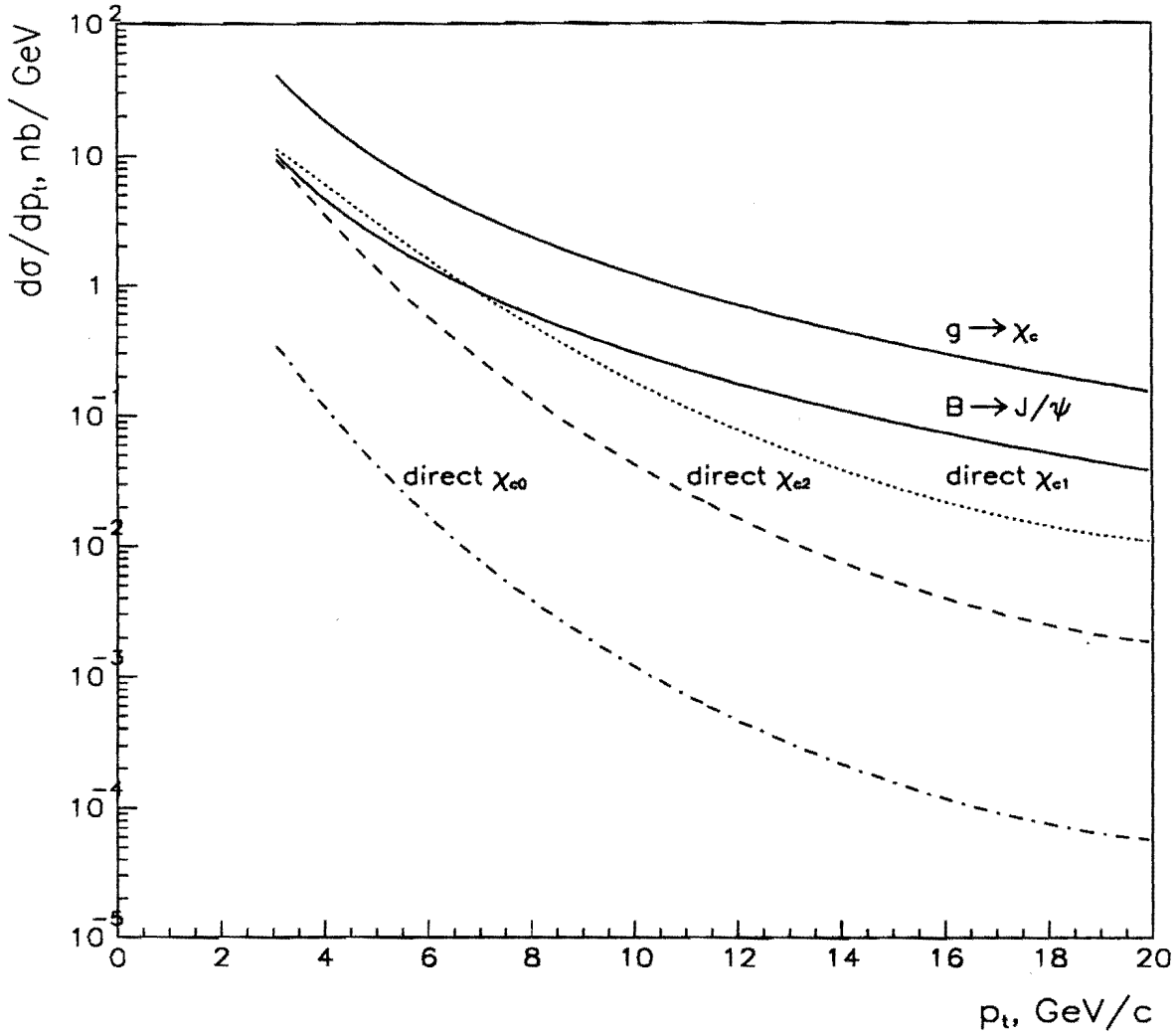

Figure 2.10: The dependence of the χ_c and J/ψ production cross section versus P_t for the different production mechanisms: direct charmonium production, charmonium production from b-decay and charmonium production from gluon fragmentation

2.5 Summary

1. High P_t charmonium production probes the parton structure functions down to $x \sim 0.003$, and hence it gives important information about parton structure functions at very low x.

2. High P_t charmonium production in $p\bar{p}$ collision can be described in terms of perturbative QCD and thus it is an important testing ground for this theory.

3. There are three possible charmonium production mechanisms, each of which exhibits characteristic patterns:

   - direct charmonium production mechanism. The differential cross section is approximately proportional to P_t^{-6} and the charmonium is isolated;
   - the fragmentation of a hard gluon or c-quark. The differential cross section is approximately proportional to P_t^{-4} and the charmonium is accompanied by a jet;
   - the decay of a b-quark. The differential cross section is approximately proportional to P_t^{-4} and the charmonium is accompanied by a jet;

4. The dominant charmonium state is χ_1, and this is produced by hard scattering and parton fragmentation mechanisms.

5. The relative production of χ_c and J/ψ in b-decay is uncertain.

6. There should be an adequate number of events produced to make it possible to observe χ_c at DØ through the decay chain:

$$\chi_c \rightarrow J/\psi + \gamma \quad J/\psi \rightarrow \mu^+ + \mu^-.$$

Chapter 3

Experimental Apparatus

The experiment discussed in this work was performed with the DØ detector [4] at the Tevatron $p\bar{p}$ collider [2], at Fermi National Accelerator Laboratory in Batavia, Illinois.

3.1 The Tevatron $p\bar{p}$ collider

The Tevatron (Figure 3.1) is the highest energy particle collider in the world. The energy of the colliding proton and antiproton beams is 0.9 trillion electron-Volts (TeV) each. The total energy in the center of mass is 1.8 TeV. When the two beams collide, some of their energy is spent on the production of new particles, some of them with high mass and high transverse momentum.

The higher the energy of the beams, the higher can be the mass of the products. Hence, the energy of the beams is the major parameter of any collider. In order to minimize the energy losses due to synchrotron radiation, it is preferable to have as large a circumference as possible. The circumference of the Tevatron is 6.28 kilometers.

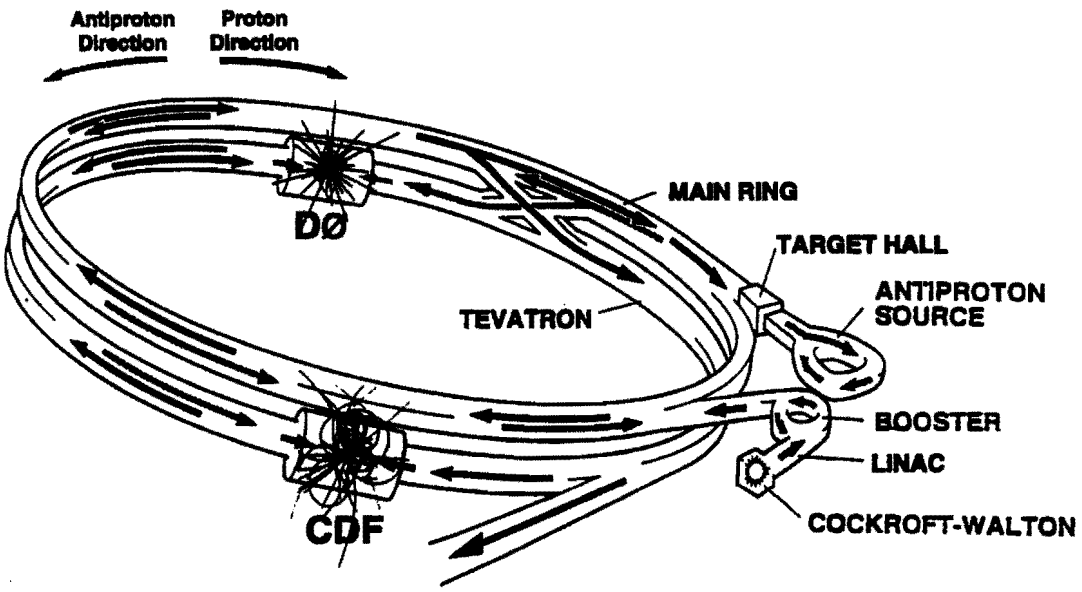

Figure 3.1: The Tevatron collider with two high luminosity interaction points: DØ and CDF

Another very important collider parameter is the so-called luminosity (L). By definition, the luminosity is the number of events of a given process produced per unit of time (N) divided by the cross section for this process (σ):

$$L = \frac{N}{\sigma}.$$

Luminosity is measured in the units $\mathrm{sec}^{-1}\mathrm{cm}^{-2}$. It is a characteristic of the collider and is totally determined by the following beam parameters:

- the luminosity is higher, when there are more particles in the proton and antiproton beams, N_p and $N_{\bar{p}}$, respectively. For the Tevatron

$$N_p = 10 \times 10^{10} \quad \text{protons per bunch,}$$

$$N_{\bar{p}} = 7 \times 10^{10} \quad \text{antiprotons per bunch.}$$

- the smaller the transverse geometrical area of the interaction point (S), the higher the luminosity. For the Tevatron

$$S = 4 \times 10^{-4}\mathrm{cm}^2.$$

- the smaller the time between the beam interactions (τ) the higher the luminosity. In order to minimize the time between collisions, there are six proton and antiproton bunches circulating in the Tevatron simultaneously. The time between collisions at some collision point is the circumference of the Tevatron (P), divided by the speed of the beams, which is almost the speed of light (c), and by the number of bunches (N_{bunch}):

$$\tau \sim \frac{P}{c\, N_{bunch}} = 3.5\ \mu\mathrm{s}.$$

Finally [35],

$$L = \frac{N_p N_{\bar{p}}}{\tau S} = 5 \times 10^{30}\ \mathrm{sec}^{-1}\mathrm{cm}^{-2}.$$

One month non-stop running at this luminosity delivers an integrated luminosity of about $15 \times 10^{36}\mathrm{cm}^{-2}$, which is equal to 15 pb^{-1}, the luminosity used in Chapter 2 for estimating the charmonium production rate. Of course, there are always dead time and luminosity losses. For this experiment, accumulating an integrated luminosity of 15 pb^{-1} took about eight months.

As has been mentioned numerous times, the colliding particles are protons and antiprotons. Protons are obtained by stripping off the electrons from a beam of H^- ions and these protons are then accelerated in three stages. First in a synchrotron, called the Booster, up to an energy of 8 GeV. Then in a larger synchrotron; the Main ring, which shares the 6.28 km tunnel with the Tevatron, up to the energy of 120 GeV. The final acceleration stage is in the Tevatron itself up to the energy of 900 GeV.

Antiprotons do not occur naturally and they are much harder to obtain. The advantage of using antiprotons is that they can be accelerated in the same ring as the protons, but in the opposite direction, since they have opposite charge. To obtain the antiproton beam, some protons are extracted from the Main ring and collided into a copper and nickel target. This collision produces proton–antiproton pairs. The antiprotons are then separated. For every million of the initial protons, 20 antiprotons are produced and collected magnetically. When enough antiprotons have been accumulated they are injected into the Main ring and accelerated up to 150 GeV. Finally they are sent to the Tevatron, where their energy reaches 900 GeV and they start being steered into collision with the protons.

Along the Tevatron ring there are two colliding points, called BØ and DØ respectively. The geometrical cross section of the beams is made as small as possible at these collision points in order to deliver the highest possible luminosity to the two collider experiments- CDF, located at BØ and DØ , located at DØ .

3.2 The DØ Detector

DØ is a general purpose detector designed to study high mass states and high P_t phenomena produced as a result of high energy $p\bar{p}$ collisions. Particles with infinite or relatively long lifetime, such as electrons, photons and muons, produced in the initial reaction or as a result of subsequent decays of initial products, can be readily detected. Partons – quarks and gluons– materialize as hadron jets and also can be identified. Neutrinos are difficult to detect, but their presence in the event can be deduced if there is transverse energy imbalance. These points dictate the following general design goals of the DØ detector:

- good electron, photon and muon identification and momentum/energy determination;
- identification and measurement of the kinematic parameters of parton jets (energy and direction angles);
- missing E_t determination.

In order to achieve these goals DØ was designed with the following features:

- stable, hermetic, thick and finely segmented calorimetry based on liquid argon;

- muon system consisting of drift tubes and thick magnetized iron to provide momentum measurement;
- compact central tracking part without magnetic field.

The general view of the DØ detector is shown in Figure 3.2.

In the following we discuss the design and performance of the main parts of the detector.

3.2.1 The Central Detector

The Central Detector consists of the Vertex Drift Chamber (VTX), the Transition Radiation Detector (TRD), the Central Drift Chamber (CDC) and two symmetric Forward Drift Chambers (FDC) (Figure 3.3).

The Central Detector covers the geometrical region up to r = 78 cm and z = $\pm$135cm . As there is no central magnetic field the main task of the Central Detector becomes the discrimination of multiple tracks.

Vertex Drift Chamber

The Vertex Drift Chamber is located immediately outside the beryllium beam tube. Its inner radius is 3.7 cm, the outer radius is 16.2 cm. The VTX consists of 3 layers of cells: 16 cells in the first layer and 32 in each of the second and third. Figure 3.4 shows the cell structure of the VTX. Wires are along the z-direction. The electric field is created by applying positive voltage on the sense wires and negative on the field wires. When a high energy particle passes through a drift cell, it ionizes the gas mixture along its track. In the presence of the electric field the ionization

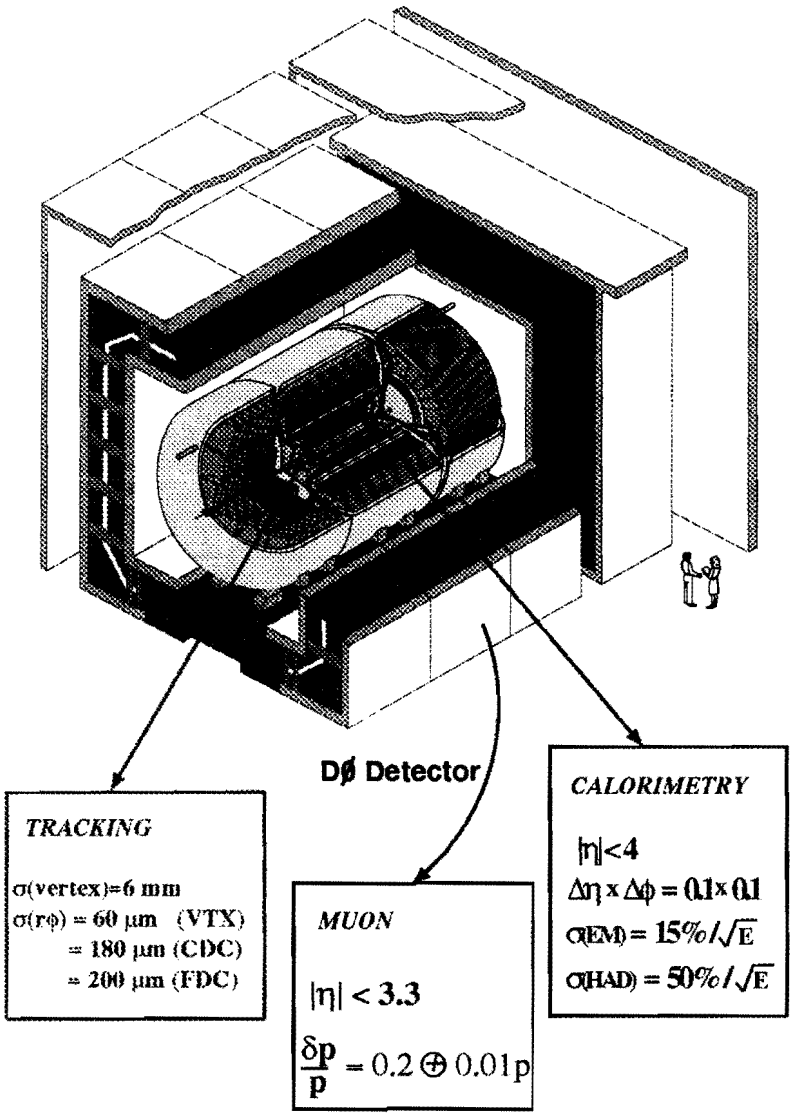

Figure 3.2: General view of the DØ detector

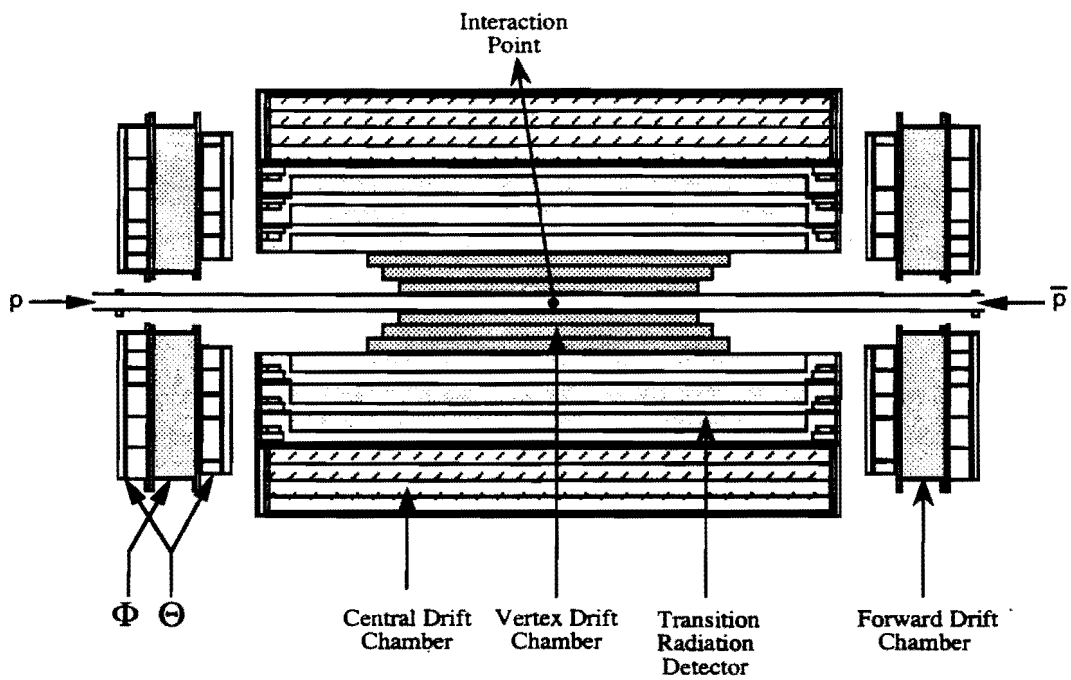

Figure 3.3: A cross section of the DØ tracking system

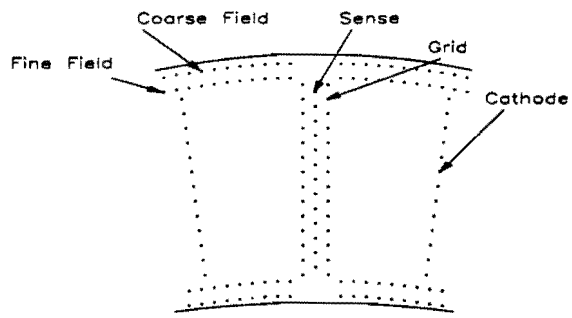

Figure 3.4: The cell structure of the DØ vertex chamber

starts drifting to the nearest sense wire. We can measure the time of arrival at the sense wire and assuming that it started drifting at the moment of $p\bar{p}$ collision we know the drift time. Knowing the drift velocity, we are able to find the distance from the particle track to the wire. The smaller the drift velocity, the better the spacial resolution. We don't know whether the ionization has drifted from the left or from the right of the wire. To resolve this ambiguity, adjacent wires are shifted by $\pm$ 100 μm. Then, out of the two sets of track points in the cell the real set will form a segment with lesser χ^2. Thus, the rϕ projection of the track will be found. To determine the z-coordinate, the signal amplitudes at both ends of the wire are measured and the z-coordinate is determined from their difference.

In the VTX the drift velocity is 7.3 μm/ns. This corresponds to a spacial resolution in the transverse plane of 60 μm. The z-resolution is 1 cm. Two close hits can be resolved with > 90% efficiency if they are separated by > 0.63 mm.

Transition Radiation Detector

The Transition Radiation Detector is used to provide independent electron identification in addition to the information provided by the calorimeter. It occupies the region $16.5 < r < 49.0$cm and $-92 < z < 92$cm. A highly relativistic particle, with Lorentz factor $\gamma = E/m > 10^3$ produces transition radiation X-rays when traversing boundaries between media with different dielectric constants. The spectrum of X-rays depends on γ and this helps to distinguish electrons from pions, since for a given momentum the electron has γ almost 300 times that of the pion.

The TRD consists of three separate units, each containing a radiator and an X-ray detection chamber. The radiator of each unit consists of 393 polypropylene foils in a volume filled with nitrogen gas. The typical X-ray energy is 8 KeV. Time-expansion proportional drift chambers are used to detect the X-rays. The principle of the proportional drift chamber is similar to that of the drift chamber described above. Both the magnitude and the time of arrival of the ionization produced by the X-rays are used to distinguish electrons from hadrons. Pion rejection of a factor of approximately 30 is found for a 90% electron efficiency.

Central Drift Chamber

The Central Drift Chamber occupies the space between 49.5 cm and 74.5 cm in radius and $z = \pm$ 92 cm. It consists of 4 layers of 32 azimuthal cells each. There are 7 sense wires in each cell. To resolve the left-right ambiguity adjacent wires have a relative shift of $\pm$ 200 μm. The drift velocity for the Central Drift Chamber is 34 μm/ns. The spacial resolution in rϕ projection is 150-200 μm. Two hits can be resolved with $>$ 90% probability when they are separated by $>$ 2 mm. The z-

coordinate is measured by the difference of time for signals arriving at each end of the wire. For better resolution, delay lines with 32:1 delay to rise time ratio are used. The z-resolution is 2 mm.

Forward Drift Chambers

The Forward Drift Chambers allow the tracking of charged particles down to 5° in θ. These symmetric chambers are located at either end of the concentric barrels of the Vertex Drift Chamber, the Transition Radiation Detector and the Central Drift Chamber. Each of them consists of three separate chambers : the Φ module whose cells have radial structure and measure the ϕ coordinate, and two Θ modules, whose sense wires measure the θ coordinate. The Φ module is sandwiched between two Θ modules. The $r\phi$ resolution of the Forward Drift Chambers is 200 μm, the z-resolution is 4 mm.

3.2.2 Calorimetry

Since DØ has no central magnetic field and momentum can not be measured for any particles except muons, precise energy measurement is extremely important.

In general, there are two basic types of calorimeter. One is the total absorption calorimeter. When the particle traverses the active material, it loses all of its energy and all of this energy is detected and measured by a detector.

The other type is the sampling calorimeter, which samples only a part of energy lost by the particle. A correction factor has to be applied to obtain the total energy determination. This factor is called the sampling fraction. In a sampling calorimeter the active material is usually sandwiched within a dense absorbing material. Thus

the particle can lose all of its energy in a more compact volume.

DØ has a liquid argon sampling calorimeter. The absorber materials used in the DØ calorimeter are uranium, copper and stainless steel. The calorimeter system consists of a Central Calorimeter, which has the form of a barrel, and two End Calorimeters (see Figure 3.5). The boundary between the Central Calorimeter and

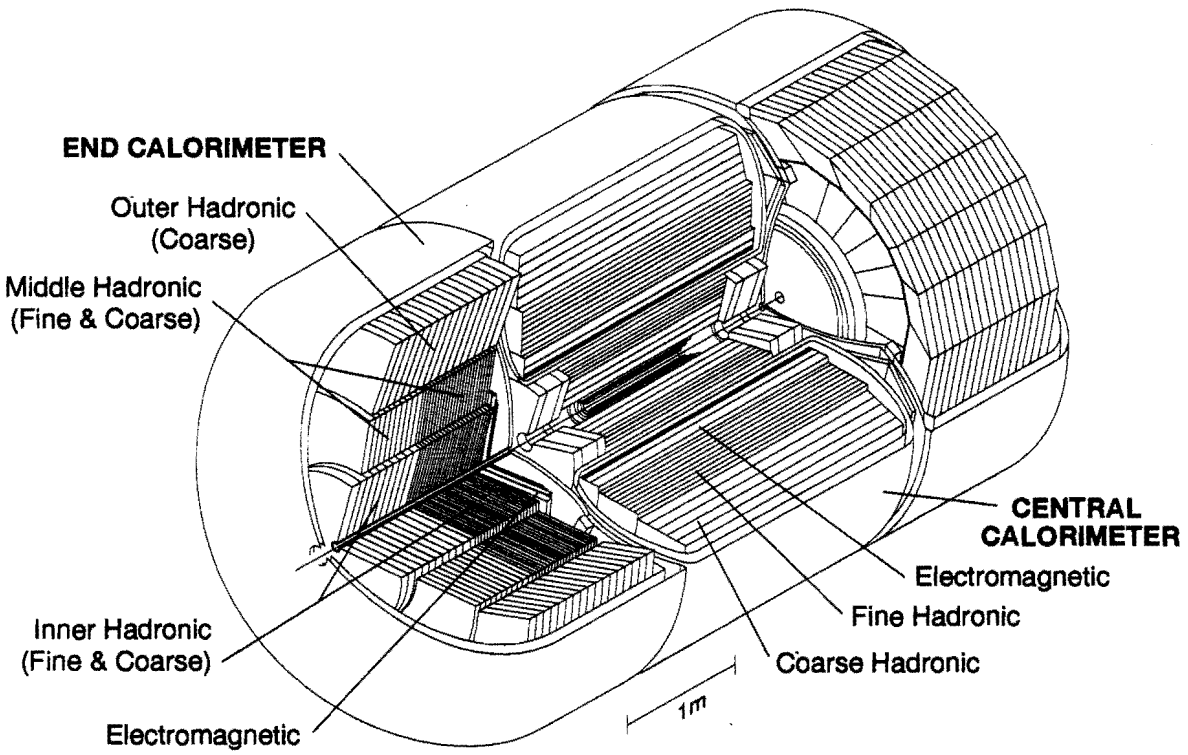

Figure 3.5: A cut away view of the DØ calorimeter system

the End Calorimeters is perpendicular to the beam axis. There are three distinct types of modules in both the Central Calorimeter and the End Calorimeters.

- An Electromagnetic section (EM), with relatively thin uranium plates. Its main purpose is to measure the energy of electromagnetic particles — electrons and

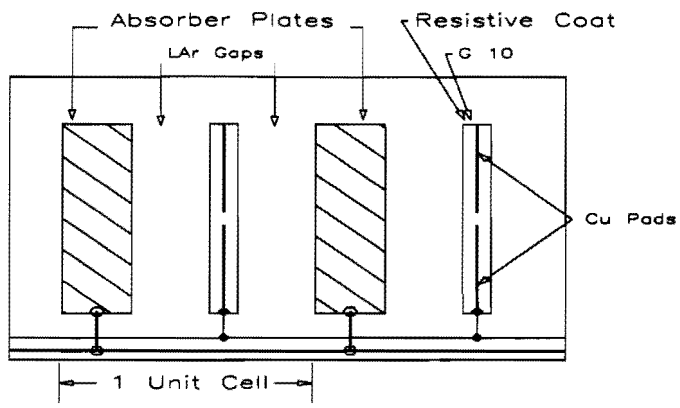

Figure 3.6: A unit cell structure of the DØ calorimeter

photons.

- A Fine Hadronic section with thicker uranium plates. It collects the energy of hadronic particles, such as pions.

- A Course Hadronic section with thick copper or stainless steel plates to minimize the leakage coverage and to ensure the hermeticity of the calorimeter.

A typical calorimeter unit cell is shown in Figure 3.6. The metal absorber plates are grounded and a positive voltage is applied on the signal board. A shower is produced when a particle traverses the absorber. Ionization is collected by the signal board, which is divided into cells. The amount of ionization is proportional to the energy lost by a particle in this cell. The cell size determines the spacial resolution of the calorimeter. The typical size $\Delta R(= (\Delta\phi^2 + \Delta\eta^2)^{1/2})$ of a jet shower is 0.5. To probe the structure of such showers, the cell size was chosen to be approximately 0.1

in η and $2\pi/64 \approx 0.1$ in ϕ.

Central Calorimeter

There are 32 Electromagnetic modules in the inner ring, 16 Fine Hadronic modules in the surrounding ring and 16 Course Hadronic modules in the outer ring.

The Central Calorimeter Electromagnetic modules have four longitudinal signal gangings of approximately 2.0, 2.0, 6.8 and 9.8 radiation lengths (X_0), respectively. The first two layers measure the longitudinal development of the shower near its beginning where electromagnetic particles (electrons and photons) and pions differ statistically. The maximum of the electromagnetic shower energy is deposited in the third layer, and the fourth layer completes the electromagnetic coverage to approximately 20 X_0. Most electromagnetic particles loses all their energy in this part of the calorimeter.

The Central Calorimeter Fine Hadronic modules have three longitudinal gangings of approximately 1.3, 1.0 and 0.9 nuclear absorption lengths (λ_A).

The Central Calorimeter Course Hadronic modules contain one depth segment of 3.2 λ_A. With the Central Calorimeter Electromagnetic part being 0.8 λ_A, the total Central Calorimeter is about 7.2 λ_A thick. This makes the probability extremely low for any particle except a muon to escape the calorimeter.

End Calorimeter

Each of the two symmetric End Calorimeters contain four module types: one Electromagnetic module, one Inner Hadronic module and, outside the Electromagnetic and Inner Hadronic modules, there are 16 Middle and Outer Hadronic modules.

The End Calorimeter Electromagnetic modules have 4 readout sections of 0.3, 2.6, 7.9 and 9.3 X_0, respectively. Each hadronic part has both Fine Hadronic and Course Hadronic sections. At the smallest angle, the End Calorimeter thickness is 10.3 λ_A.

Calorimeter Performance

After various studies and tests the energy resolution was proven to be

$$(\sigma_E/E)^2 = C^2 + S^2/E,$$

where the constants C and S represent the calibration error and sampling fluctuations, respectively. Their values for electromagnetic particles are

C = 0.003 ± 0.002

S = 0.157 ± 0.005 $\sqrt{\text{GeV}}$;

and for pions

C = 0.032 ± 0.004

S = 0.50 ± 0.04 $\sqrt{\text{GeV}}$.

The lower limit on the energy threshold is set by noise and is 0.4 GeV for electromagnetic particles. Cluster position is determined by the cluster center of gravity; cluster position resolution varies from 0.8 to 1.2 mm. A muon track in the calorimeter must be consistent with a minimum ionizing particle, whose energy deposition is typically from 1 to 4 Gev.

3.2.3 The Muon System

The purpose of the Muon System is to identify muons and measure their trajectories and momenta (Figure 3.7).

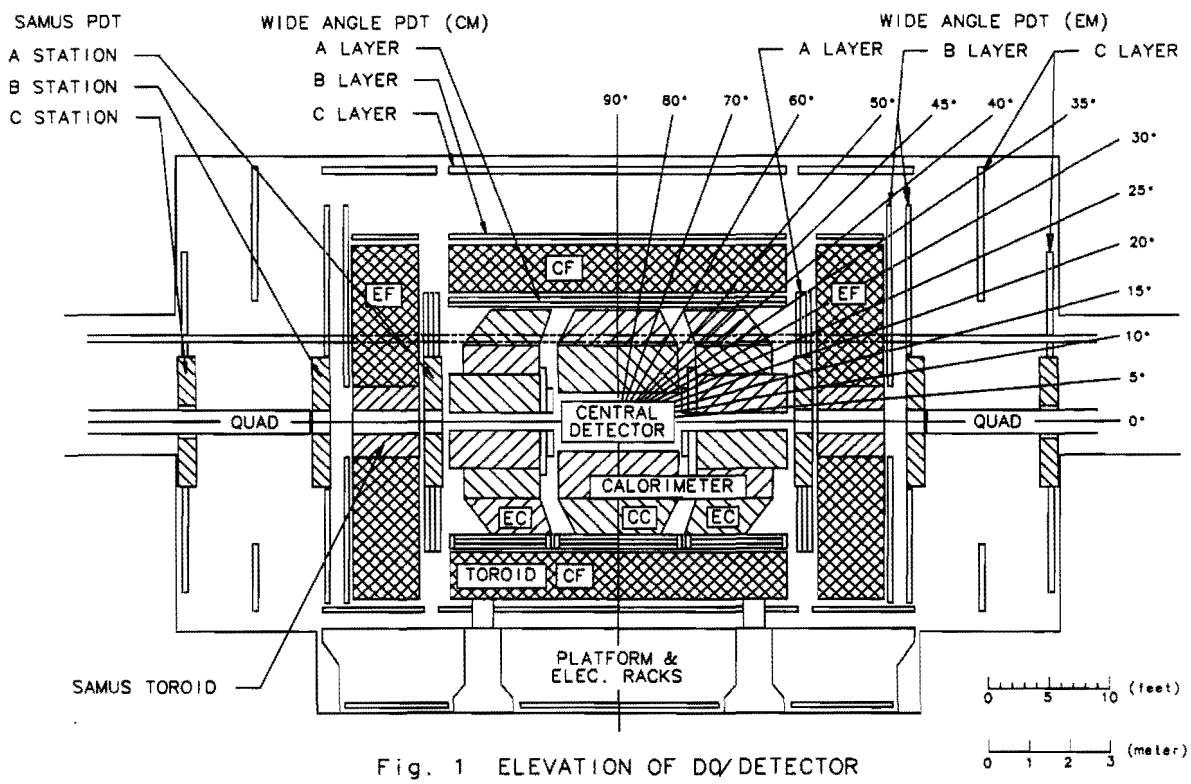

Fig. 1 ELEVATION OF DØ DETECTOR

Figure 3.7: General view of the DØ muon system

The Muon System consists of 5 solid iron toroidal magnets and 3 layers of proportional drift tube chambers – 1 before and 2 after the magnet. This provides a measurement of the initial and final directions of muons and a determination of their momenta by the bend in the magnet. Multiple Coulomb scattering in the iron limits the relative momentum resolution to 20%. The minimum momentum required for a muon to emerge from the iron toroids varies from 3.5 Gev/c in the central part to 5 GeV/c for large η.

The muon magnets have a toroidal magnetic field which bends muons in the r-z plane. The absolute value of the magnetic field is 1.9 T. The muon system consists of three parts : the central region, covering up to $|\eta| = 1.0$, the Wide Angle Muon System (WAMUS) with $1.0 < |\eta| < 2.5$ and the Small Angle Muon System (SAMUS) completing the coverage to $|\eta| = 3.6$.

The central part and the WAMUS consist of three layers called A,B and C, respectively. The A layer is located before the magnet and the B and C layers after. The distance between B and C is about 1 m. A relative offset of the drift tubes is introduced to solve the left-right ambiguity. The drift velocity is about 65 μm/ns. The spacial resolution in the bend view is 0.53 mm. The nonbend coordinate ξ along the wire is measured by a combination of the cathode pad signal and the timing information from the anode wires. A coarse indication of the ξ coordinate is obtained from the difference between the times when the signal arrives at each end of the wire. This Δt measurement has a precision of about 10 to 20 cm.

Finer resolution in ξ is obtained using the information from the cathode pad signals. Figure 3.8 shows the diamond structure of the pads. The amplitudes from the two inner pads (A_{in})are added and read independently of the sum of the amplitudes

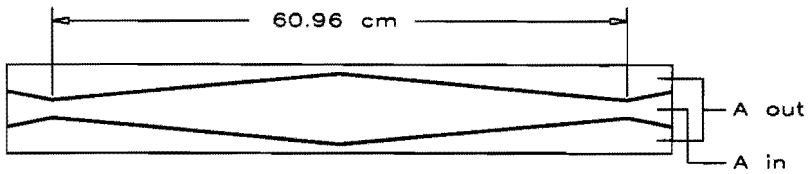

Figure 3.8: The pad structure of the DØ muon system

from the outer pads (A_{out}). The difference between these two amplitudes ($A_{in} - A_{out}$) is at a maximum for a particle passing at the center of the diamond, and smallest on the sides of the diamond, this allows a determination of the ξ coordinate with a resolution of approximately 3mm.

Each of the A, B and C layers of the SAMUS system consist of three doublets of proportional drift tubes. These doublets are oriented in the x, y and u directions, where u is at 45° with respect to x and y. The drift velocity in the SAMUS is 97 μm/ns . The resolution in the bend view is 0.53 mm and 1.6 mm in the non-bend view.

3.2.4 The Trigger System

Not every event that happens as a result of a $p\bar{p}$ collision is interesting from the physics point of view. For example, elastic scattering events are not usually processed and recorded on tape. To select interesting physics events the DØ trigger system is used. The selection is done in three levels.

Level 0 Trigger

The Level 0 scintillator-based trigger indicates the occurrence of an inelastic collision. It detects low angular particles in the interaction region. At a luminosity

$$L = 5 \times 10^{30} \mathrm{cm}^{-2} \mathrm{s}^{-1}$$

there happen on average 0.75 such interactions per beam crossing and the Level 0 trigger rate is about 200 kHz. In addition, the Level 0 trigger provides fast information about the z-coordinate of the primary vertex, which is used in the next step of the selection (the Level 1 trigger) to provide a missing E_t correction.

Luminosity measurement

Information from the Level 0 trigger is used to measure the instantaneous luminosity at DØ[36]. The total number of events registered by the Level 0 trigger is:

$$N_{L0} = acc_{L0}\ L\ \sigma_{tot},$$

where L is the instantaneous luminosity, σ_{tot} is the total cross section of $p\bar{p}$ scattering and acc_{L0} is the acceptance of the Level 0 trigger. The total $p\bar{p}$ scattering cross section at the center of mass energy 1800 GeV was measured in two experiments - E710 [37], [38] and CDF [39], [40], both at the Tevatron in Fermilab. For its Level 0 normalization constant, DØ uses the average value of these two total cross section determinations:

$$\sigma_{tot} = 70\ \ mb.$$

The acceptance of the Level 0 trigger was determined using Monte Carlo simulation and is:

$$acc_{L0} = 69\%.$$

Thus, the instantaneous luminosity is expressed as a function of the Level 0 counts:

$$L = \frac{N_{L0}}{\sigma_{L0}},$$

where $\sigma_{L0} = \sigma_{tot} \quad acc_{L0} = 48.2 \quad mb$. For each run the initial, final and integrated luminosity are measured and stored in the data base. The relative error on the luminosity value is 12%.

Level 1 Trigger

More sophisticated event selection is done in the Level 1 hardware trigger. The Level 1 trigger framework gathers information from the Level 0 trigger, the calorimeter, and the muon system. This information forms the basis for the decision to keep this event for further processing. This decision has to be made before the next beam crossing (every 3.5 μs).

The input to the Level 1 trigger can be, for example, the vertex position from the Level 0 trigger, the transverse electromagnetic, hadronic or missing energy above the threshold from the Level 1 calorimeter trigger processor, the number of coarse muon candidates, etc. Based on this information a logical trigger word is formed. This logical trigger word consists of 32 bits. When all 32 bits are 0, such event is ignored. The event is accepted when at least one bit is 1.

For the particular analysis described here we are discussing a process with 2 muons in the final state, therefore only events that passed the muon triggers are used.

The basic information provided for the Level 1 muon trigger system by the muon chambers, is one bit from each chamber indicating if there was a signal in this chamber. Coarse tracking is done using centroids, which actually are the coordinates of the hit in the bend view but with error bars on the scale of an entire chamber. Thus, we have some rough information about the number of muon tracks in the event.

Level 2 Trigger

The Level 2 trigger is a software trigger and is based on a farm of 48 micro-VAX 4000-M60 computers. The main purpose of the Level 2 trigger is to collect the digitized information from all relevant detector elements for the events that successfully pass the Level 1 trigger. Also, a more sophisticated selection of events is done than is possible in Level 1. Some topological analysis of the event is performed at this level. A total of 128 programmable filter conditions are available for the specific physics interest. If the event passes a filter it is transferred to the host computer for logging. All this allows a reduction in trigger rate from some 200 Hz to about 1 – 2 Hz.

3.3 Data Processing

After an event is accepted by both levels of the triggering system, it is written on tape. At this stage, only raw information about the event is available, for example:

- numbers of the wires that were hit in the Central Drift Chamber, drift times and arrival times at both ends of these wires;
- the amount of energy deposited in each calorimeter cell;
- numbers of the Muon drift tubes hit, drift times and pad signals from them;

- Level 1 trigger word;
- Level 2 trigger word.

This format of the event is referred to as RAW.

The next stage is to identify the hits with the tracks produced by different kinds of particles and determine their kinematic parameters. In other words, the next stage is to reconstruct the event. This is performed using the off-line reconstruction program DØ RECO. All the events that are accepted by both levels of trigger and written on tape are reconstructed. After reconstruction each event is written in two formats. One of them (called STA), contains all the available raw and reconstructed information about the event. Each STA event contains approximately 600 kbytes of data. The other more compact format (called DST) contains only compressed reconstruction information. The size of a DST event is about 20 kbytes. The STA files are typically kept on tape, while the more manageable DST records are largely kept on disk.

After event reconstruction, the first step of event selection is performed. This is called streaming or filtering. Each physics group specifies roughly the characteristics of the events which are interesting for their analysis. For the analysis discussed here, the events that pass the so-called B2M stream were used. The major requirement of this stream is the presence of at least 2 good quality muons in the event. About 6 % of the data satisfy this criterion. Both STA and DST files are streamed.

The history of data processing is kept in a Production Database (PDB). The PDB contains all information about the RAW, the STA and the DST files, the tapes on which the files were written, the version of the reconstruction program that was used for the creation of a particular file and the streaming and filtering information. The

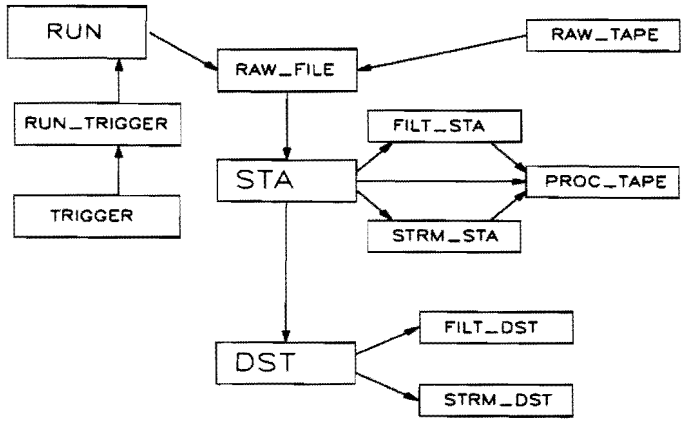

Figure 3.9: The scheme of data processing at DØ

information about runs, triggers and luminosity is also stored in the PDB. What is even more important is that the PDB, being a relational database, keeps information about the relations between the streamed, DST, STA and RAW data files, so that any user can trace back and find out from which RAW data file the streamed file was made. The schematic structure of the Production Database is shown in figure 3.9. Every block on this diagram represents a separate table in the PDB. Arrows show the relations between tables.

These relations between tables represent a very important feature. They allow, for example, calculation of the integrated luminosity for any given data set. The luminosity is calculated per run, based on the number of counts from the Level 0 trigger, and is stored in the PDB. To find the luminosity for any streamed file, one must find, using the relations between tables, from which set of RAW files it was

made. The luminosity for each RAW file (L_{raw}) is related to the run luminosity (L_{run}) as follows:

$$L_{raw} = L_{run} \frac{N_{raw}}{N_{run}},$$

where N_{raw} is the number of events in the RAW file and N_{run} is the total number of events in this run. The streamed file luminosity is summed over all raw files from which the streamed file was produced.

Maintaining the completeness of the PDB and developing the user utilities that allow easy access to the information stored in the database is a very important task.

3.4 Particle Identification

Different particles produce different characteristic signals in the detector. These patterns are identified with a particular type of a particle, although there is always some uncertainty in this identification. The DØ reconstruction program is designed to recognize these characteristic patterns. The reconstruction algorithms are discussed in this section.

3.4.1 Photons and Electrons

As there is a photon in the final state of the physical process discussed in this thesis, photon identification is of particular importance for this analysis.

Electromagnetic particles – electrons and photons – produce similar response in the DØ calorimeter. They create well shaped clusters in the electromagnetic part (EM) of the calorimeter and deposit almost no energy in its hadronic part.

The main clustering algorithm used to define an electromagnetic particle is the *nearest neighbor clustering algorithm* [41]. It forms a cluster by looping through Electromagnetic (EM) towers. The algorithm looks for the highest E_t tower and relates other towers nearest to it into the cluster if their energy is above a certain threshold. These towers are related to the highest E_t tower and then summed into a cluster. The summing continues until there are no towers above the threshold or until the limit in the number of the towers is reached. The total energy of the cluster is defined as the total sum of all the calorimeter cells within the size of the cluster. An acceptable EM cluster is required to have at least 90% of its total energy deposited in the EM section.

The standard DØ threshold for an acceptable electromagnetic cluster is 1.5 GeV.

To distinguish electrons from photons, information from the central tracking part is also used: the particle is identified as an electron if there exists at least one matching track within a road of 0.1 (cell size) in both η and ϕ projections. Otherwise the particle is identified as a photon.

Due to the noise in the calorimeter, both electronics noise and noise induced by the radioactivity of the absorber, there is the possibility of finding fake clusters. The lower the threshold on the cluster energy, the higher is the probability of finding fake clusters. This fact must be taken into account in our analysis, which involves the search for low energy photons.

3.4.2 Muons

Muon identification is extremely important since in the discussed process there are two muons in the final state. Any reconstructed track in the muon system that

satisfies certain quality requirements is considered to be a muon. In addition, the energy deposition in the calorimeter along the muon track must be consistent with a minimum ionizing particle.

The muon reconstruction algorithm proceeds as follows [42] .

Hit Sorting

The location of the hits in a specific muon chamber is determined. These hits are then converted into points in the DØ global coordinate system by correcting for appropriate calibration and alignment constants.

Trackfinding

Trackfinding is the pattern recognition process that identifies a certain set of hits as being all due to the passage of a single muon through the muon system.

Muon trackfinding is done by geographic sectors called quadrants. There are 14 quadrants: 4 in the central part, 4 in each north and south part of the WAMUS, and 1 in each north and south part of the SAMUS. The algorithm searches first for track segments, starting from a wide angle quadrant and proceeding to smaller angles. A road algorithm is used which allows only a single hit per plane with hits required to be on the track line in both magnetic bend and non-bend views. The algorithm first searches for BC segments with at least 4 points. If found, an A layer segment with at least 2 points is searched for. If no BC segment is found, the algorithm searches for an A segment with at least 3 points.

Fitting

Segments from different layers are linked together to form a muon track. For three module tracks, a straight line fit to the BC points is done first. This segment is then extrapolated to the magnet center. The coordinates of the track in the magnet center (referred to as a pseudopoint) are combined with A-layer points in fitting the A-segment.

The non-bend view assumes a straight line fit through the magnet. The momentum of the muon is determined by its bend in the iron toroid magnet.

Quality Flagging

Finally, a track quality flag is set, using the projection of the muon track to the vertex point and the muon quality of fit in separate views as primary factors.

The minimum P_t required for a muon to emerge from the toroid magnet is 3.5 GeV/c and this sets a P_t threshold for muon identification.

When there is a high population of hits, there is always the probability of finding a fake hit combination which occasionally forms a good segment. This effect introduces a so-called combinatorics background.

3.4.3 Jets

As discussed in Chapter 2, some charmonium production mechanisms produce charmonium associated with a jet and some not. Hence, jet identification becomes very important for the separation of different production mechanisms.

Jet identification requires the presence of a hadronic cluster in the calorimeter, which is sought in a similar manner to that of the electromagnetic cluster, described

in 3.4.1 [41]. The jet energy threshold is 8 GeV for DØ.

3.4.4 Neutrinos

Neutrinos are not present in the studied events and neutrino identification, which relies on the missing transverse energy algorithm, is not used in the present analysis.

Chapter 4

Estimates

In a production experiment, the particle of interest can be identified if the invariant mass of its decay products peaks at a certain value. The central value of the mass peak is considered to be the mass of the particle. The width of the mass distribution is determined by the lifetime of the particle as well as the resolution of the apparatus. In this chapter we discuss how well we can identify charmonium states with the DØ detector.

4.1 Kinematics

First, it is useful to find out what are the typical values of the kinematic parameters of the final products of the process. In the case of

$$\chi_c \to J/\psi + \gamma, \qquad J/\psi \to \mu^+ + \mu^-$$

the observable particles are a photon and two muons. It is important to identify typical values of the muon momenta, the angle between the muons, the energy of the photon and the angle between the photon and the two muons.

Typical values of the kinematic parameters are those values for which the cross section of the process is significant. To investigate the dependence of the charmonium production cross section versus the kinematic parameters of the final products, it is necessary to go through the parton formalism, which involves a lot of integration. It is difficult to do analytically, and it is performed instead by Monte Carlo simulation.

The Monte Carlo process involves the following steps:

1. Kinematic parameters of each initial parton are determined according to its structure function;

2. According to the derived differential cross section, the parameters of charmonium and any other product of the $p\bar{p}$ scattering are evaluated;

3. Any parton produced in the reaction is fragmented into hadrons. Muons, electrons and photons are left as such;

4. The charmonium decays into its final products with probabilities defined by branching ratios measured in earlier experiments.

For this analysis we used ISAJET V6.36 [43] as the primary Monte Carlo event generator.

The output of the primary event generator is the set of exact kinematic parameters of the products; in real life, of course, the products are registered by the detectors with a finite resolution. In order to take this into account the event must be processed through software which simulates the detector response. This involves the following steps.

1. The final products are transported through the simulated detector, undergoing all possible interactions with its matter – decays, multiple scattering, nuclear

interaction, delta ray production, ionization, interaction with the magnetic field, and so on.

2. The response of the detector elements to each of the particles is simulated.

3. The response is digitized, according to the realistic electronics resolution.

4. The digitized simulated information is recorded in the same format as the real raw data, so that the same reconstruction program can be used to reconstruct both real and simulated events.

For this analysis DØ GEANT [44] was used as simulator of the detector response. In addition, special packages that introduce the realistic calorimeter noise (NOISY) [45] and the realistic muon chamber resolution and efficiencies (MUSMEAR) [46] were used. These packages take into account the experimentally measured parameters of the DØ calorimeter and the DØ muon system.

In the following paragraphs we discuss the kinematic parameters of the final products, obtained from the ISAJET simulation. The full detector simulation is used later for the acceptance determination.

Figure 4.1 shows the transverse momentum distribution of either muon in the final state. The momentum of the muon must be at least 3.5 GeV/c for it to emerge from the magnet of the muon system. This imposes a threshold on the muon momentum in this distribution. From Figure 4.1 we see that muons from the J/ψ decay typically have momentum of about 5 GeV/c.

The distribution in the angle between the two muons is shown in Figure 4.2. At Tevatron energies, the J/ψ decays into two muons with an average angle of about 35° between them.

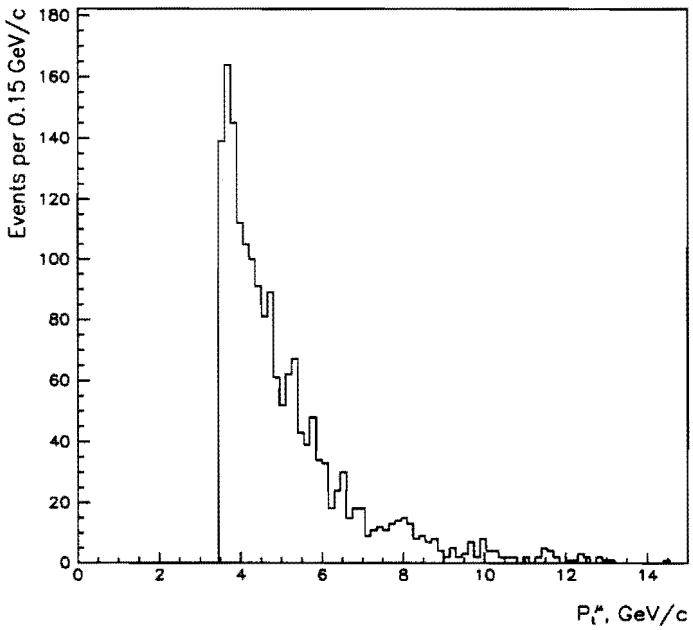

Figure 4.1: The transverse momentum distribution of the muons from J/ψ decay

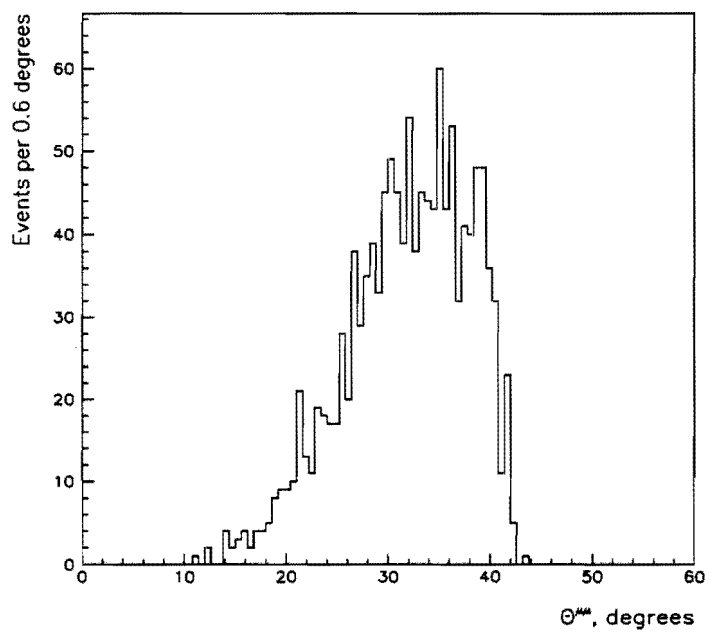

Figure 4.2: Distribution in the angle between the two muons from J/ψ decay

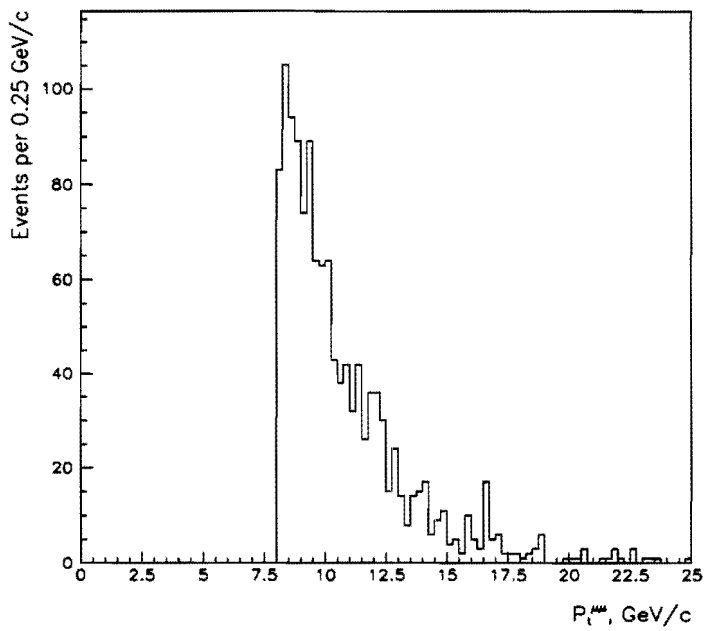

Figure 4.3: The J/ψ transverse momentum distribution

Using the measured momenta and angles of the two muons it is possible to reconstruct the momentum and angle of the two muon system itself. Figure 4.3 depicts the transverse momentum distribution of the dimuon system.

In the χ_c rest frame the energy of the photon is the difference between the χ_c and J/ψ masses. This is 0.4 GeV. In the laboratory frame it is boosted along the χ_c direction. Figure 4.4 shows the photon energy distribution; 58% of all photons have energy above 0.8 GeV. Hence, if the threshold on the energy of the reconstructed photon is 0.8 GeV, about 58% of the photons from χ_c decay can be detected. For our estimations we can consider the energy of the photon to be around 1 GeV.

The distribution in angle between J/ψ and the photon is shown in Figure 4.5. The photon is close to the J/ψ. The angle is always less than 40°.

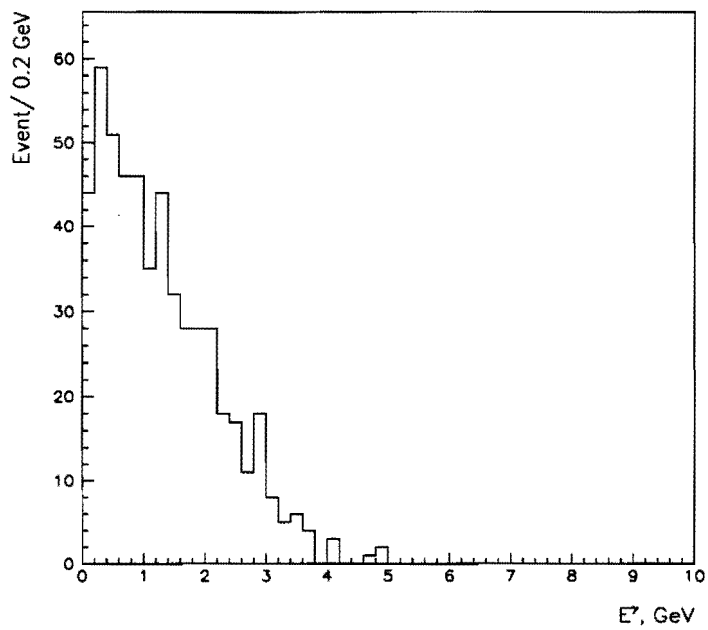

Figure 4.4: The energy distribution of the photon from χ_c decay

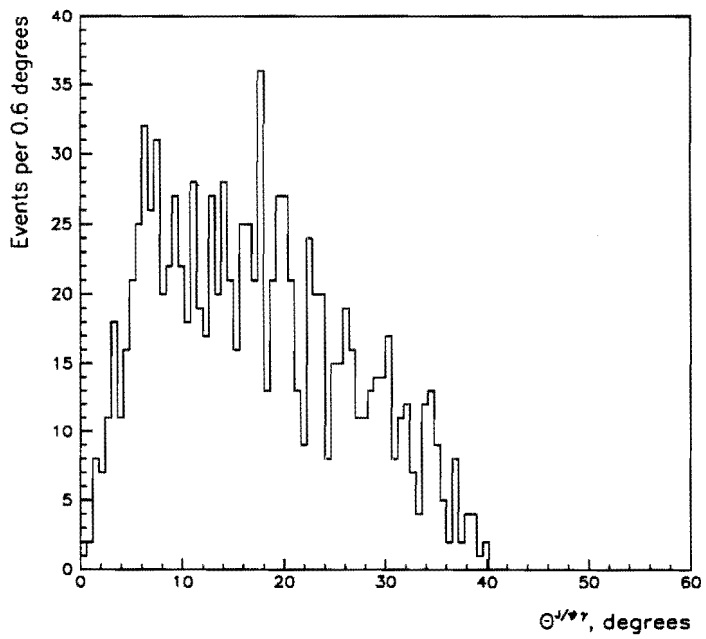

Figure 4.5: Distribution in the angle between J/ψ and the photon from χ_c decay.

In summary, the χ_c decay produces a photon whose energy is around 1 GeV, and two muons with momenta near 5 GeV/c and with an angle of about 30° between them. The photon direction is close to the dimuon system direction.

4.2 Kinematic Resolution Estimates

The two muons in the final state of the discussed process must form the invariant mass of J/ψ and then together with the photon, form the invariant mass of one of the three χ_c states.

The invariant mass squared of two muons can be expressed in terms of their kinematic parameters as:

$$M_{\mu\mu}^2 = (E_{\mu 1} + E_{\mu 2})^2 - (\vec{P_{\mu 1}} + \vec{P_{\mu 2}})^2 = 2M_\mu^2 + 2P_{\mu 1}P_{\mu 2}(1 - \cos\theta_{12}),$$

where $E_{\mu i}$ is the energy of the i-th muon, $P_{\mu i}$ is its momentum, M_μ is the muon mass and θ_{12} is the angle between the two muons. The resolution of $M_{\mu\mu}^2$ is determined by the momentum resolution of the muon system, (20% in the case of DØ), and its angular resolution. The coordinate resolution in the nonbend view is about 1.6 mm, which on a base of 3 m corresponds to an angular resolution of about 0.05%. Therefore, it is clear that the mass resolution is dominated by the precision of the muon momentum measurement:

$$\Delta M_{\mu\mu}^2 / M_{\mu\mu}^2 = \sqrt{2}\Delta P_\mu / P_\mu$$

or

$$\Delta M_{\mu\mu} / M_{\mu\mu} = \frac{\Delta P_\mu}{\sqrt{2}P_\mu} = 13\%$$

For $M_{\mu\mu} = M_{J/\psi} = 3.1$ GeV/c^2 the mass resolution we can expect is ≈ 0.4 GeV/c^2.

To obtain the invariant mass of χ_c we must combine the two muons and the photon. Since the difference of the masses of χ_c and J/ψ is much smaller than the mass of J/ψ, we can neglect the kinetic energy of J/ψ in the rest frame of χ_c and assume that the photon from χ_c would have energy equal to the mass difference of χ_c and J/ψ. This is approximately 0.4 GeV. It is convenient to look not at the $M_{\mu\mu\gamma}$ spectrum but at the mass difference $M_{\mu\mu\gamma} - M_{\mu\mu}$ spectrum, where to first order the dimuon mass resolution does not contribute and everything is determined by the photon energy resolution:

$$M_{\mu\mu\gamma} - M_{\mu\mu} = E_{cm\gamma} = E_\gamma/\gamma,$$

where $E_{cm\gamma}$ is the photon energy in the rest frame of χ_c and γ is the Lorentz factor. The relative resolution of the mass difference is equal to the relative photon energy resolution (this is $15\%/\sqrt{E}$ in DØ). The photon energy is typically 1 GeV in the laboratory frame, so we can expect the resolution for the mass difference to be $\sim$ 15%. This is approximately 0.064 GeV and clearly not adequate enough to separately resolve the individual χ_c states, the mass difference for which is about 0.045 GeV. Therefore, in the following we discuss only inclusive χ_c production.

To avoid the contribution from the muon momentum resolution to the χ_c mass resolution so-called kinematic fit can be used. The idea of this method is that the value of the muon momentum is allowed to vary within its errors, so that the invariant mass of the dimuon system is constrained to be that of the J/ψ.

4.3 The Goals of the Experiment

In this experiment we intend to use data collected with the DØ detector to:

- fully reconstruct the J/ψ and inclusive χ_c states,
- measure the χ_c production cross section at a center of mass energy 1800 GeV,
- separate different charmonium production mechanisms.

All the well-defined characteristics of the detector plus our estimates of the event yields and mass resolutions indicate the feasibility of this study.

Chapter 5

Event Selection

In the following chapter we discuss data collected with the DØ detector in the August 92 to May 93 period of time. The integrated luminosity for this data set is about 13 pb^{-1}. Approximately 13 million events were recorded on tape in this run. The maximum instantaneous luminosity achieved in this run was $5 \times 10^{30} cm^{-2} sec^{-1}$.

In the discussed process

$$p + \bar{p} \rightarrow \chi_c + X, \qquad \chi_c \rightarrow J/\psi + \gamma, \qquad J/\psi \rightarrow \mu^+ + \mu^-$$

there are two muons and one photon in the final state. To reconstruct this process implies finding the events where there are two muons, which form the invariant mass of J/ψ, and a photon, which together with the muon system forms the invariant mass of χ_c. The data selection is done in three steps.

- Events with two good quality muons are found,
- certain restrictions (so called "cuts") are applied to the dimuon sample to isolate the J/ψ signal from the background processes,
- photons are reconstructed for the accepted dimuon events.

In this chapter we discuss this event selection process.

5.1 Single Muon Selection

5.1.1 Level 1 trigger.

The Level 1 hardware muon trigger requires 2 hits in either 2 or 3 layers of the muon system, depending on the geometric region, in a coarse road of 60 cm width. The efficiency of the Level 1 muon trigger for high P_t muons is about 60%.

5.1.2 Level 2 trigger.

The Level 2 software muon trigger requires a good quality muon track with reconstructed transverse momentum $P_{t\mu} > 3.5$ GeV/c. A good quality track implies that this track has been fitted in both bend and nonbend views and has a good vertex projection.

5.1.3 Offline selection.

In the offline analysis, two good quality muons are required in the fiducial volume $\mid \eta \mid < 0.8$ and $P_{t\mu} > 3.5$ GeV/c. To ensure the quality of muons the following other requirements are applied: since a true muon should deposit some energy in the calorimeter, the energy deposition along the muon track in the calorimeter is required to be consistent with the deposition of a minimum ionizing particle

$$E_\mu > 1\,\mathrm{GeV}.$$

To reduce the combinatorics background, which was defined earlier in the muon identification section, we avoid events where there is too high a hit population in one cell. We therefore demand the ratio of the total number of hits in the event to the total number of hit modules to be less than 3.5. To avoid so-called blast events, which happen due to electronics failure, the total number of hits in the event is required to be less 130.

5.1.4 Dimuon selection.

Only central dimuons ($|\eta_{\mu\mu}| < 0.6$) contribute to the final event sample. The additional requirement for dimuons is $P_{t\mu\mu} > 8$ GeV/c. To reject a potentially huge contribution from cosmic ray muons that punch through the detector and leave a track looking like two back-to-back muon tracks, the following cuts on the angles between muons are applied:

$$|\phi_1 - \phi_2| < 160^0 \quad or \quad |(\theta_1 + \theta_2) - 180^0| > 30^0,$$

where ϕ_i is the azimuthal angle of the i-th muon and θ_i is its angle with respect to the beam axis. This cut suppresses the cosmic ray contamination to about 0.2%.

As noted earlier, the invariant mass of the system of two muons can be expressed as:

$$M_{\mu\mu} = (2M_\mu^2 + 2P_{\mu 1}P_{\mu 2}(1 - cos\theta_{12}))^{1/2},$$

where $M_\mu (= 0.105\ GeV/c^2)$ is the mass of the muon, $P_{\mu i}$ is the momentum of the i-th muon, and θ_{12} is the angle between the two muons. It is useful to notice, that for given muon momenta, the wider the angle between them, the larger is the invariant mass.

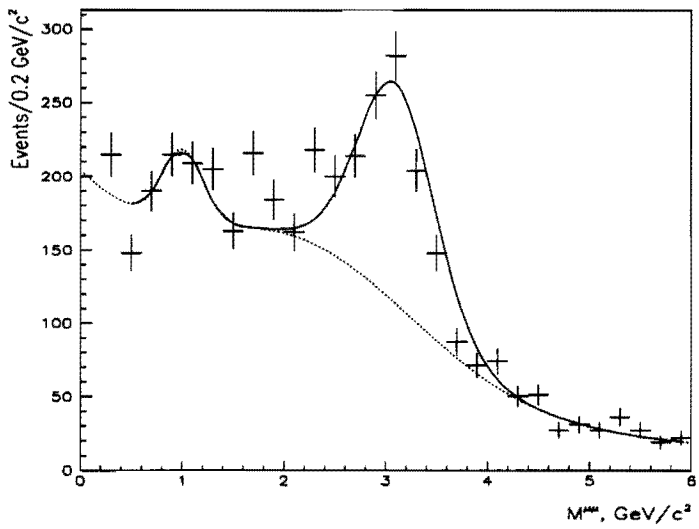

Figure 5.1: The experimental spectrum of the invariant mass of two muons the curves show the fit to the background plus the J/ψ signal shapes (solid line) and the background shape (dashed line).

The final experimental spectrum of the invariant mass of two muons is shown in Figure 5.1. There is a clear J/ψ peak seen in the mass region between 2 to 4 GeV/c^2. The mass resolution is consistent with the one expected from the muon P_t resolution. In the next section we shall discuss different contributions to this dimuon spectrum.

5.2 Contributions to the dimuon spectrum

The possible processes producing two muons and the associated dimuon invariant mass spectra, obtained with the full DØ simulation, are discussed in this section.

5.2.1 b-quark decay.

Two muons can be produced in the decay of two b-quarks produced in the $p\bar{p}$ collision. A b-quark decays into a c-quark plus a W-boson, which in turn decays into a lepton and a neutrino:

$$p\bar{p} \rightarrow b + \bar{b},$$

$$b \rightarrow c + W^-,\ \bar{b} \rightarrow \bar{c} + W^+,$$

$$W^\pm \rightarrow l^\pm + \nu_l.$$

This type of quark decay is called a semileptonic decay. The c-quark may also decay semileptonically:

$$c \rightarrow s + W^+,\ \bar{c} \rightarrow \bar{s} + W^-$$

$$W^\pm \rightarrow l^\pm + \nu_l.$$

With the probability of approximately one third the lepton from W-decay happens to be a muon. If the lepton is a tau, it also may produce a muon in its decay. There are several possibilities to produce two muons. First, when both b-quarks decay into a muon, this is called *parallel* b-decay (see Figure 5.2). Second, when one of the b-quarks decays into a muon, and then the c-quark from the decay of any of the b-quarks also decays semileptonically into a muon (see Figure 5.3). When the c-quark comes from the same b-quark that decayed into the muon, that type of decay is called *sequential* b-decay. The final possibility is, when both c-quarks decay into muons. This can also be referred to as parallel decay. The two b-quarks are produced almost back-to-back with respect to each other and so the muons from the parallel b-decay tend to have a large angle between them. Hence, these muons tend to populate the high invariant mass region. Similarly, when one muon comes from one b-quark and the

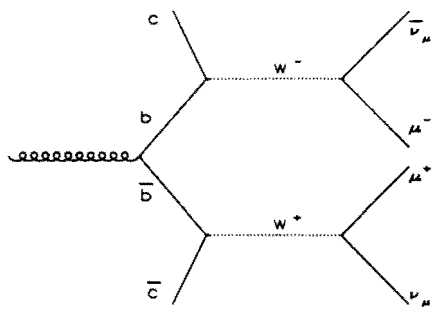

Figure 5.2: Feynman diagram of the parallel b-quark decay

other muon from the c-quark which came from the decay of the other b-quark; though in this case the muons have the same charge and presumably do not contribute to our event sample. The muons, that both come from the c-quark decays have opposite charges and their invariant mass is high.

On the other hand the two muons that both come from the same b-quark form small angles with each other. Thus, they populate the low invariant mass region. The combined invariant mass spectrum of all muon pairs from b-decay is shown in Figure 5.4.

5.2.2 Drell-Yan

In a $p\bar{p}$ collision, a pair of muons can be produced, when quarks and antiquarks annihilate into a virtual photon or a Z-boson, which then decays into a lepton pair. The reaction

$$p + \bar{p} \rightarrow \mu^+ + \mu^- + X$$

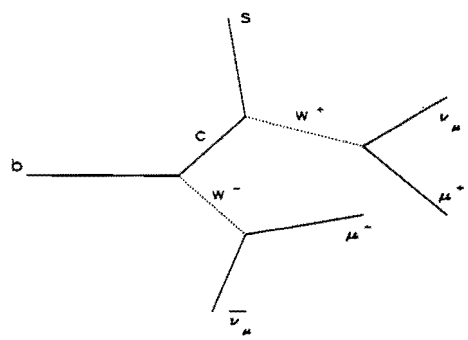

Figure 5.3: Feynman diagram of the sequential b-quark decay

is called the Drell-Yan process [1]. It is illustrated in Figure 5.5. When two muons are the only particles produced in this process, they are back-to-back with respect to each other, and hence, have high invariant mass. However, there is a high probability for an initial quark to emit a high energy gluon and in this case, the muons can form smaller angles and can have low invariant mass. The invariant mass spectrum of two muons from the Drell-Yan process is shown in Figure 5.6.

5.2.3 Muons from Hadronic Jets

Muons can be produced in hadronic jets, either from the leptonic decays of $\pi^{\pm}$ or $K^{\pm}$, or from $\mu^+ \mu^- X$ decays of the low mass resonances: ω, ϕ, ρ, η. The branching ratio of the leptonic decays for $\pi^{\pm}$ and $K^{\pm}$ are high, but their life time is long. The branching ratio for the $\mu^+ \mu^- X$ decays of the low mass resonances are usually low, i.e. 10^{-4}, but their life time is short. Pions, kaons and low mass resonances are produced in large amounts in the hadronic jets, and thus constitute a large source

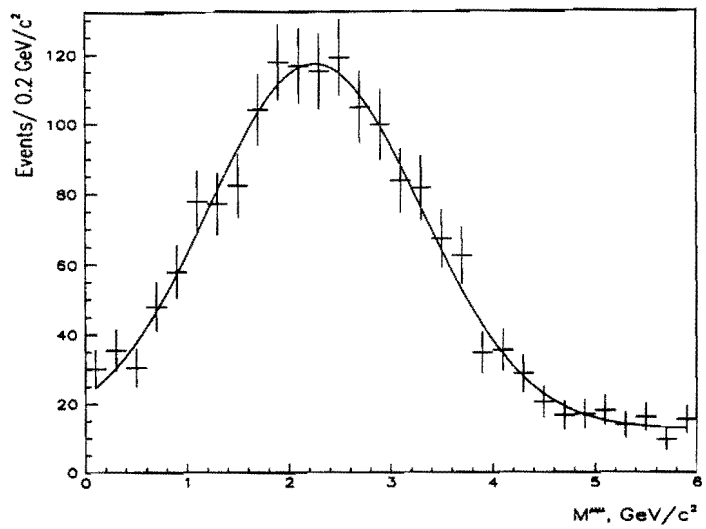

Figure 5.4: The combined invariant mass spectrum of muons from b-quark decay, obtained from a full Monte-Carlo simulation

of the dimuon events. When muons come from the same jet their invariant mass is small; muons from different jets populate higher invariant mass region. The invariant mass spectrum of two muons from hadronic jets is shown in Figure 5.7.

5.2.4 Cosmics

A cosmic ray muon that passes through the entire detector produces a track that may be interpreted as two back-to-back muon tracks. The reconstruction program that uses the vertex position as a point in the track fit introduces spurious small angle between these two tracks. That is why 0.2% of the cosmic ray muons survive after "cosmic" cuts and should be taken into account in our discussion of the contributions to the total dimuon invariant mass spectrum.

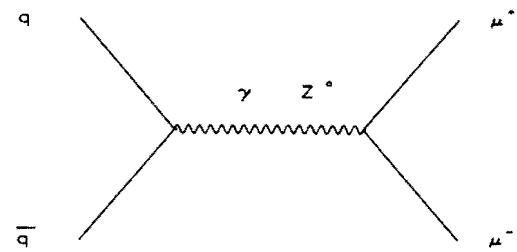

Figure 5.5: Feynman diagram of the Drell-Yan process

Cosmic ray muon tracks produce large dimuon invariant mass. Real cosmic events were studied using special cosmic ray runs with the accelerator turned off and only cosmic ray muons being registered by the detector. The invariant mass spectrum of these cosmic ray muons after the "cosmic" cut has been applied, is shown in Figure 5.8.

5.2.5 J/ψ

As discussed in chapter 2 there are three possible mechanisms that can produce a J/ψ state in a hadronic collision. These are: direct charmonium production from hard scattering, gluon and c-quark fragmentation and b-quark decay.

All the three mechanisms of J/ψ production were simulated and shown to yield essentially the same dimuon invariant mass spectrum. This is because the spectrum is determined mainly by the muon detector resolution. The dimuon invariant mass spectrum with the simulated J/ψ signal is shown in Figure 5.9. The width of this

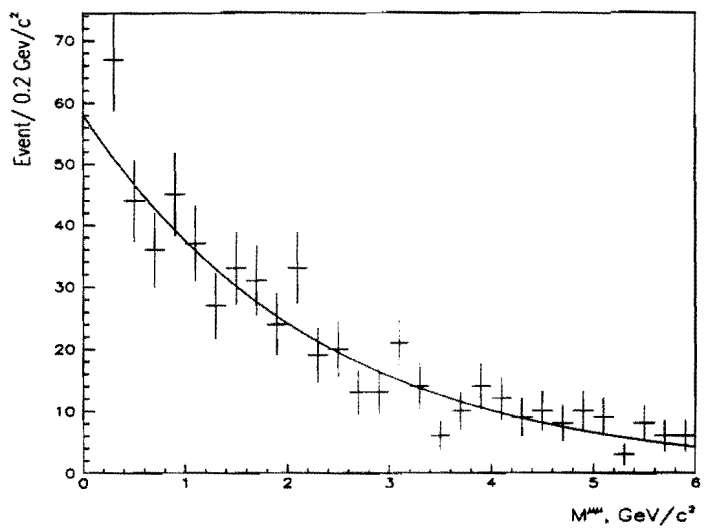

Figure 5.6: The invariant mass spectrum of two muons from the Drell-Yan process, obtained from a full Monte-Carlo simulation

distribution is determined by the momentum resolution of the muon system, and is about 0.4 GeV/c, which is in good agreement with our simple estimates done in Chapter 4.

5.3 Fitting the Dimuon Spectrum

All contributions to the dimuon invariant mass spectrum were fitted with smooth curves and then the experimentally obtained dimuon spectrum was fitted to the sum of the these curves (see Figure 5.1). Thus the number of the J/ψ in the final event sample was obtained. In this manner we obtain:

$$N_{J/\psi} = 722 \pm 52(\text{stat}) \pm 72(\text{sys}) \text{ events},$$

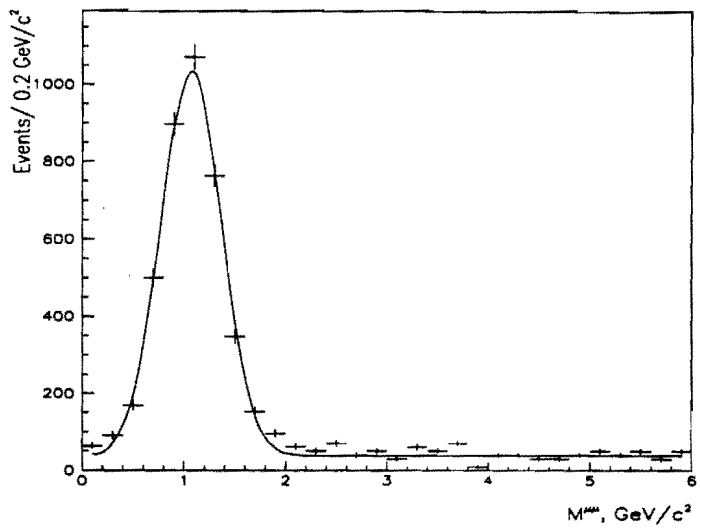

Figure 5.7: The invariant mass spectrum of two muons from the hadronic jets, obtained from a full Monte-Carlo simulation

where the statistical error comes from the statistical error on the parameters of the fit of the J/ψ signal and the systematic error is determined by the background fit errors. Here and latter we use the least square fit method. As can be seen from Figure 5.1, the J/ψ signal is contained between 2 and 4 GeV/c^2. This is the region in the dimuon invariant mass distribution that is considered for further analysis. The main contributions to this part of the dimuon mass spectrum are from the J/ψ signal itself, from the b-quark sequential decay and from Drell-Yan. The latter processes constitute the major background.

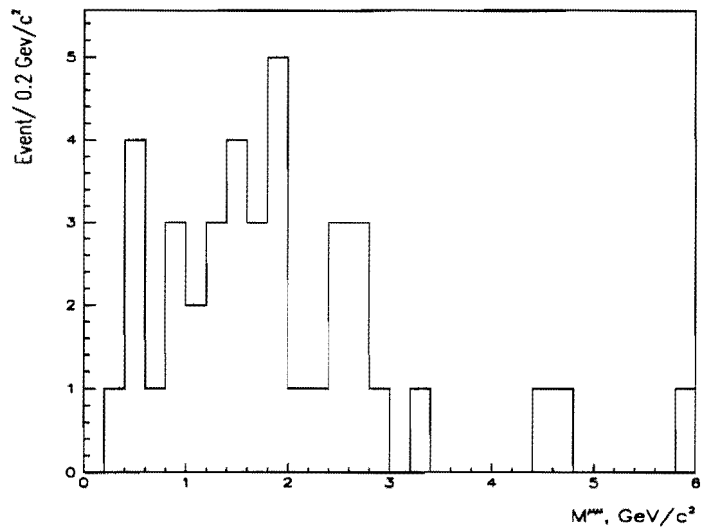

Figure 5.8: The invariant mass spectrum of the cosmic ray muons, obtained from cosmic ray runs

5.4 MU_2_HIGH Dimuons

The full statistics from the run 1a was used only to determine the fraction of the J/ψ events coming from χ_c decay. However, this was the first collider run of the DØ detector and the trigger configuration changed a lot during that period of time. Also, during the December 1993 shutdown the muon system was adjusted, which caused an increase in its efficiency. The Monte Carlo was tuned to account for that efficiency. That is why, to determine the production cross section, only data that were taken after the shutdown (December 1993 - May 1994, corresponding luminosity 6.6 pb^{-1}) and only those events that pass a specific muon trigger - MU_2_HIGH were used. From this data the J/ψ production cross section is obtained. The χ_c production cross section is calculated as a product of the J/ψ cross section and the fraction of the J/ψ

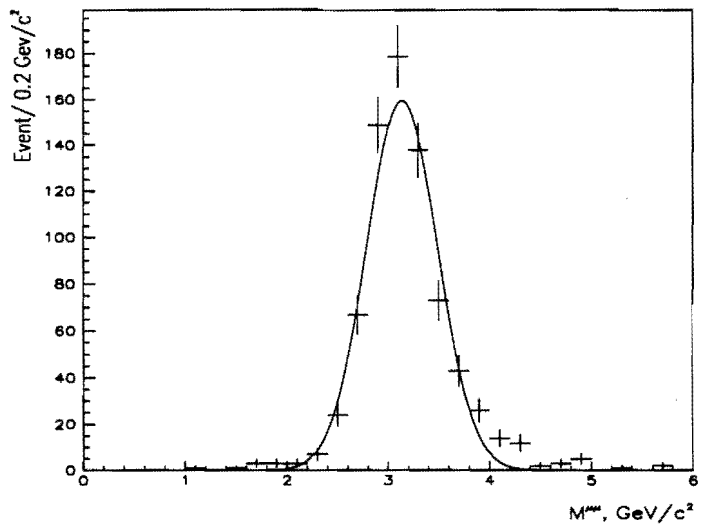

Figure 5.9: The dimuon invariant mass spectrum of the J/ψ signal from a full Monte-Carlo simulation

coming from χ_c decay.

The dimuon invariant mass spectrum for the post shutdown MU_2_HIGH events is shown in Figure 5.10.

The number of the J/ψ events obtained from the fit, similar to discussed above is:

$$N^{J/\psi}_{MU_2_HIGH} = 444 \pm 36(stat) \pm 44(sys).$$

5.4.1 Photon Selection

As mentioned in Chapter 4, the photon from χ_c decay has relatively low energy. The standard DØ threshold on the energy of the electromagnetic cluster is 1.5 GeV and even with 100% efficient reconstruction, with this threshold only 22% of the

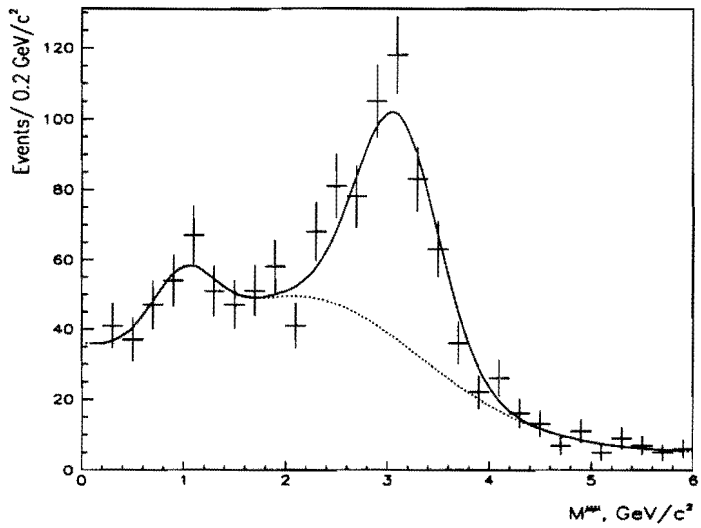

Figure 5.10: The experimental dimuon invariant mass spectrum for post shutdown data, MU_2_HIGH trigger

photons from χ_c decay would be registered. Therefore, the photon energy threshold was lowered down to 0.8 GeV for this analysis, and the entire data sample of dimuons with dimuon invariant mass between 2 and 4 GeV/c^2 was rereconstructed. Offline a photon energy was required to be greater than 1.0 GeV. Approximately 60% of the photons from χ_c decay have energy greater then 1.0 GeV. The reconstruction efficiency of the low energy photons was found to be $50.0 \pm 2.4\%$. Finally, the total efficiency of finding the photon from χ_c decay is $30.0 \pm 1.5\%$.

The mass difference spectrum ($\Delta M = M_{\mu^+\mu^-\gamma} - M_{\mu^+\mu^-}$) for the dimuon events is shown in Figure 5.11. There is a clear χ_c signal at $\Delta M = 0.43$GeV/c^2. The width of the peak is 0.063 GeV/c^2, which is determined by the photon energy resolution. This agrees with our estimations done in Chapter 4.

Lowering the photon energy threshold unfortunately causes many fake electro-

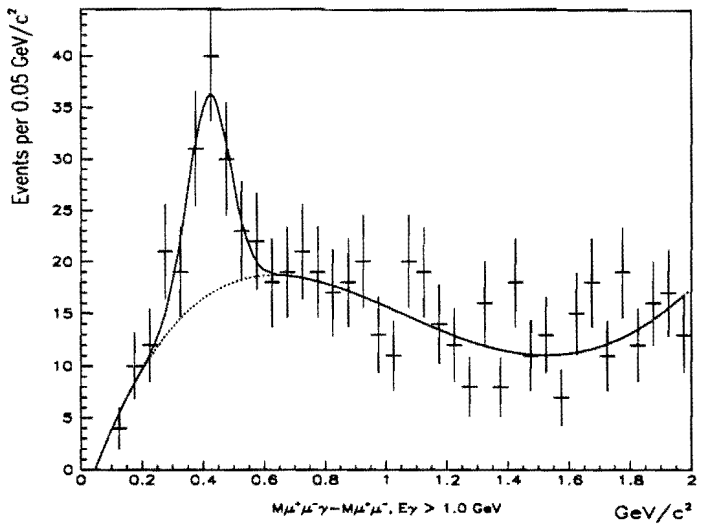

Figure 5.11: The mass difference spectrum ($\Delta M = M_{\mu^+\mu^-\gamma} - M_{\mu^+\mu^-}$) for the selected dimuon events

magnetic clusters to be reconstructed. The contribution from the fake photons to the mass difference distribution was estimated in two different ways:

- a Monte-Carlo simulation of the background processes was performed (using the NOISY package) to reproduce realistic calorimeter noise. The Monte-Carlo events were reconstructed with the same reconstruction algorithm and with the same threshold on the energy of the electromagnetic cluster as the real data. The ΔM distributions for different backgrounds are shown in Figure 5.12, Figure 5.13 and Figure 5.14.

- events with same sign muons were selected , using the same requirements, and rereconstructed with the same algorithm (see Figure 5.15).

In all three cases the ΔM distribution has been fitted by the 4-th power polyno-

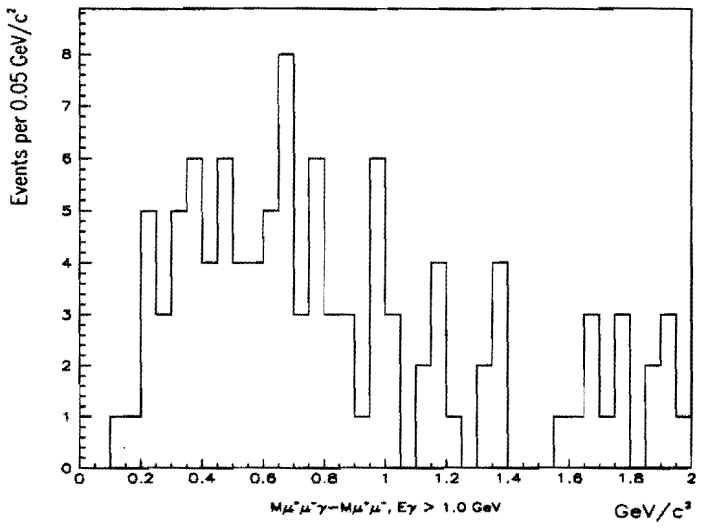

Figure 5.12: The ΔM distribution for J/ψ from b-quark decay

mial. Taking this as the shape of the background, the experimental mass spectrum was fitted to a 4-th power polynomial plus a gaussian signal. The width of the gaussian distribution agrees with that of the simulated χ_c decay (see Figure 5.16).

The number of the χ_c events obtained from the fit is

$$N_{\chi_c} = 66 \pm 15(stat) \pm 5(sys) \ \ events.$$

Systematic error is determined by the background fit errors.

5.5 χ_c Reconstruction for Different P_t regions

As was stated in Chapter 2 the P_t dependance of the χ_c production cross section $(\frac{d\sigma}{dP_t^2})$ is sensitive to the production mechanism, viz. direct charmonium production

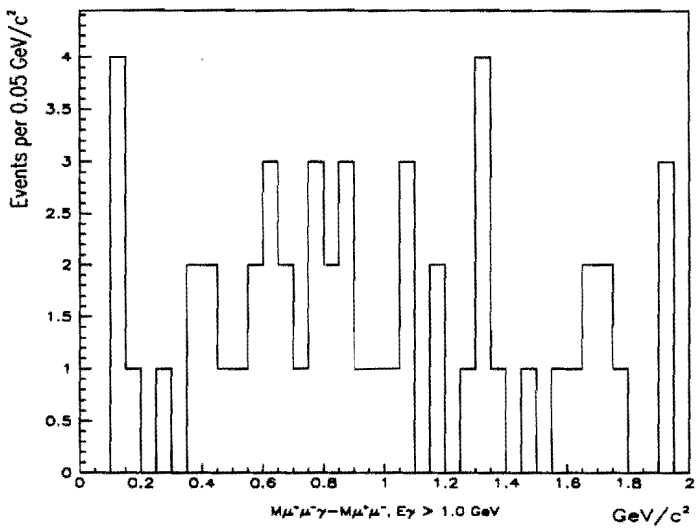

Figure 5.13: The ΔM distribution for dimuons from parallel and sequential b-quark decays

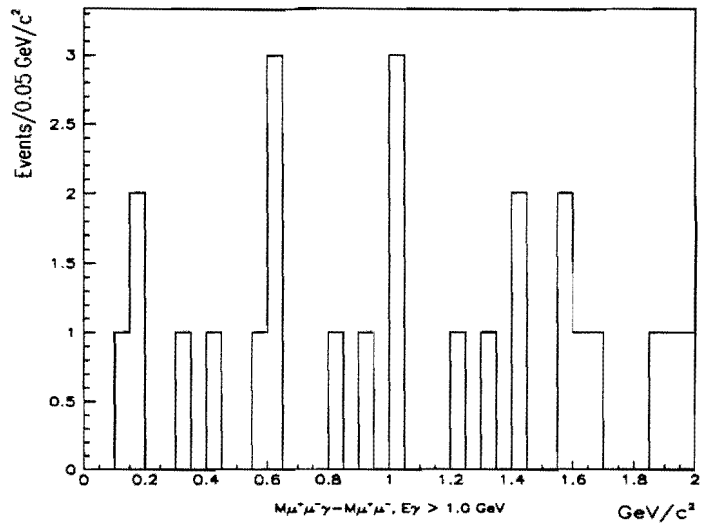

Figure 5.14: The ΔM distribution for the Drell-Yan process

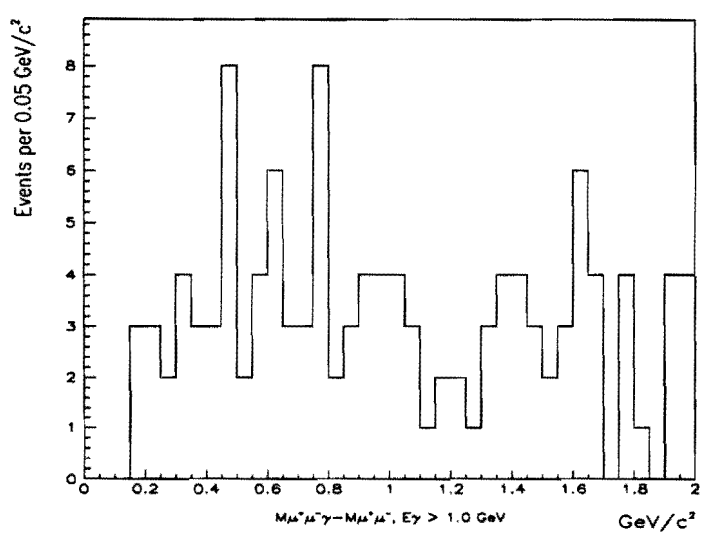

Figure 5.15: The ΔM distribution for same sign muons

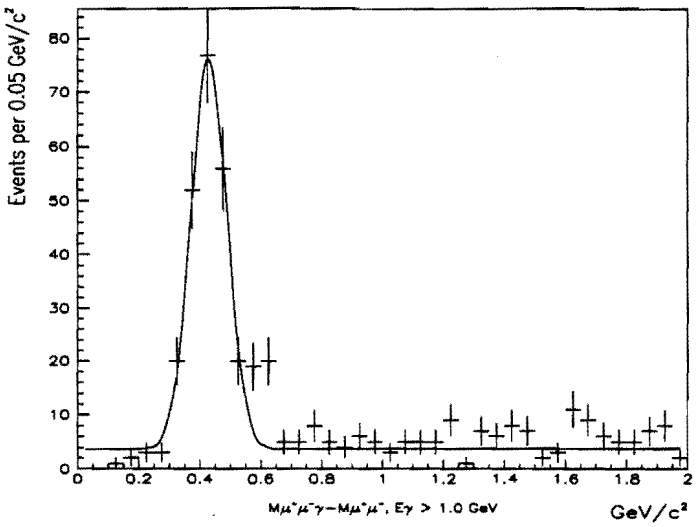

Figure 5.16: The ΔM distribution for J/ψ from χ_c decay

exhibits P_t^{-6} behaviour while gluon fragmentation and b-quark decay are proportional to P_t^{-4}. That is why it is important to study the P_t dependance of the χ_c production cross section.

The same procedure as discussed above was used to reconstruct the χ_c signal for two P_t regions of J/ψ :

$$8 < P_t < 10 \text{ GeV/c and } \mathrm{P_t} > 10 \text{ GeV/c.}$$

The corresponding dimuon mass ($M_{\mu\mu}$) spectra and $\Delta M(= M_{\mu\mu\gamma} - M_{\mu\mu})$ spectra are shown in Figure 5.17. The numbers of J/ψ events obtained from the fits of the $M_{\mu\mu}$ spectra are:

$$N_{J/\psi}(8 < P_t < 10) = 203 \pm 29(\text{stat}) \pm 20(\text{sys}) \text{ events,}$$

$$N_{J/\psi}(P_t > 10) = 498 \pm 38(\text{stat}) \pm 50(\text{sys}) \text{ events.}$$

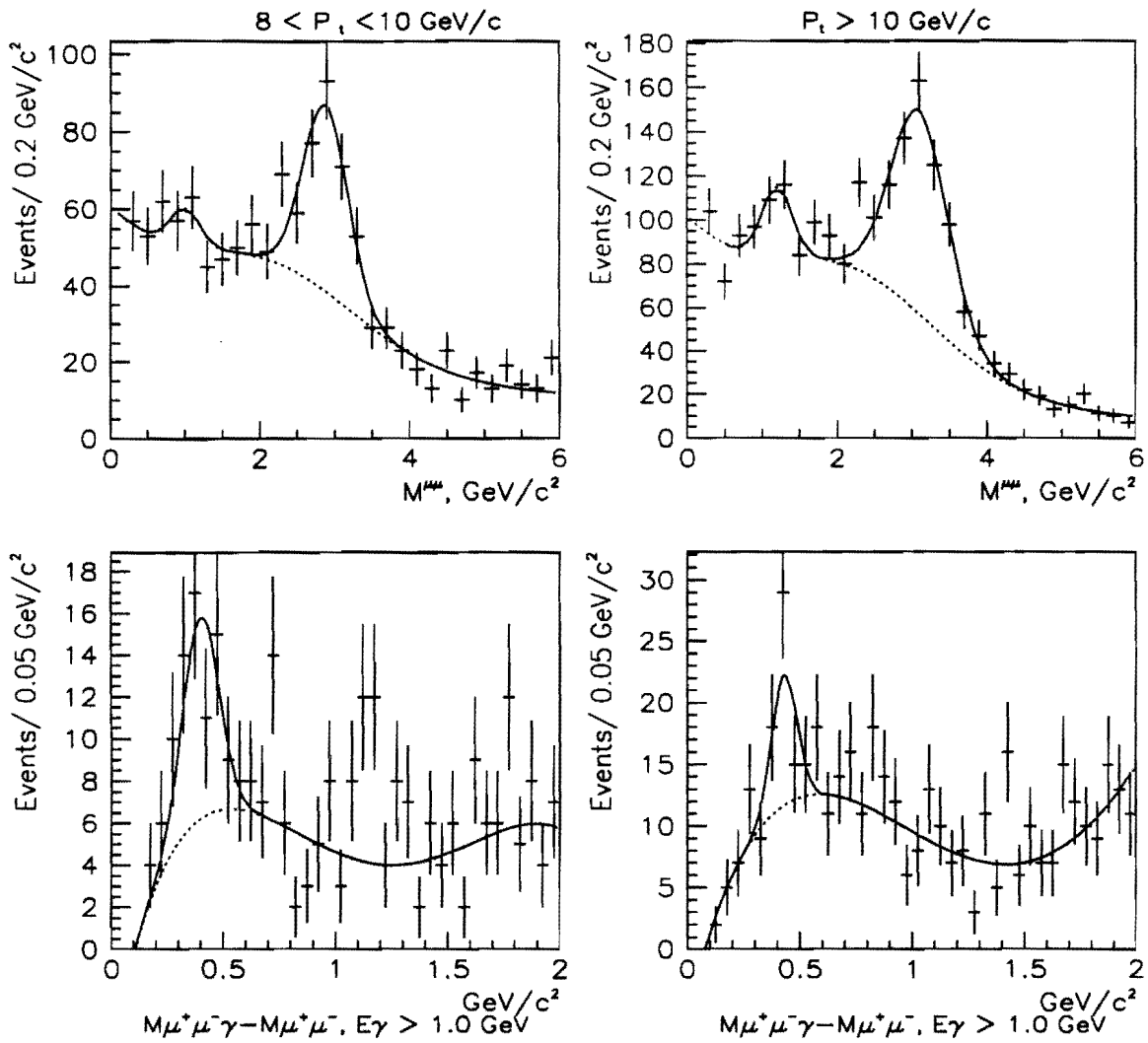

Figure 5.17: The dimuon mass ($M_{\mu\mu}$) spectra and $\Delta M(= M_{\mu\mu\gamma} - M_{\mu\mu})$ spectra for P_t regions: $8 < P_t < 10$ GeV/c and $P_t > 10$ GeV/c

Similarly, the ΔM spectra were fitted to obtain the corresponding numbers of χ_c events. In our fit of the χ_c signal, the width of the gaussian was constrained to agree with the one expected from Monte Carlo simulation. The distribution with higher P_t exhibits a narrower χ_c width. The reason for this behaviour is that the width of the ΔM distribution is determined mostly by the photon energy resolution:

$$\frac{\sigma(\Delta M)}{\Delta M} = \frac{\sigma(E)}{E} = \frac{16\%}{\sqrt{E}},$$

which is better for more energetic photons. At the same time the χ_c with higher P_t is more likely to decay into a photon with higher energy. Thus, the higher P_t ΔM distribution has a narrower width. The obtained numbers of the χ_c events are:

$$N_{\chi_c}(8 < P_t < 10) = 32 \pm 10(\text{stat}) \pm 4(\text{sys}) \text{ events},$$

$$N_{\chi_c}(P_t > 10) = 31 \pm 9(\text{stat}) \pm 4(\text{sys}) \text{ events}.$$

5.6 Isolation requirement

As mentioned in Chapter 2, the direct production mechanism tends to produce an isolated charmonium signal, while both parton fragmentation and b-decay processes produce J/ψ associated with a jet. Hence, the distance from the dimuon to the nearest jet can be a useful parameter for separating different production mechanisms.

The distance between the dimuon and the jet is defined as:

$$\Delta R = (\Delta\phi^2 + \Delta\eta^2)^{1/2},$$

where $\Delta\phi$ is the difference in the ϕ angle of the dimuon and the jet and $\Delta\eta$ is the difference in pseudo-rapidity of the dimuon and the jet. The fraction of events that

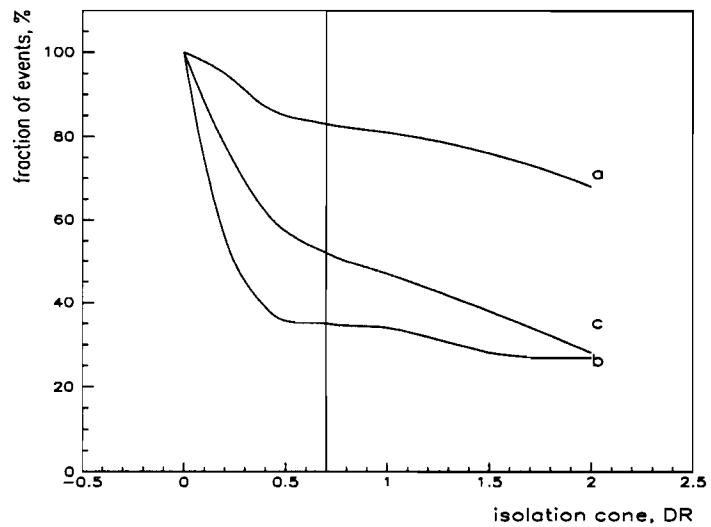

Figure 5.18: The fraction of events that have no jet in the cone, ΔR, around the dimuon, as a function of the size of the cone, ΔR a) J/ψ from χ_c decay; b) J/ψ from b-quark decay; c) parallel and sequential b-quark decay;

have no jet in the cone, ΔR, around the dimuon, as a function of the size of the cone, ΔR, is shown in Figure 5.18 for the processes: direct charmonium production, charmonium production from b-decay and the b-quark parallel and sequential decay. For further analysis, the isolation requirement was chosen as the absence of any jet in the cone defined by $\Delta R < 0.7$ around the dimuon. This is shown in Figure 5.18. Approximately 83% of J/ψ produced in the hard scattering mechanism pass this requirement. Only 35% of the J/ψ from both b-decay and parton fragmentation and 52% of the muons from b-quark semileptonic decay survive this cut.

The isolated dimuon mass spectrum is shown in Figure 5.19. The number of J/ψ

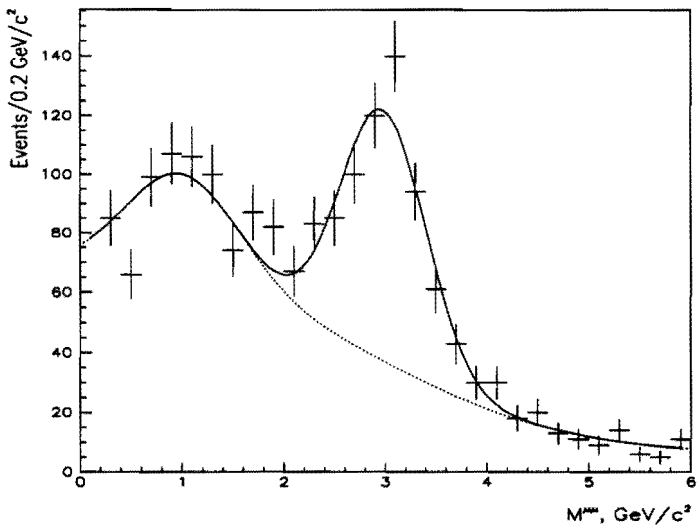

Figure 5.19: The dimuon invariant mass spectrum of isolated muons

events in this sample is obtained from the fit and is:

$$N_{isoJ/\psi} = 324 \pm 31(\text{stat}) \pm 33(\text{sys}) \text{ events.}$$

To understand how many of these events actually come from χ_c decay, the photons from this decay were reconstructed. The corresponding $\Delta M (= M_{\mu\mu\gamma} - M_{\mu\mu})$ spectrum for isolated events is shown in Figure 5.20. The number of the isolated χ_c events was then determined from a fit:

$$N_{iso\chi_c} = 40 \pm 12(\text{stat}) \pm 4(\text{sys}) \text{ events.}$$

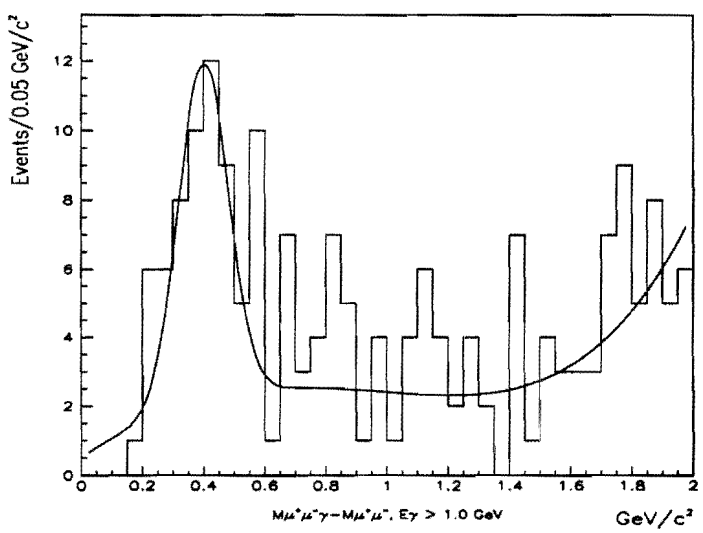

Figure 5.20: The mass difference spectrum ($\Delta M = M_{\mu^+\mu^-\gamma} - M_{\mu^+\mu^-}$) for the isolated dimuon events

Chapter 6

Efficiency Determination

Some of the χ_c mesons that are produced in $p\bar{p}$ collisions inside of the DØ detector do not contribute to the final event sample that is used for the physics studies. The quantity that characterizes the probability of the produced event to contribute to the final event sample is called efficiency (ϵ). It is defined as the ratio of the number of the events in the final sample (N_{final}) to the number of produced events ($N_{initial}$):

$$\epsilon = N_{final}/N_{initial}.$$

Several factors contribute to the overall efficiency. In other words, the probability to contribute to the final event sample is the product of several different efficiencies.

- The detector covers a solid angle that is smaller than 4π. The probability of the final products of the reaction to be in the solid angle of the detector is called the geometrical acceptance.

- Usually the detector can register only those particles that have energy or momentum above a certain threshold. The probability of the products to have

kinematic parameters above the detector threshold is called the kinematic acceptance.

- The probability of the detector to register a particle that has kinematic parameters above the detector threshold is called the registration efficiency.

- Even though a particle has produced hits in the detector, it may not be accepted by the trigger system. The associated probability is referred to as the trigger efficiency. Because there are two levels of triggering at DØ, there exist both Level 1 and Level 2 trigger efficiencies.

- After an event is accepted by the trigger system, it has to be reconstructed. The particle of interest has to be recognized as such by the reconstruction routine. This leads to a reconstruction efficiency.

- Finally, an event is analyzed off-line. The probability to pass the offline selection criteria is called the offline efficiency.

The analysis of these efficiencies is a complicated task, and usually a Monte Carlo simulation of the process of interest is used for this purpose. This method has been discussed in Chapter 4.

To study the efficiency of χ_c-meson identification, the production of this particle was simulated by ISAJET and its special extension for χ_c production – ISACHI[47]. The produced events were then processed by the DØ detector simulation DØ GEANT which simulates the response of all the detector systems. For more realistic calorimeter response the special package NOISY was used and to account for the muon chamber resolution and efficiency the MUSMEAR package was used. Next the events passed

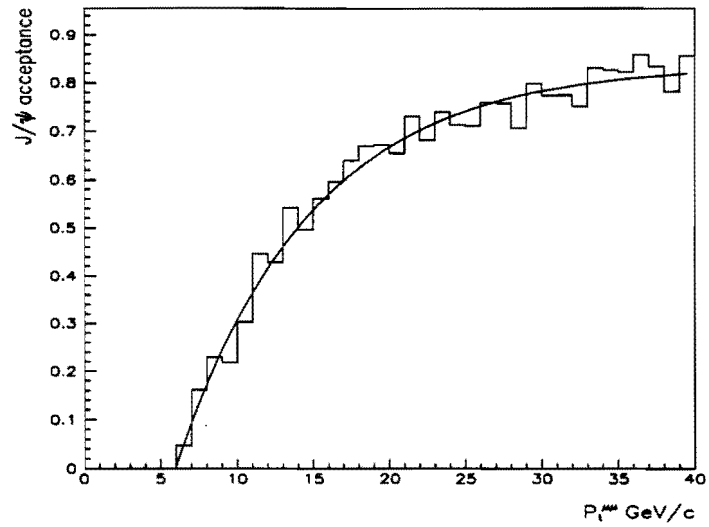

Figure 6.1: The acceptance for muons within $|\eta| < 0.6$ region as a function of the P_t of the dimuon system

through the trigger simulation program and finally they were reconstructed by the same reconstruction program that is used for real events and analyzed with the same analysis code as the real events.

The results of these efficiency studies are discussed in this chapter.

6.1 The J/ψ Kinematic Region

As was stated in Chapter 5, only dimuons with transverse momentum ($P_t^{\mu\mu}$) greater than 8 GeV/c and in the pseudo-rapidity ($\eta^{\mu\mu}$) region from – 0.6 to 0.6 contribute to the final event sample. These requirements specify the kinematic region in which the χ_c production cross section is studied. To avoid any uncertainty associated

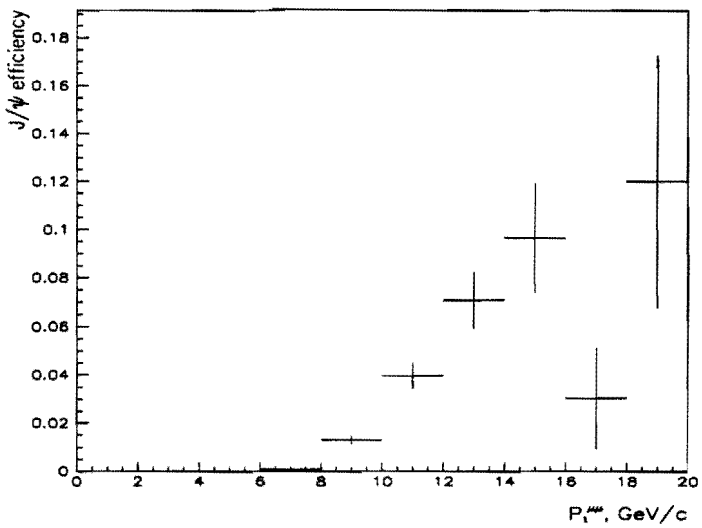

Figure 6.2: The J/ψ efficiency dependance on the transverse momentum of the dimuon system

with the production model used in the Monte Carlo simulation, the resultant χ_c cross section is not corrected for these acceptance cuts. All further studies are done with these cuts implicitly imposed.

6.2 Muon Acceptance

Acceptable muons were required to have $P_t^\mu > 3.5$ GeV/c and to be in the $|\eta^\mu| < 0.8$ region. The acceptance for these requirements as a function of the $P_t^{\mu\mu}$ of the dimuon system, is shown in Figure 6.1. The average acceptance was found to be 34.0 ± 1.0 %.

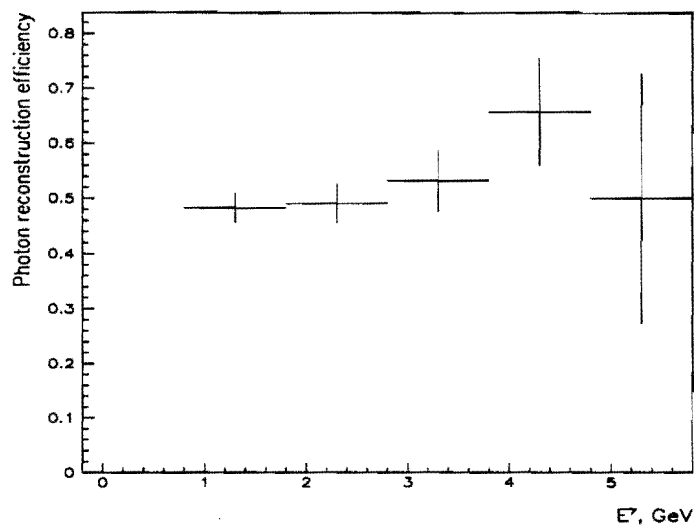

Figure 6.3: The dependance of the efficiency of photon reconstruction as a function of energy

6.3 J/ψ Identification Efficiency

The combined MU_2_HIGH trigger, registration, reconstruction and off-line efficiency of J/ψ identification has been studied. An off-line cut was made on the invariant mass of the dimuon system of $2 < M_{\mu\mu} < 4$ GeV/c^2 to minimize the contribution from the backgrounds to the J/ψ signal. This point was discussed in Chapter 5.

Because the muon system is more efficient for muons with higher momenta, the J/ψ efficiency also grows with the transverse momentum of the dimuon system. The average efficiency for identification of the J/ψ with $P_t^{\mu\mu} > 8$ GeV/c and $|\eta^{\mu\mu}| < 0.6$ is 8.83 ± 0.66 %.

The efficiency time acceptance of the J/ψ identification is then 3.0 $\pm$ 0.5 %. Its dependance on $P_t^{\mu\mu}$ is shown in Figure 6.2.

6.4 Photon Acceptance

The energy of the photon from the χ_c decay is required to be greater than 1.0 GeV. The acceptance to this cut must be calculated with the imposed constraint on the $P_t^{\mu\mu}$ of the J/ψ, as these two parameters are strongly correlated: i.e. the higher the transverse momentum of the J/ψ the higher the probability to have a higher photon energy. With this constraint the photon acceptance was found to be 60.0 $\pm$ 0.76 %.

6.5 Photon Reconstruction Efficiency

The efficiency for finding a low energy electromagnetic cluster depends on its energy, viz. the higher the energy, the better shaped is the cluster, thus the probability of finding it is higher. In other words, the efficiency of photon reconstruction grows with energy. Reconstruction of the χ_c meson necessitates reconstruction of the J/ψ signal and finding a photon with energy greater than 1.0 GeV. An additional requirement was imposed that the photon should not share its calorimeter cell with any of the muons, in other word the distance from the photon cluster to either muon track must be greater than 0.1:

$$\Delta R = (\Delta\phi^2 + \Delta\eta^2)^{1/2} > 0.1,$$

$$\Delta\phi = \phi_\mu - \phi_\gamma, \qquad \Delta\eta = \eta_\mu - \eta_\gamma.$$

The photon finding efficiency as a function of a photon energy is shown in Figure 6.3.

The average reconstruction efficiency for the photon from χ_c decay is 50.0 ± 2.4 % for photon energy greater than 1.0 GeV.

6.6 Systematic Errors

Systematic errors are introduced in the efficiency calculation by the uncertainty in the production model. The acceptance and the reconstruction efficiency are sensitive to the P_t and angular distributions of the final products in the reaction.

In our efficiency evaluation we have used the direct production model of the χ_c. As was pointed out, the production cross section in this model behaves like P_t^{-6}. Compared to the P_t^{-4} behavior, which is exhibited by the gluon fragmentation mechanism, the direct production model tends to populate the lower P_t region, thus producing photons with lower energies and a lower efficiency than for the case of the fragmentation mechanism. At the same time, the main contribution to the event sample is done by the J/ψ with the lowest possible P_t, and hence lowest energy photons. Hence, this will not lead to large changes in the efficiency. Estimates show that the difference in the P_t behavior introduces a relative increase of 24% in the J/ψ registration efficiency and about 9% in the photon reconstruction efficiency.

The angular distribution of the photon depends on the polarization (α) of the χ_c:

$$\frac{d\sigma}{d\Omega} \sim (1 + \alpha \cos^2\theta),$$

where θ is the angle between the χ_c and the photon. The experimental value of the polarization parameter α is not reliably measured yet. In our efficiency studies we used the unpolarized model. In other words, α was assumed to be zero. For the extreme cases of polarization the photon efficiency varies from $\Delta\epsilon_\gamma/\epsilon_\gamma = -3.3\%$ for $\alpha = +1$ to $\Delta\epsilon_\gamma/\epsilon_\gamma = 8.8\%$ for $\alpha = -1$. The J/ψ acceptance was studied for different values of α. For the extreme values of ± 1 the corresponding relative acceptance changes are $\pm 7\%$. Summing this up, the production model introduces a relative systematic error of $\pm^{25}_{7}\%$ in the J/ψ registration efficiency, and $\pm^{13}_{3.3}\%$ error in the photon registration efficiency.

Chapter 7

Results and Conclusion

7.1 Presentation of the Result

In production experiments, the final results are usually expressed in terms of the total production cross section (σ):

$$\sigma = \frac{N_{events}}{L\,\epsilon},$$

where N_{events} is the number of observed events of a particular process, L is the integrated luminosity for this data set and ϵ is the efficiency of detecting, identifying and reconstructing the process. The result, expressed in terms of the production cross section, can be compared to the results of other experiments and to theoretical predictions.

The cross section provides information about the absolute rate of the process. When the problem is to distinguish between different production mechanisms, the result can also be expressed in terms of the relative fraction of a particular mechanism. In the case of J/ψ production, it is the relative fraction of J/ψ coming from χ_c decay

(F) that is important:

$$F = \frac{N_{\chi_c}}{N_{J/\psi}\ \epsilon_\gamma},$$

where N_{χ_c} is the number of fully reconstructed χ_c events, $N_{J/\psi}$ is the number of J/ψ events and ϵ_γ is the efficiency to register the photon from χ_c decay.

Sometimes the dependence of the production rate on some kinematic parameter gives even more information than the total rate. In the case of charmonium production, as was discussed in Chapter 2, the dependence of the cross section, or the relative fraction, on the $P_t^{\mu\mu}$ of the charmonium helps to distinguish the charmonium production mechanisms. The fraction of J/ψ coming from χ_c decay as a function of $P_t^{\mu\mu}$ is expressed as:

$$F(P_t^{\mu\mu}) = \frac{N_{\chi_c}(P_t^{\mu\mu})}{N_{J/\psi}(P_t^{\mu\mu})\ \epsilon_\gamma(P_t^{\mu\mu})},$$

where the efficiency, $\epsilon_\gamma(P_t^{\mu\mu})$, must be regarded as a function of $P_t^{\mu\mu}$.

In this chapter we discuss all of these three representations of the results on charmonium production at DØ.

7.2 Determination of the Fraction of J/ψ Coming from χ_c Decay

The number of fully reconstructed χ_c events (N_{χ_c}), the number of J/ψ events ($N_{J/\psi}$) and the efficiency to register the photon from χ_c decay (ϵ_γ) are summarized in Table 7.1. The fraction of J/ψ coming from χ_c decay is

$$F_{\chi_c} = \frac{N_{\chi_c}}{N_{J/\psi}\epsilon_\gamma} = 30 \pm 7 \pm^{4.2}_{5.6}\ \%,$$

N_{χ_c}	66 ± 15 (stat) ± 5 (sys)
$N_{J/\psi}$	722 ± 52 (stat) ± 72 (sys)
Efficiency ϵ_γ, %	$30 \pm^{4.2}_{1.8}$

Table 7.1: The number of fully reconstructed χ_c events, the number of J/ψ events and the efficiency to register the photon from χ_c decay

where the first uncertainty is statistical and the second is systematical.

7.3 Cross Section Determination

In this thesis we study the production of χ_c mesons in $p\bar{p}$ collisions. The χ_c meson is observed in the decay chain:

$$\chi_c \to J/\psi + \gamma,\ J/\psi \to \mu^+ + \mu^-.$$

Thus the result must be the cross section of χ_c production times the branching ratio of its radioactive decay to J/ψ times the branching ratio of J/ψ decay to two muons $(\sigma(p\bar{p} \to \chi_c X)Br(\chi_c \to J/\psi + \gamma)Br(J/\psi \to \mu^+ + \mu^-))$.

As was already stated, the cross section is determined for the following kinematic region of the J/ψ:

$$|\eta(J/\psi)| < 0.6, \qquad P_t(J/\psi) > 8 \text{ GeV/c}.$$

As was already stated in Chapter 5, only part of the J/ψ data sample is used to determine the production cross section, which is defined as a product of the J/ψ

$N_{J/\psi}$	444 ± 36 (stat) ± 44 (sys)
Luminosity L, pb^{-1}	6.6 ± 0.8
Efficiency $\epsilon_{J/\psi}$, %	$3.0 \pm^{0.9}_{0.5}$

Table 7.2: The number of J/ψ events, the total integrated luminosity of this data set and the efficiency of J/ψ registration

cross section and the fraction of the J/ψ coming from χ_c decay:

$$\sigma(p\bar{p} \to \chi_c\, X)\ \ Br(\chi_c \to J/\psi + \gamma)\ \ Br(J/\psi \to \mu^+ + \mu^-) =$$
$$= \sigma(p\bar{p} \to J/\psi X)\ \ Br(J/\psi \to \mu^+ + \mu^-)\ \ F_{\chi_c}.$$

The number of J/ψ events, the total integrated luminosity of this data set and the efficiency of J/ψ registration are summarized in Table 7.2 together with their statistical and systematical uncertainties. These values yield the cross section of J/ψ production

$$\sigma(p\bar{p} \to J/\psi\ X)\ \ Br(J/\psi \to \mu^+ + \mu^-) = 2.24 \pm 0.18 \pm^{0.5}_{0.74} \text{nb},$$

where the first uncertainty is statistical and the second is systematical.

Together with the fraction this yields:

$$\sigma(p\bar{p} \to \chi_c\, X)\ \ Br(\chi_c \to J/\psi + \gamma)\ \ Br(J/\psi \to \mu^+ + \mu^-) = 0.67 \pm 0.16 \pm^{0.18}_{0.25} \text{nb},$$

where the first uncertainty is statistical and the second is systematical.

$P_t^{\mu\mu}$ range, GeV/c	$8 < P_t < 10$	$P_t > 10$
N_{χ_c}	$32 \pm 10(stat) \pm 4(sys)$	$31 \pm 9(stat) \pm 4$
$N_{J/\psi}$	$203 \pm 29(stat) \pm 20(sys)$	$498 \pm 38(stat) \pm 50(sys)$
ϵ_γ, %	$25.3 \pm^{3.3}_{2.6}$	$30.4 \pm^{4.0}_{3.1}$

Table 7.3: Number of χ_c and J/ψ events and photon efficiency for two $P_t^{\mu\mu}$ regions

7.4 The P_t Dependance of the Fraction of J/ψ Coming from χ_c Decay.

Using the results on the numbers of χ_c and J/ψ events for the two P_t regions and the P_t-dependance of the photon identification efficiency, which are summarized in Table 7.3, it is possible to determine the P_t dependance of the fraction of J/ψ coming from χ_c decay. This yields:

$$F_{\chi_c}(8 < P_t < 10) = 63 \pm 21(\text{stat}) \pm^{12}_{13} (\text{sys})\% \text{ and}$$

$$F_{\chi_c}(P_t > 10) = 22 \pm 6.6(\text{stat}) \pm^{4.2}_{4.6} (\text{sys})\%.$$

In other words, in the low P_t region approximately 60% of the J/ψ are from χ_c decay, whereas in the high P_t region only about 20% of the J/ψ are from χ_c decay. The errors are large and do not allow us to perform a detailed quantitative analysis of this result, e.g. to determine the power of the P_t-dependance, but qualitatively it agrees with our expectations: the J/ψ in the lower P_t-region where direct production is the most important mechanism, come mostly from χ_c decay, while in the high P_t-region where the b-decay mechanism becomes significant, the fraction of the J/ψ coming

from χ_c decay is much reduced.

7.5 Isolated χ_c.

Isolation is another tool in the separation of the production mechanisms. Assuming that all the isolated χ_c come from direct charmonium production we can determine the relative contribution of this mechanism to χ_c production:

$$F_{direct} = \frac{N_{iso\chi_c}}{N_{\chi_c}\epsilon_{iso}},$$

where $\epsilon_{iso}(= 83 \pm 4\%)$ is the acceptance to the isolation cut. This yields:

$$F_{direct} = \frac{(40 \pm 12 \pm 4)}{(66 \pm 15 \pm 5) \times (0.83 \pm 0.04)} = 73 \pm 24(\text{stat}) \pm 8.8(\text{sys})\%.$$

7.6 Discussion of the Different Production Mechanisms.

Of course, statistics are very limited and the errors are too large to allow strong statements to be made about the relative fraction of the charmonium production mechanisms. Moreover, the uncertainty in the fraction of the χ_c coming from b-decay does not allow separation of the gluon fragmentation and b-decay mechanisms.

The inclusive J/ψ production from b-decay is currently being studied using DØ data. In this analysis, one tags the second b-quark by its semileptonic decay to a muon. In principle, the same analysis could be performed on the χ_c event sample. Unfortunately, the limited statistics and high background do not allow for it with the present data sample.

Summarizing our results on the production mechanism, the P_t dependance of the fraction of J/ψ coming from χ_c decay agrees qualitatively with the one predicted by the charmonium production models. The relative fraction of χ_c coming from direct production is

$$F_{direct} = 73 \pm 24(\text{stat}) \pm 8.8(\text{sys})\%.$$

7.7 Conclusion

Using DØ data from Tevatron run 1a, 66 ± 15 χ_c events were reconstructed. The measured cross section of the χ_c production times the branching ratio of χ_c radiative decay to J/ψ is $0.67 \pm 0.16 \pm^{0.18}_{0.25}$ nb for the kinematic region $P_t(J/\psi) >$ 8 GeV/c, and $|\eta| < 0.6$. A similar analysis was attempted by the CDF collaboration [48]. The result obtained there is $3.2 \pm 0.4 \pm^{1.2}_{1.1}$ nb for the J/ψ kinematic region $P_t(J/\psi) > 6$ GeV/c, and $|\eta| < 0.5$. These two results can be compared assuming the power of the P_t-dependance of the production cross section ($\frac{d\sigma}{dP_t^2}$). If we assume P_t^{-6}, as predicted by the direct production model, then the extrapolation of the CDF result to the DØ kinematic region yields $1.22 \pm 0.15 \pm^{0.46}_{0.42}$ nb. If we assume the power of P_t^{-4}, as predicted by the gluon fragmentation model, then the extrapolation gives $2.1 \pm 0.27 \pm^{0.81}_{0.74}$ nb. Clearly comparison of the DØ and CDF data favors P_t^{-6}.

A quantitative theoretical prediction exists for the direct χ_c production mechanism [25], this is 196 nb for $P_t(J/\psi) > 5$ GeV/c. Corrected for the branching ratio ($Br(J/\psi \rightarrow \mu^+\mu^-) = 6\%$) and for the kinematic region the expected cross section would be 0.36 nb. This prediction is within errors in agreement with the DØ result; although it is tempting to interpret the excess in the measured cross section as the

gluon fragmentation contribution to the χ_c production.

In conclusion, we have shown in this thesis that it is possible to identify $\chi_c \rightarrow J/\psi + \gamma$ events in the DØ event sample from run 1a and to make a determination of the production cross section. The limited statistics make it difficult to produce compelling quantitative results, although studies of the alternate production mechanisms indicate qualitatively that for the low P_t region direct charmonium production is the most important mechanism of the charmonium production, while for the higher P_t region b-quark decay becomes more significant. There are indications that the gluon fragmentation mechanism also contributes to charmonium production.

More data obtained during Tevatron run 1b(1994 - 1995) and run 2 (1997 - 1998) should yield interesting results and allow a detailed discrimination of the χ_c production mechanisms.

Chapter 8

Charmonium Physics with the DØ Upgrade

In the following chapter we briefly discuss the plans for the DØ upgrade and the resulting potential for charmonium production physics.

8.1 Problems

In the present experiment it has proven possible to establish reliable J/ψ and χ_c signals; however some physics tasks still remain to be addressed:

- Because of the current limited statistics, the errors on the cross section and fractions are high. It is difficult to separate the different mechanisms of charmonium production.
- As was already stated several times, the DØ detector has no central magnetic field. The momenta of muons are measured by the bend in the iron toroidal magnet of the muon system. The muon momentum resolution is limited to 18% by multiple scattering inside the toroid. This leads to a mass resolution at the J/ψ of about 0.4 GeV/c^2. For this reason, it is difficult to separate the J/ψ signal from the background processes discussed in Chapter 5.

- Low vertex resolution did not allow a reliable reconstruction of the secondary vertex of b-decay to J/ψ. This also would be a powerful tool in distinguishing charmonium production mechanisms.

8.2 The DØ Upgrade

The approved upgrade of the Tevatron and the DØ detector offers solutions to all of the discussed problems for the investigation of charmonium production.

8.2.1 Main Injector

The construction of the Main Injector [49], where protons and antiprotons will be stored before injecting into the Tevatron, will cause the luminosity to increase up to 5×10^{31}. This is 10 times higher than the record luminosity for the run when the discussed data was collected. In other words, one year of running will deliver 10 times more events than presently. The high luminosity runs are planned to begin in 1996.

8.2.2 The DØ Upgrade

The goals of the DØ upgrade [50] are: an improvement of the momentum resolution for charged particles; better reconstruction of secondary vertices; better radiation stability to allow the detector to operate in the high luminosity environment.

To achieve these goals the following upgrade was proposed. The entire tracking system of the present DØ detector, consisting of the Vertex Detector, the Transition Radiation Detector and the Central and Forward Drift Chambers will be replaced by silicon microstrip barrel and disk detectors along with a scintillating fiber tracker.

These new detector systems will be located inside a superconducting solenoid magnet. A scintillating strip based preshower detector will be located just outside the magnet. The upgrade will proceed in two stages. First the silicon microstrip barrel and the inner part of the fiber tracker will be installed; then the remaining parts of the system will take their place in the DØ detector. The layout of the DØ upgrade showing solenoid, scintillating fiber super-layers, silicon barrels and disks and the preshower detector is presented in Figure 8.1.

8.2.3 The DØ Central Magnetic Field

The new DØ superconducting magnet will provide a 2 Tesla magnetic field in a volume of radius $r = 62$ cm and $|z| < 140$ cm.

8.2.4 The DØ Silicon Vertex Detector

The DØ Silicon Vertex Detector consists of four barrels layers, layers 1 and 3 are single-sided; layers 2 and 4 are double sided. Twelve double sided disks are located in $|z| < 70$ cm with inner radius of 3 and outer radius of 10 cm.

Larger single sided disks located at the end of the inner fiber super-layer at $\pm$ 130 cm in z are an option that is presently under study. The DØ Silicon Vertex Detector is expected to provide secondary vertex resolution better than 30 μm.

8.2.5 The DØ Fiber Tracking System

The current scintillating fiber tracker design consists of four super-layers of fibers arranged at radii of 20, 33, 44 and 55 cm inside the superconducting magnet. The inner super-layer is 256 cm long, all the other super-layers are 280 cm long. In each

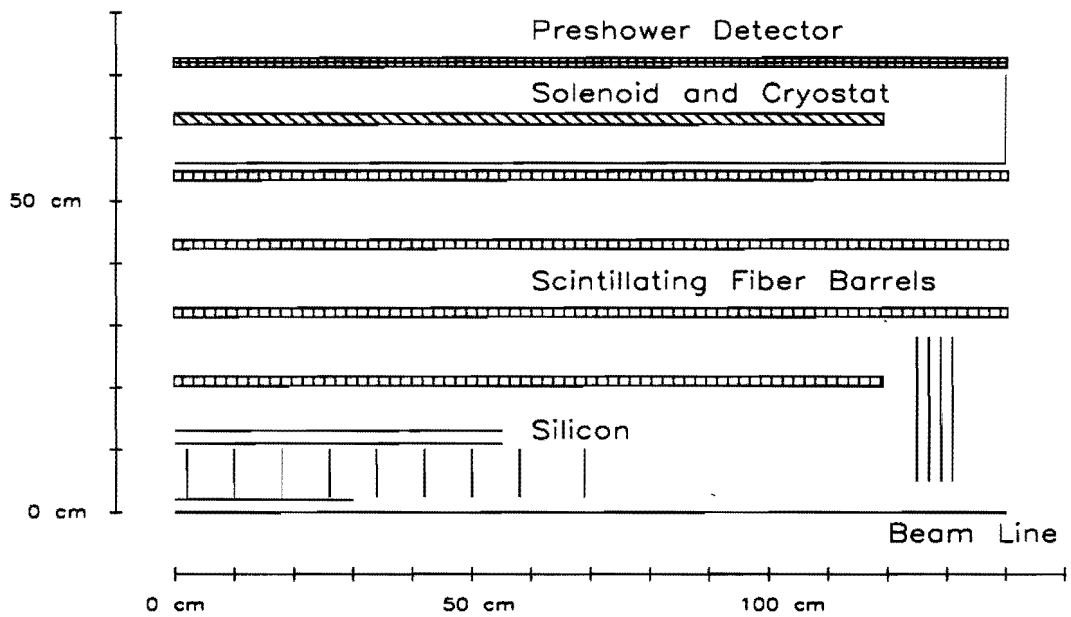

Figure 8.1: Layout of the DØ upgrade showing solenoid, scintillating fiber super-layers, silicon barrels and disks and the preshower detector.

super-layer the fibers are arranged in four doublets. Two of the fiber doublets are parallel to the beam axis, the other two are oriented with a stereo angle of $\pm 3^\circ$ with respect to the axial doublets. This provides a measurement of the z coordinate. The spacing between fibers in each layer is 0.87 mm. Two singlets forming a doublet have a relative offset of a half-fiber-width to ensure a better doublet detection efficiency. The optical signal from the fibers will be detected by Visible Light Photon Counters (VLPCs). VLPCs are doped silicon diodes, produced by Rockwell International.

8.3 Cosmic Ray Test of the DØ Fiber Tracking System

The performance of the main components of the DØ fiber tracking system, scintillating fibers and VLPC's, was tested with cosmic ray muons. In this section we discuss the setup and the results of this Cosmic Ray Test (CRT) [51].

8.3.1 The Cosmic Ray Test Setup

The fiber super-layers used in the Cosmic Ray Test have the same geometric parameters as for the DØ upgrade. The layout of the Cosmic Ray Test stand has a cylindrical geometry similar to the detector design. The schematic layout of the Cosmic Ray Test stand is shown in Figure 8.2.

The system consists of three superlayers of scintillating fibers mounted on a carbon cylinder. Two 1x2.5x0.8 m^3 steel blocks, layered with plastic scintillators, used as triggers, serve as muon filters to select muons with momenta of approximately > 2.5 GeV/c.

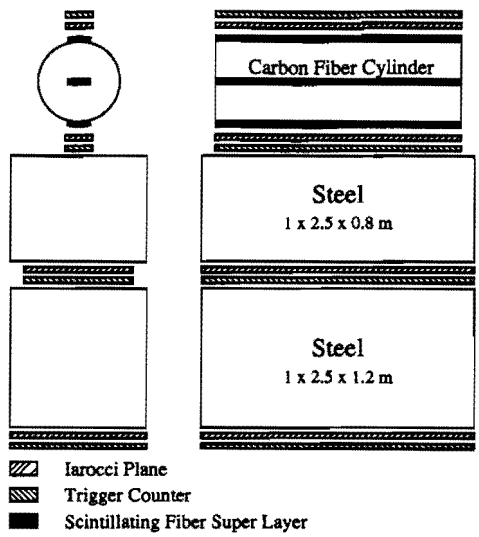

Figure 8.2: The schematic layout of the Cosmic Ray Test stand

8.3.2 The Cosmic Ray Test Results

The test results show that the prototype of the fiber tracking system performed very well. The efficiency of a doublet was found to be about 99.5%. The track resolution provided by this system was found to be 163.3 μm.

8.4 Estimates for Charmonium Production with the Upgraded DØ Detector

The upgraded Tevatron will deliver ten times higher luminosity than in the present experiment. This means, that in one year of running about 10 thousand J/ψ will be registered by the DØ detector, even if its efficiency will be the same. A central magnetic field will improve the momentum resolution of the DØ detector by a

factor of about 5.5. Monte Carlo studies have shown that the width of the J/ψ signal in the upgraded DØ detector will be 0.072 GeV/c^2, compared to 0.4 GeV/c^2 in the present experiment. This will produce a reduction in background contamination by the same factor of 5.5. The expected signal to background ratio will be 1.8 as compared to 0.33 presently. These improvements will allow a reduction of the relative error on the J/ψ production cross section by a factor of 4.

The DØ Silicon Vertex Detector will provide secondary vertex resolution better than 30μm. The mean b lifetime is 300 μm. This will allow us to separate the b-decay production mechanism of the J/ψ, while the increased statistics will enable us to determine the fraction of direct charmonium production.

In summary, the upgraded DØ detector provides many exciting possibilities for charm and beauty physics.

Bibliography

[1] V.D.Barger, R.J.N.Phillips: *Collider Physics* Addison-Wesley, New York (1988).

[2] L.M.Lederman, "The Tevatron" in *Sci.Am.*, Vol.264, Num.3, (Scientific American, Inc., New York, March 1991) p.53.

[3] F.Abe, *et al.*, Nuclear Instruments and Methods, **A 271**, (1988).

[4] S.Abachi, *et al.*, The DØ Detector, Nuclear Instruments and Methods, **A 338**, (1993).

[5] F.Halzen, A.D.Martin: *Quarks and Leptons*, Wiley, New York (1984).

[6] A.H.Mueller, *Perturbative QCD at High Energies*, Phys. Rep. **73C**, 237 (1981).

[7] Particle Data Group, L.Montanet *et al.* , Review of Particle Properties, Physical Review, **D 50**, Part I, 1173 (1994).

[8] B.Richter, From the ψ to charm: The experiment of 1975 and 1976, *The 1976 Nobel prize address*, Rev. Mod. Phys. **49**, 251 (1977)

[9] S.C.C.Ting, The discovery of the J particle: A personal recollection, *The 1976 Nobel prize address*,Rev. Mod. Phys. **49**, 235 (1977)

[10] G.Altarelli, *Partons in QCD,* Phys. Rep. **81**, 1 (1982)

[11] D.W.Duke, J.F.Owens, Q^2 - *Dependent Parametrizations of Parton Distribution Functions*, Phys. Rev. **D30**, 49 (1984)

[12] E.W.N.Glover, A.D.Martin and W.J.Stirling, Z. Phys. **C 38**, 473 - 478 (1988).

[13] D.H.Saxon, *Quark and Gluon Fragmentation*, **Electron-Positron Physics**, A.Ali, P.Söding, *eds.*, World Scientific (1987)

[14] E.Braaten and Tzu Chiang Yuan, Fermilab preprint, FERMILAB-PUB-94/040-T (1994).

[15] M.Cacciari and M.Greco, FNT/T-94/13, hep-ph/9405241

[16] E.Braaten, M.A.Doncheski, S.Fleming and M.L.Mangano, FERMILAB-PUB-94/135-T, hep-ph/9405407 (1994).

[17] E.Braaten and Tzu Chiang Yuan, *Phys. Rev. Lett.*, **71** 1673 (1993).

[18] M.A.Doncheski, S.Fleming and M.L.Mangano, FERMILAB-CONF-93/348-T, (1993)

[19] E.Braaten, K.Cheung and T.C.Yuan, *Phys.Rev*, **D 48** 4230 (1993).

[20] E.Braaten, K.Cheung and T.C.Yuan, *Phys.Rev*, **D 48** R5049 (1993).

[21] R.Baier and R.Rückl, Z. Phys. **C 19** , 251 - 266 (1983).

[22] R.Baier and R.Rückl, Nuclear Physics **B 208** , 381 -396 (1982).

[23] B.Humpert, Physics Letters **B 184** 105 - 107 (1987).

[24] R.Gastmans, W.Troost and Tai Tsun Wu, Physics Letters **B 184** 257 - 260 (1987).

[25] E.W.N.Glover, F.Halzen and A.D.Martin, Physics Letters **B 185**, 441 - 445 (1987).

[26] P.Nason, S.Dawson and R.K.Ellis, Nucl. Phys. **B 327**, 49 (1989).

[27] J.H.Kühn, S.Nussinov and R.Rückl, Z.Phys. **C 5**, 117 (1980).

[28] J.H.Kühn and R.Rückl, Physics Letters **B 135**, 477 (1984).

[29] H.Fritzch, Phys. Letters, **B 86** 164 (1979).

[30] H.Fritzch, Phys. Letters, **B 86** 343 (1979).

[31] P.H.Cox *et al.*, Phys Rev., **D 32** 1157 (1985).

[32] G.T.Bodwin, E.Braaten, T.C.Yuan and G.P.Lepage, Phys. Rev., **D 46** R3703 (1992).

[33] L3 Collaboration, O.Adriani *et al.*, Physics Letters **B 317** 467 (1993).

[34] ARGUS Collaboration, H.Albrecht *et al.*, *Phys. Lett.*, **B 277** 209 (1992)

[35] "Collider Run Sets World Luminosity Records" in *Fermilab Annual Report, 1992,* p.9 (unpublished)

[36] N.Amos *et al*, Luminosity Calculations for DØ, DØ Internal Note 2031, (1994).

[37] N.Amos *et al*, Physics Letters **B 243** 158 (1990).

[38] N.Amos *et al*, Phys. Rev. Letters **63** 2784 (1989).

[39] The CDF Collaboration, G.Chiarelli *et al*, Fermilab preprint, FERMILAB-Conf-93/360-E, (1993).

[40] The CDF Collaboration, S.Belforte *et al*, Fermilab preprint, FERMILAB-Conf-93/358-E, (1993).

[41] *Determination of the Strong Coupling Constant (α_s) and a Test of Perturbative QCD Using W+ Jets Process in the DØ Detector* by Jaehoon Yu, SUNY at Stony Brook, Aug 1993, Ph.D.Thesis.

[42] "D0$MUON_UTIL$DOCS:MUON_ANALYSIS.MEM" D.Hedin, DØ Online documentation.

[43] F.Paige, S.D.Protopopesku, ISAJET Monte Carlo version 6.36, BNL Report No. BNL38034, 1986 (unpublished).

[44] R. Brun and F. Carminati, "GEANT Detector Description and Simulation Tool," CERN, CERN Program Library Long Writeup W5013 (1993).

[45] "D0$CALOR_OFF:NOISY.DOC" DØ Online documentation.

[46] "D0$MUON_UTIL$DOCS:MUON_UTIL.DOC" T. Diehl DØ Online documentation.

[47] *Chi Meson Production in Proton-Antiproton Interactions at a Center of Mass Energy of 1.8 TeV* by Christopher M. Boswell, The John Hopkins University, Nov 1993, Ph.D. Thesis.

[48] CDF Collaboration, C.M.Boswell, FERMILAB-Conf-92/347-E (1992)

[49] "Main Injector Construction Begins" in *Fermilab Annual Report, 1992,* p.42 (unpublished)

[50] E823 (DØUpgrade), DØ Internal Note 1322, (1992) (unpublished).

[51] Proceedings of DPF '94, to be published

APPENDIX

QCD Cross Section

The QCD cross sections are expressed in terms of the invariants:

$$\hat{s} = (k_1 + k_2)^2,$$

$$\hat{t} = (k_2 - k_3)^2,$$

$$\hat{u} = (k_1 - k_3)^2,$$

where k_1 and k_2 are the 4-momenta of the initial partons in the hard-scattering processes and k_3 is the 4-momentum of a final parton.

R_0 is related to the $q\bar{q}$ wave function at the origin, while R_1' is related to its derivative at the origin.

To order α_s^2 one only has the gluon fusion processes, g g $\rightarrow$ $^{2S+1}L_J$ with the cross section [21], [22]:

$$\sigma(^1S_0) = \frac{\pi^2\,\alpha_s^2\,R_0^2}{3\,M^3\,\hat{s}}\;\delta(1 - \frac{M^2}{\hat{s}}),$$

$$\sigma(^3P_0) = \frac{12\,\pi^2\,\alpha_s^2\,R_1'^2}{M^5\,\hat{s}}\;\delta(1 - \frac{M^2}{\hat{s}}),$$

$$\sigma(^3P_2) = \frac{16\,\pi^2\,\alpha_s^2\,R_1'^2}{M^5\,\hat{s}}\;\delta(1 - \frac{M^2}{\hat{s}}).$$

To order α_s^3 one has typically two-by-two scattering processes. The relevant cross section are given below:

(a) g $q \to {}^{2S+1}L_J\, q$ or $(q \to \bar{q})$ with [21], [22]

$$\frac{d\sigma}{d\hat{t}}({}^1S_0) = \frac{2\,\pi\,\alpha_s^3\,R_0^2}{9M\,\hat{s}^2}\cdot\frac{(\hat{t}-M^2)^2-2\,\hat{s}\,\hat{u}}{(-\hat{t})(\hat{t}-M^2)^2},$$

$$\frac{d\sigma}{d\hat{t}}({}^3P_0) = \frac{8\,\pi\,\alpha_s^3\,R_1'^2}{9M^3\,\hat{s}^2}\cdot\frac{(\hat{t}-3\,M^2)^2-(\hat{s}^2+\hat{u}^2)}{(-\hat{t})(\hat{t}-M^2)^4},$$

$$\frac{d\sigma}{d\hat{t}}({}^3P_1) = \frac{16\,\pi\,\alpha_s^3\,R_1'^2}{3M^3\,\hat{s}^2}\cdot\frac{-\hat{t}(\hat{s}^2+\hat{u}^2)-4M^2\hat{s}\hat{u}}{(\hat{t}-M^2)^4},$$

$$\frac{d\sigma}{d\hat{t}}({}^3P_2) = \frac{16\,\pi\,\alpha_s^3\,R_1'^2}{9M^3\,\hat{s}^2}\cdot\frac{(\hat{t}-M^2)^2(\hat{t}^2+6\,M^4)-2\hat{s}\hat{u}(\hat{t}^2-6M^2(\hat{t}-M^2))}{(-\hat{t})(\hat{t}-M^2)^4}.$$

(b) $q\,\bar{q} \to {}^{2S+1}L_J$ g with [21], [22]

$$\frac{d\sigma}{d\hat{t}}({}^{2S+1}L_J) = -\frac{8}{3}\,\frac{\hat{t}^2}{\hat{s}^2}\cdot\frac{d\sigma}{d\hat{t}}(g\,q \to \ {}^{2S+1}L_J\,q)|_{\hat{t}\leftrightarrow\hat{s}}$$

(c) g g $\to {}^{2S+1}L_J$ g with [23], [24]

$$\frac{d\sigma}{d\hat{t}}({}^3S_1) =$$

$$= \frac{5\,\pi\,\alpha_s^3\,R_0^2}{9M\,\hat{s}^2}\cdot\frac{M^2}{(\hat{s}-M^2)^2(\hat{t}-M^2)^2(\hat{u}-M^2)^2}\cdot\{[\hat{s}^2(\hat{s}-M^2)^2]+[\hat{s}\to\hat{t}]+[\hat{s}\to\hat{u}]\}$$

$$\frac{d\sigma}{d\hat{t}}({}^1S_0) =$$

$$= \frac{\pi\,\alpha_s^3\,R_0^2}{2M\,\hat{s}^2}\cdot\frac{1}{\hat{s}\hat{t}\hat{u}(\hat{s}-M^2)^2(\hat{t}-M^2)^2(\hat{u}-M^2)^2}\cdot\{[\hat{s}^4(\hat{s}-M^2)^2((\hat{s}-M^2)^2+2M^4)-$$

$$-3/4\hat{s}\hat{t}\hat{u}(\hat{s}^2+\hat{t}^2+\hat{u}^2)\cdot(\hat{s}-M^2)(\hat{t}-M^2)(\hat{u}-M^2)+$$

$$+16/3\,M^2\,\hat{s}\hat{t}\hat{u}(\hat{s}^2\hat{t}^2+\hat{s}^2\hat{u}^2+\hat{t}^2\hat{u}^2)+$$

$$+28/3M^4\,\hat{s}^2\hat{t}^2\hat{u}^2]+[\hat{s}\leftrightarrow\hat{t}]+[\hat{s}\leftrightarrow\hat{u}]\}$$

$$\frac{d\sigma}{d\hat{t}}(^3P_0) = \xi(\frac{4}{\hat{s}\hat{t}\hat{u}}) \cdot \frac{\hat{s}^{14}[\sum_{n=0}^{6}(\hat{t}\hat{u}/\hat{s}^2)^n C_n(V)]}{[(\hat{s}-M^2)(\hat{t}-M^2)(\hat{u}-M^2)]^4},$$

$$\frac{d\sigma}{d\hat{t}}(^3P_1) = 12\xi \cdot \frac{\hat{s}^{11}[\sum_{n=0}^{5}(\hat{t}\hat{u}/\hat{s}^2)^n C_n(V)]}{[(\hat{s}-M^2)(\hat{t}-M^2)(\hat{u}-M^2)]^4},$$

$$\frac{d\sigma}{d\hat{t}}(^3P_2) = \xi(\frac{4}{\hat{s}\hat{t}\hat{u}}) \cdot \frac{\hat{s}^{14}[\sum_{n=0}^{6}(\hat{t}\hat{u}/\hat{s}^2)^n C_n(V)]}{[(\hat{s}-M^2)(\hat{t}-M^2)(\hat{u}-M^2)]^4},$$

where

$$\xi \equiv (\pi\ \alpha_s^3/16)(M\ \Gamma_e\ r/\alpha^2 e_q^2\ \hat{s}^2).$$

The bound state wave function at the origin is related to the decay width $\Gamma_e \equiv \Gamma(^3S_1 \to e^+\ e^-)$ as $R(0)^2 = \Gamma_e M^2/(2\alpha\ e_q)^2$. M is the mass of the narrow $q\bar{q}$ resonance with the constituents' charge fraction e_q, and $r \equiv [2R'(0)/MR(0)] \simeq 0.074$. The coefficients C_n are linear combination of $V \equiv (M^2/\hat{s})$ and read

$^3\mathbf{P_0}$:

$C_0 = 9V^2(V^8 - 6V^7 + 17V^6 - 30V^5 + 36V^4 - 30V^3 + 17V^2 - 6V + 1),$

$C_1 = 6V(6V^8 - 35V^7 + 98V^6 - 168V^5 + 187V^4 - 135V^3 + 60V^2 - 14V + 1),$

$C_2 = 54V^8 - 324V^7 + 920V^6 - 1506V^5 + 1476V^4 - 850V^3 + 263V^2 - 34V + 1,$

$C_3 = 2(18V^7 - 126V^6 + 377V^5 - 571V^4 + 456V^3 - 187V^2 + 35V - 2),$

$C_4 = 9V^6 - 102V^5 + 344V^4 - 454V^3 + 269V^2 - 68V + 6,$

$C_5 = 2(-9V^4 + 42V^3 - 43V^2 + 16V - 2),$

$C_6 = 9V^2 - 6V + 1.$

$^3\mathbf{P_1}$:

$C_0 = V(V^6 - 8V^5 + 26V^4 - 44V^3 + 41V^2 - 20V + 4),$

$C_1 = 2(V^6 - 9V^5 + 31V^4 - 51V^3 + 41V^2 - 14V + 1),$

$C_2 = 2V^5 - 18V^4 + 59V^3 - 84V^2 + 49V - 8,$

$C_3 = 2(V^4 - 7V^3 + 16V^2 - 17V + 6),$

$C_4 = V^3 - 10V^2 + 13V - 8,$

$C_5 = 2(-2V + 1).$

$^3\mathbf{P_2}$:

$C_0 = 12V^2(-V^8 + 6V^7 - 17V^6 + 30V^5 - 36V^4 + 30V^3 - 17V^2 + 6V - 1),$

$C_1 = 3V(-16V^8 + 96V^7 - 257V^6 + 408V^5 - 434V^4 + 324V^3 - 161V^2 + 44V - 4),$

$C_2 = 2(-36V^8 + 228V^7 - 557V^6 + 747V^5 - 663V^4 + 421V^3 - 173V^2 + 34V - 1),$

$C_3 = -48V^7 + 360V^6 - 782V^5 + 814V^4 - 513V^3 + 244V^2 - 83V + 8,$

$C_4 = 2(-6V^6 + 72V^5 - 149V^4 + 109V^3 - 32V^2 + 11V - 6),$

$C_5 = 24V^4 - 75V^3 + 46V^2 - 7V + 8,$

$C_6 = 2(-6V^2 + 6V - 1).$

The cross sections are $\hat{t} - \hat{u}$ symmetric. The production of the $^3P_0$ and $^3P_2$ states reveals the $\hat{t}$ (and $\hat{u}$) infrared singularities whereas these poles are absent in the production of the $^3P_1$ state.